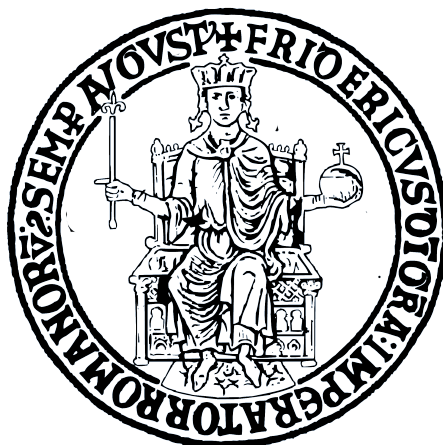


UNIVERSITÀ DEGLI STUDI DI NAPOLI
FEDERICO II



DOCTORAL THESIS

**The Role of Shell effects in Nuclear
Reactions: Multinucleon-Transfer
and Ternary Decay**

Author:

Daniele QUERO

Supervisor:

Prof. Emanuele VARDACI

*A thesis submitted in fulfilment of the requirements
for the degree of Doctor of Philosophy*

December 11, 2018

Declaration of Authorship

I, Daniele QUERO, declare that this thesis titled, “The Role of Shell effects in Nuclear Reactions: Multinucleon-Transfer and Ternary Decay” and the work presented in it are my own. I confirm that:

- This work was done wholly or mainly while in candidature for a research degree at this University.
- Where any part of this thesis has previously been submitted for a degree or any other qualification at this University or any other institution, this has been clearly stated.
- Where I have consulted the published work of others, this is always clearly attributed.
- Where I have quoted from the work of others, the source is always given. With the exception of such quotations, this thesis is entirely my own work.
- I have acknowledged all main sources of help.
- Where the thesis is based on work done by myself jointly with others, I have made clear exactly what was done by others and what I have contributed myself.

Signed:

Date:

...he grabbed my face with both hands, and then for the first time in the entire conversation, he gave me his complete focus and attention, completely present, and calmly said:

“We will never know world peace, until three people can simultaneously look each other straight in the eye. ”

Simultaneous - Puscifer

UNIVERSITÀ DEGLI STUDI DI NAPOLI FEDERICO II

Abstract

Faculty Name

Department of Physics

Doctor of Philosophy

The Role of Shell effects in Nuclear Reactions: Multinucleon-Transfer and Ternary Decay

by Daniele QUERO

The binding energy of *magic* nuclei results in an enhanced stability. This "shell-effects" may be taken into account in the computation of the potential landscape, resulting in deep "valleys" along which the evolution of the system is more probable. This thesis will show two examples: the reaction Xe + Pb, in which the stability of the nuclei (neutron shell-closure) in the entrance channel is exploited to improve the possibility of proton transfer from target to projectile in order to explore the region of the closed shell $N = 126$ and a program of four different reactions, with the aim of searching evidences of the *True Ternary Fission*, trying to take advantage of the possibility of a tripartition (exit channel) leading to one or more magic nuclei.

Acknowledgements

Acknowledgments goes to all those who supported me and believed in me, especially when I was not believing.

All my friends and colleagues, capable of keeping my focused on my work... but also made me unfocus when necessary.

My supervisor and mentor who kept me pushing through this work.

My love, my sweet home who, more than anyone else, got my back and stood by my side. She kept my hand and made me realize that I am more than just the job I do...

Thanks...

Contents

List of Abbreviations	viii
1 Interaction Potential Energy	4
1.1 A Versatile Model	4
1.2 The Role of Shell-Effects	10
1.2.1 Exploration of the <i>Terra Incognita</i>	13
1.2.2 True Ternary Decay	17
2 Xe + Pb LNL Experiment	23
2.1 Scientific Motivation	23
2.2 Experimental Setup	26
2.3 Results and Discussion	29
3 NRO127 JYFL Experiment	40
3.1 Scientific Motivation	40
3.2 Experimental Setup	47
3.3 Results and Discussion	50
3.3.1 Binary Decay	50
3.3.2 Ternary Decay	53
3-body Interpretation of the Kinematics of Two Fragments	53
Inclusion of the Third Particle	58
Comparison with Simulations	59
Other Reactions Results	64

4	Summary and Conclusions	79
4.1	Xe + Pb LNL Experiment	79
4.2	NRO127 JYFL Experiment	80
A	Data Analysis	83
A.1	Preliminary Calculations: Angular Correlation	83
A.2	Detectors Calibration	86
A.2.1	Time Calibration	86
A.2.2	Position Calibration	87
A.2.3	PRISMA Ionization Chamber Calibration	88
A.3	Analysis	88
A.3.1	PRISMA Ionization Chamber	88
A.3.2	TOF-TOF Analysis	88
Laboratory Frame of reference	89
Flight Paths	89
Velocity Calculation	91
A.3.3	TOF-DTSP Analysis	91
Laboratory Frame of reference	91
Flight Paths	93
Velocity Calculation	93
A.3.4	Quantities in Centre of Mass Reference Frame	94
A.3.5	Binary Reaction Analysis	95
V _{par} -V _{per} Test for Binary Decay		95
Angular Correlations		96
Mass and Energy Calculations		97
Energy Loss Corrections		98
A.3.6	Ternary Reaction Analysis	100
Data Filtering for Ternary Decay through <i>Pattern Spectra</i>		100
V _{par} -V _{per} Test for Ternary Decay		101

Test for Evaporated Particles	101
Ternary Decay Mass Reconstruction	102
B Developed Tools and Relative Pseudo Code	105
B.1 Eloss Code	105
B.2 Viola Systematics and prediction of Laboratory correlation an- gles of Fission fragments	107
C Main Experimental Setup Parameters	109
C.1 Xe+Pb Setup	109
C.1.1 PRISMA Arm	109
C.1.2 TOF Arm	110
C.2 NRO127 Setup	111
C.2.1 CORSET	111
C.2.2 Silicon Detectors	111

List of Abbreviations

PES	Potential Energy Surface
DI	Deep Inelastic
QE	Quasi Elastic
QF	Quasi Fission
FF	Fusion Fission
DoF	Degree of Freedom
CN	Compound Nucleus
CF	Complete Fission
TKE	Total Kinetic Energy
PLF	Projectile-Like Fragment
PLF	Target-Like Fragment
TKEL	Total Kinetic Energy Loss
TTF	True Ternary Fission
CM	Centre (of) Mass
TOF	Total Kinetic Energy
LNL	Laboratori Nazionali (di) Legnaro
MCP	Micro- Channel Plate
PPAC	Parallel Plate Avalanche Counter
FMT	Full Momentum Transfer
CORSET	CORrelation SETup
JYFL	Jyväskylän Yliopiston Fysiikan Laitos
ST	START
SP	STOP

Introduction

In the binding energy of atomic nuclei in their ground state there are large fluctuations depending on the proton and neutron number. When such numbers approach the *magic* numbers, namely closed shells, a higher binding energy is observed which gives rise to an enhanced stability. When this "shell-effect" is taken into account in the computation of the potential energy of a nucleus in the macroscopic approximation (namely depending on collective variables), along with another single particle correlation effect called pairing, deep minima appear, along which the time evolution of an excited nuclear system is more probable. The existence of these minima may be exploited experimentally both in entrance and exit channels of a nuclear reaction.

This thesis will show two specific cases: the first is the reaction $^{136}\text{Xe} + ^{208}\text{Pb}$, in which the stability of the reacting nuclei in the entrance channel, due to neutron shell-closures, is exploited to enhance the possibility of proton transfer from target to projectile; the second is a campaign of four different reactions carried out with the aim of searching evidences of the *True Ternary Fission*, namely the simultaneous tripartition (exit channel) of the intermediate composite nucleus leading to three fragments having magic numbers of protons or neutrons or both.

The reaction $^{136}\text{Xe} + ^{208}\text{Pb}$ allows to collect information about the potentialities of the multinucleon transfer (MNT) channel in connection with the production of neutron-rich species. The results show a mass distribution with tails stretching out towards mass asymmetry (production of nuclei heavier than target). The importance of this study stays in the fact that if MNT works in this

mass region, it is expected that it may be used to reach the region of super-heavy nuclei and the region of the predicted *Island of Stability*. The collision $^{136}\text{Xe} + ^{208}\text{Pb}$ has also an interest in astrophysics. It was chosen in order to explore the region of neutron shell-closure $N = 126$ which represents the last known waiting point of the r-process of stellar nucleosynthesis.

The possibility of a ternary decay was suggested in the past by the observation of mass distributions of fragments both in spontaneous (^{252}Cf) and induced $^{235}\text{U}(n, f)$ fission. The occurrence of events in which the measured masses of two fragments is definitely lower than the mass of the parent nucleus was taken as hint of the presence of a third, undetected fragment, thus of the occurrence of a non binary decay. Swiatecki calculations of energy release in a fission event confirms that, under certain circumstances (above a value of the fissility parameter) decay into more than two fragments is even energetically allowed. The aim of the campaign of four experiments was to exploit the advantages provided by a nuclear reaction in order to explore the possibility of ternary decays. Unlike spontaneous fission, a nuclear reaction would allow to reconstruct masses and energies through the kinematics thanks to the possibility of detecting the three fragments. Several shell closures may be found among all the possible tripartitions and may favor the decay into three fragments if the excitation energy is kept low enough allowing the persistence of the shell effects. Hence the choice of a bombarding energy near the Coulomb barrier height.

Thesis Layout

A list of abbreviations (1) may help in the understanding of acronyms.

Chapter organization:

- Chapter 1 introduces the dynamical model within which the potential energy was calculated and marks the role of shell effects;
- Chapter 2 and 3 contain details about the experiments mentioned above and the results of data analysis performed by the author;
- Chapter 4 provides conclusions and remarks.

An appendix section is attached in order to give helpful and specific details about different topics concerning this thesis:

- Appendix A, data analysis procedures;
- Appendix B, algorithms and codes developed during the analysis work;
- Appendix C, parameters of the experimental setups.

A Bibliography section follows.

Chapter 1

Interaction Potential Energy

1.1 A Versatile Model

The Potential Energy Surface (PES) and the role played by shell closures represent the *pivot* for this thesis, being the link between the two experiments, so different from each other, discussed in Chapters 2 and 3.

This model appears very agile and capable of describing simultaneously several competitive processes, such as *Deep Inelastic* (DI) Collisions, *Quasi-Fission* (QF) and *Fusion-Fission* (FF).

It is clear that a dynamical description of a nuclear reaction cannot follow all the single particle degrees of freedom (DoF). The strong suit of the model is, indeed, its dependance on a limited set of *bulk* (collective) degrees of freedom, providing a realistic picture of collective behavior and mass transfer. All the remaining unknown degrees of freedom are treated as a heat bath. Dissipation is the mechanism to transfer energy between the collective degrees of freedom and the heat bath. The dynamical equations that couple these DoF describe the time evolution of the reaction in terms of the chosen variables and their conjugate momenta. The dissipation is treated with a friction term and a stochastic term is used to introduce fluctuations. Friction is due to *viscosity* of a nuclear matter fluid.

The choice of the proper degrees of freedom is crucial to describe the reactions and provide an estimate of cross sections. On one side, the number of degrees of freedom must not be too large in order to have a limited set of coupled differential equations to solve. On the other side, too few variables would not allow the simultaneous description of many channels.

DI processes dominate when the Coulomb repulsion prevails over nuclear attraction and Compound Nucleus (CN) formation is quite improbable. In this case the reaction mechanism depends mainly on nucleus-nucleus interaction potential, friction forces and nucleon transfer rate at contact point. In DI events nuclear compenetration is rather short but, nonetheless, the reaction cross section is found to be sensitive to nuclear viscosity because of large dynamic deformations of the fragments. The kinetic energy of the fragments are almost independent on the beam energies so these events resemble the fission processes even though a CN is not formed [4].

Quasi Fission is a mechanism in strong competition with CN formation and appears when some features of the entrance channel are present. Three main entrance channel properties have been identified: Coulomb factor $Z_{proj} \cdot Z_{targ} \geq 1600$, low mass asymmetry, or values of the nuclear fissility parameter $\chi = Z^2/A$ larger than 0.68 [15]. Also the relative orientation of the two nuclei at the interaction point appears to be very important when one or both fragments are deformed in their ground state. QF is the most important mechanism that prevents the fusion of massive nuclei, useful to produce super-heavy elements [15]. It is a kind of a transitional mechanism, between deep-inelastic collisions and Complete Fusion (CF), in which the composite system separates in two main fragments without forming a CN and a large mass transfer occurs.

In the stochastic model of Zagrebaev and Greiner [2], the chosen degrees of freedom are the following:

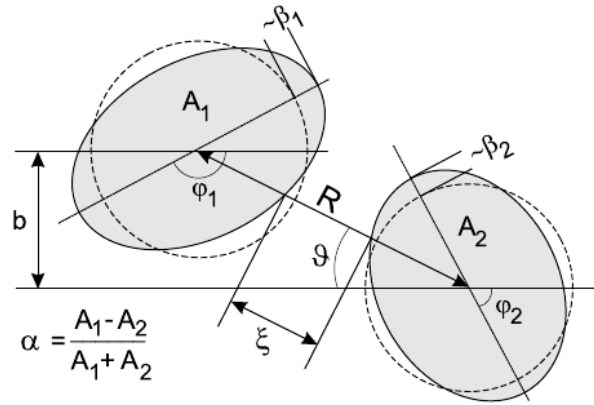


Figure 1.1: Schematic explanation of the degrees of freedom chosen for the calculations [4].

- R , distance between nuclear centers or elongation of mono-nucleus (when a composite system is formed);
- $\beta_{1,2}$, quadrupole deformation of nuclei (representing their shape);
- $\alpha = \frac{A_1 - A_2}{A_1 + A_2}$, mass asymmetry;
- $\phi_{1,2}$, angle of rotation of nuclei in the reaction plane (angle between symmetry axis of deformed nuclei and beam direction);
- ϑ , angle between beam axis and the line connecting nuclear centers (or centroids of composite system).

Fig. 1.1 summarizes, schematically, the degrees of freedom.

Since both neutrons and protons can be exchanged, different fragment species can be obtained by the same amount of generic nucleons transferred. To be able to compute the yield of these different products, it is necessary to consider neutron and proton transfers to be independent, but constrained by the mass asymmetry above.

Thus, two additional variables are introduced:

- $\eta_N = \frac{2N_1 - N_{CN}}{N_{CN}}$, neutron asymmetry in terms of neutron number of one of the fragments;

- $\eta_Z = \frac{2Z_A - Z_{CN}}{Z_{CN}}$, proton asymmetry in terms of atomic number of one of the fragments.

being A_{CN} , N_{CN} , Z_{CN} , respectively, the mass number, the neutron number and the proton number of the composite system.

The dynamical equations mentioned earlier are in the form of Langevin Equation [4], similar to those describing Brownian Motion:

$$\mu\ddot{q} = -\frac{\partial V}{\partial q} - \gamma\dot{q} + \sqrt{\gamma T\Gamma(t)}, \quad (1.1)$$

where:

- q is a generic DoF, with related *inertia parameter* μ ;
- V is the multidimensional potential energy surface plus centrifugal barrier, so $-\frac{\partial V}{\partial q}$ is the *driving force*;
- γ is the viscosity coefficient associated to q , so $-\gamma\dot{q}$ is a friction force;
- $T = \sqrt{\frac{E^*}{a}}$ is the nuclear temperature, a measure of the excitation $E^* = E_{cm} - TKE - V$, TKE is the Total Kinetic Energy of the fragments in exit channel;
- $\Gamma(t)$ is Gaussian distributed and takes into account the stochastic diffusion.

The last term in eq. 1.1 represents a *stochastic force* that, along with the dissipation term, is responsible of energy dissipation during the interaction. In the case of total dissipation of energy, the stochastic force drives the evolution of the system in terms of a path in the potential landscape. Such is the case of near-barrier collisions, where the probability of CN formation is very small for massive nuclei and, due to strong dissipation, the evolution is determined by fluctuations. The low incident (available) energy leads to low excitation and

temperature so the fluctuations are weak and the most probable paths lie on QF valley.

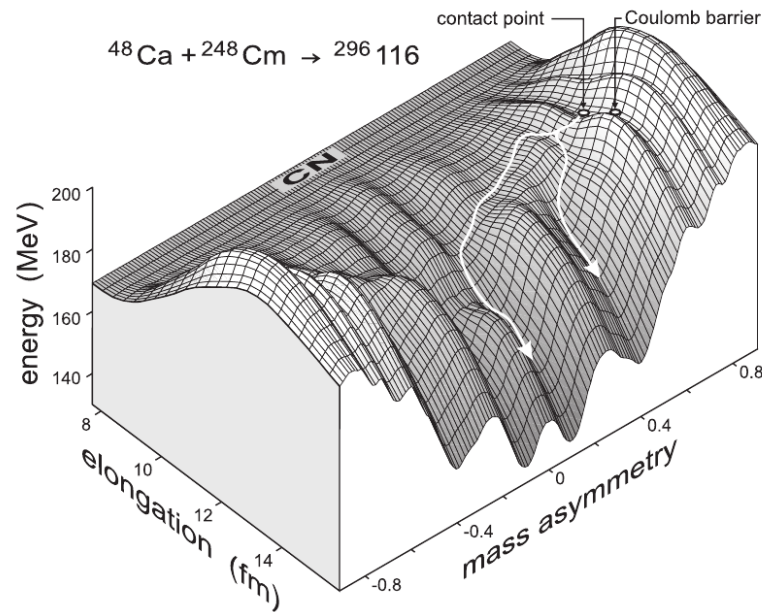


Figure 1.2: 3D view of the potential energy surface for the reaction $^{48}\text{Ca} + ^{248}\text{Cm}$ at deformation $\beta = 0.1$. The two curves with arrows show possible QF paths while the circles represent the *injection point* [4].

In Fig.1.2 and 1.3 some example of PES are shown. They are obtained by projection of the multidimensional potential onto hyperplanes of fixed value of certain degrees of freedom. Arrows represent trajectories (paths) in these landscapes, i.e. the evolution of the system. The dependence on the reciprocal orientation of nuclei is showed in Fig.1.4.

The model takes into account a time dependence in order to describe also reaction times: the potential energy is calculated within the double-folding procedure at the initial (diabatic, energy exchange allowed) reaction stage, and within the extended version of the two-center shell model at the adiabatic (no energy exchange) reaction stage [5]. For the nucleus-nucleus collisions at energies above the Coulomb barrier the potential energy, after contact, gradually transforms from a diabatic potential energy into an adiabatic one, namely: $V(\dots DoF \dots, t) = V_{diab}[1 - f(t)] + V_{adiab}f(t)$ [5]. Here, t is the interaction time

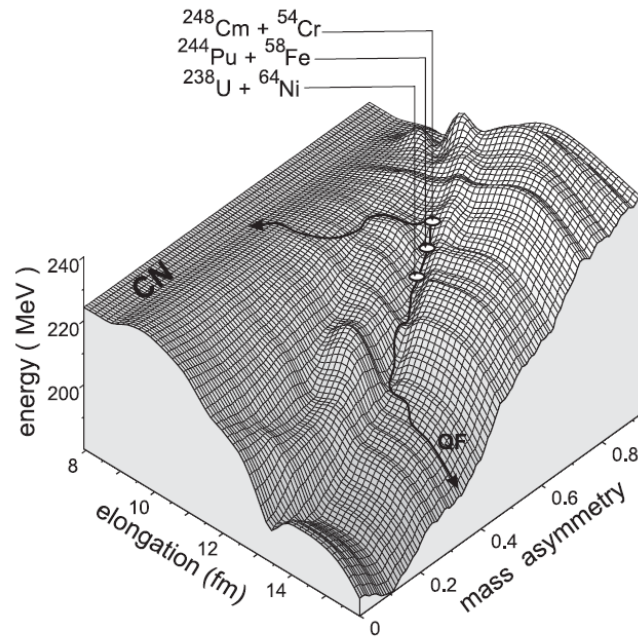


Figure 1.3: PES for a nuclear system of 120 protons and 182 neutrons at fixed deformation $\beta = 0.2$. Injection points for the $^{54}\text{Cr}+^{248}\text{Cm}$, $^{58}\text{Fe}+^{244}\text{Pu}$, and $^{64}\text{Ni}+^{238}\text{U}$ fusion reactions are shown by the circles. The curves with arrows show QF and complete fusion trajectories[3].

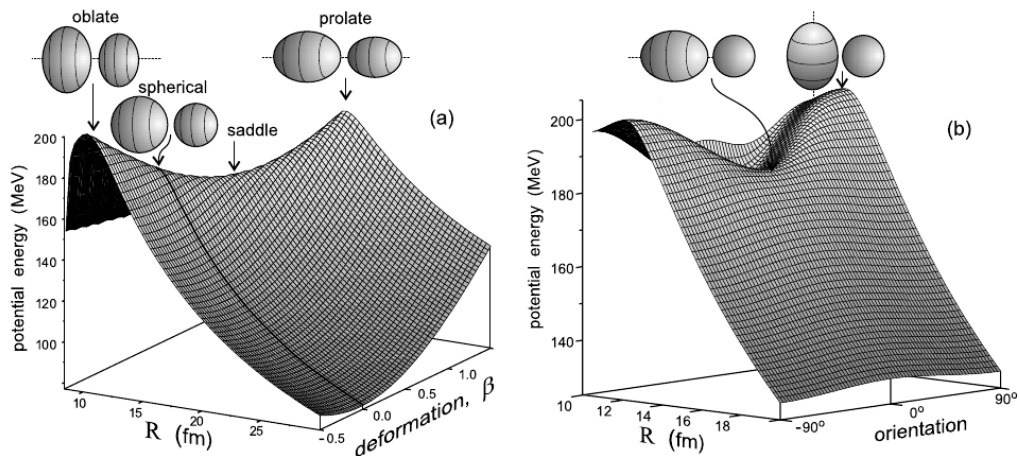


Figure 1.4: (a) Potential energy of $^{48}\text{Ca}+^{208}\text{Pb}$ depending on distance and quadrupole deformations of both nuclei. (b) Potential energy of $^{48}\text{Ca}+^{238}\text{U}$ depending on orientation of the deformed target[4].

and $f(t)$ a smoothing function which operates the transformation from diabatic to adiabatic potential, within a time of the order of 10^{-21} s. Fig. 1.5 shows this transformation for the potential energy as a simple dependence on R variable.

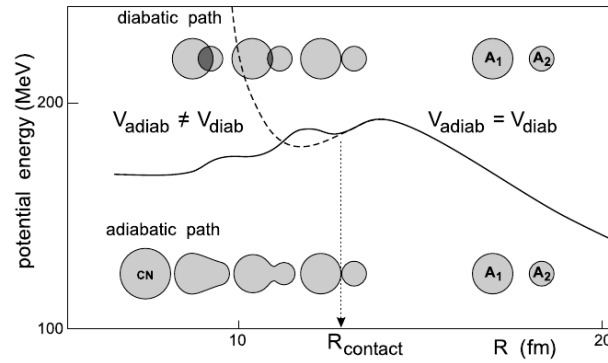


Figure 1.5: Potential energy for the reaction $^{48}\text{Ca}+^{248}\text{Cm}$ in diabatic (dashed curve) and adiabatic (solid curve) conditions [4].

In the next section, it will be shown how the inclusion of the experimental binding energies (*shell-correction*) affect the potential energy and how the latter has been used for predicting observables in the exit channel.

1.2 The Role of Shell-Effects

To take into account the higher binding energy of nuclei, in entrance or exit channel, related to occurrence of *magic numbers* of nucleons (shell-closures), the so called shell-correction are included in the computation of the PES.

The valleys are produced by the proton and neutron shell and pairing correlation corrections, which have a negative value when the nucleon number is magic. These *shell-effects*, result in deep "valleys", in the potential landscape, along which the evolution of the system is more probable. The valley becomes much deeper when two magic numbers occur in the same fragment. The existence of such minima, closely related to mass division leading to magic nuclei, is not just a feature of the PES but can be considered as a powerful tool to tune the properties of the entrance channel.

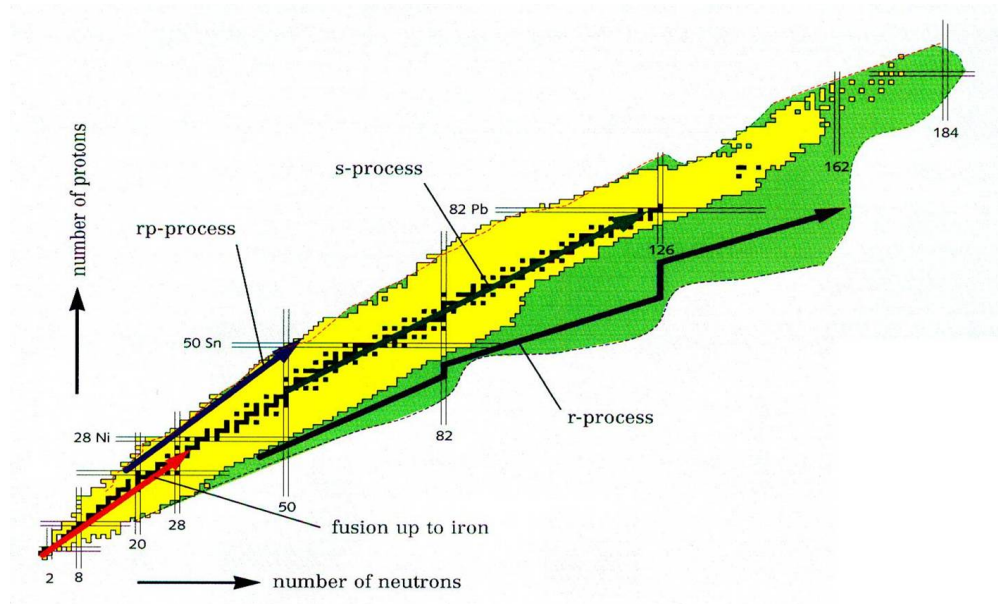


Figure 1.6: The Segré (or nuclide) chart in which each nucleus is placed according to its neutron number N and atomic number Z . The black line represents the stable nuclei, the yellow area includes all known species while the green one is the *Terra Incognita*, embracing all those not yet observed nuclei. The arrows show the path of different stellar nucleosynthesis processes, such as fusion, s -, r -, rp -processes.

The examples provided in these work are related to the exploration of the *Segré Chart* (Fig. 1.6), namely the production of nuclei in the so called *Terra Incognita* and search for possible *true* ternary decay in fission and quasi-fission events, as it will be explained later on.

Among various possibilities, shell-effects may be exploited in the entrance channel as a "stability enhancer" (Par. 2.1) or, in exit channel, being suggested as a possible cause of a direct(simultaneous) tripartition (Par. 1.2.2). One of the strong suits of this kind of study is the (empirically) clear link between the reaction channel, shell-effects and some observables such as the fragment mass and Total Kinetic Energy (TKE).

As an example of the importance of these observables, Fig. 1.7 shows how the valleys in the landscape are related to several mass divisions that can be associated to specific loci of the Mass-TKE distribution and reaction mechanisms. The PES shown in figure is related to the reaction $^{48}\text{Ca}+^{248}\text{Cm}$, that led to the

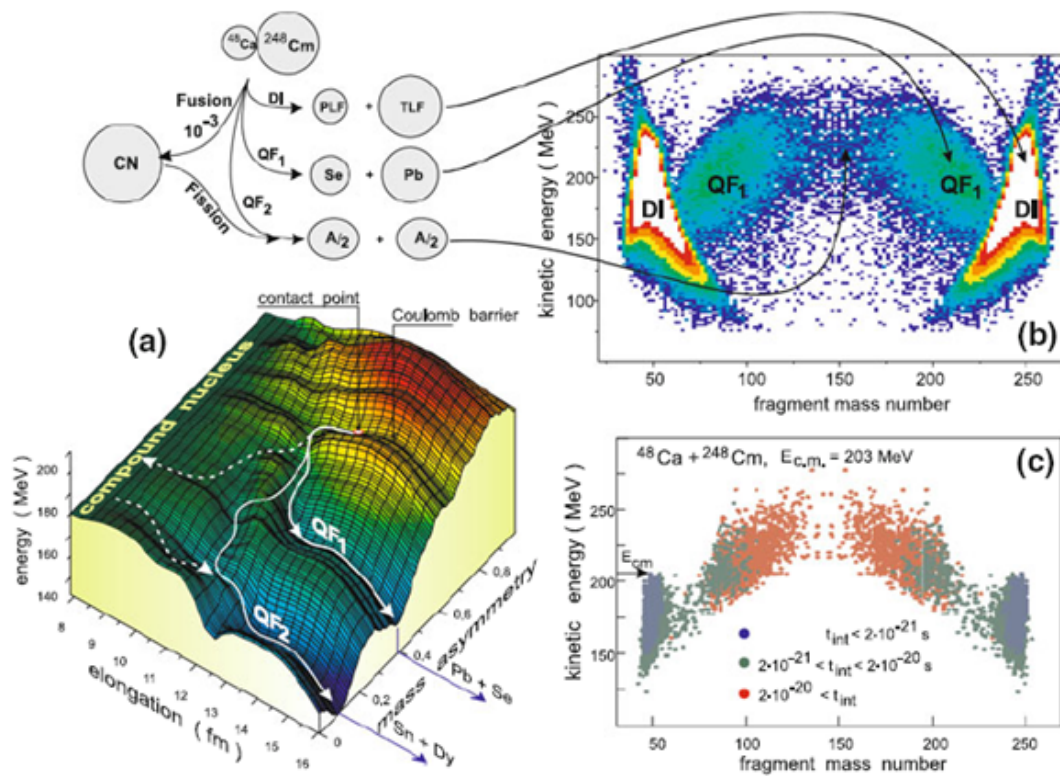


Figure 1.7: $^{48}\text{Ca} + ^{248}\text{Cm}$ is the reaction that produced the Livermorium element [22]. It is possible to see the link between the reaction channels, shell-effects and the observables mass and TKE. In panel a) Adiabatic driving potential for the nuclear system formed in the collision. The solid lines with arrows show schematically (without fluctuations) the quasi-fission trajectories going to the lead and tin valleys. The dashed curves correspond to complete fusion (CN formation) and fission processes. Experimental b) and calculated c) mass-energy distribution of reaction fragments in collision at 203 MeV center-of-mass energy. Different colors in c) indicate the interaction time of different events (longer for larger mass rearrangement). However, it is clear that QF and FF cannot be disentangled by means of just mass and TKE observables.

observation of element 118. It is also shown that the trajectories that could lead to a CN formation are located at higher values of the potential and several bifurcations are possible. This means that the injection point (entrance channel properties such as mass asymmetry, see also Fig. 1.16) plays an important role and, also because of fluctuations, the trajectories may overcome the barriers to reach the CN valley (if existent) or may even tunnel through. The potential energy surface is therefore the playground where to explore the possible reaction paths.

It is interesting to note that, looking at the M-TKE distribution, the case of QF leads to an almost symmetric mass division that would be indistinguishable from the symmetric mass division that can arise if FF would appear. The only possibility to disentangle the two mechanisms is to use other observables, such as gamma emission [30].

1.2.1 Exploration of the *Terra Incognita*

The Segré chart of nuclides (Fig. 1.6) can be explored by means of several channels: due to the curvature of the stability line, with fusion reactions it is possible to reach the proton-rich side of the map, medium-heavy nuclei fission can produce neutron-rich species of medium mass while there is no certainty about production channels for heavy and super-heavy neutron-rich nuclei.

The production of the unknown nuclei in this so-called *Terra Incognita* (the green area in the chart) is the mean to study topics of great interest in nuclear physics and astrophysics, such as:

- the search for *Island of Stability*, a return of stability predicted around $N=184$ and $Z=114-126$ (next shell-closures);
- the stellar nucleosynthesis of heavy elements, "*How were the heavy elements from iron to uranium made?*" is considered the third among the "The 11

Greatest Unanswered Questions of Physics” (Discover Magazine [1]). A possible answer would be the *r-process*, whose path lies deeply in the *Terra Incognita* (Fig. 1.6);

- the study of the quenching of shell closure in nuclei with large neutron excess.

In order to fill the “blank region” of the nuclear map, largely extended in the neutron-rich side, multinucleon transfer process in low energy collisions of heavy nuclei has been proposed [2]. In the DI collisions of heavy ions the energy of relative motion is quickly transformed into the internal excitation of the projectile-like (PLF) and target-like (TLF) fragments which afterward de-excite by evaporation of light particles (mostly neutrons). At a first glance, this does not seem of any help for the production of neutron-rich nuclei. However, if the Total Kinetic Energy Lost (TKEL) is kept low, the primary reaction fragments might not be very much excited (eq. 1.3) and will descend to their ground states after evaporation of a few neutrons, thus remaining far from the stability line.

$$TKEL = E_{cm} - TKE \quad (1.2)$$

$$E_{frag}^* = TKEL + Q_{gg} \quad (1.3)$$

It has been shown experimentally that even at low energies (close to the Coulomb barrier) the cross sections for transfer of several protons and neutrons are still rather high [7], and this kind of reactions could be considered as an alternative way for the production of exotic nuclei.

The satisfactory agreement (Fig. 1.8 and Fig. 1.9) between experimental data and calculation, within the model [4] proposed by V. Zagrebaev and W. Greiner, gave confidence in obtaining reliable estimations of the cross section

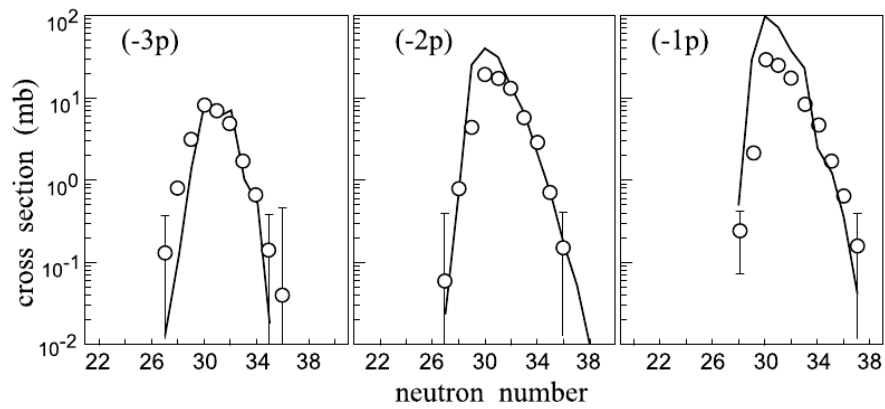


Figure 1.8: Angular and energy integrated cross sections for proton and neutron transfer in the reaction $^{58}\text{Ni}+^{208}\text{Pb}$ @ $E_{\text{lab}} = 328.4\text{MeV}$. Experimental data (open circles) are from [7].

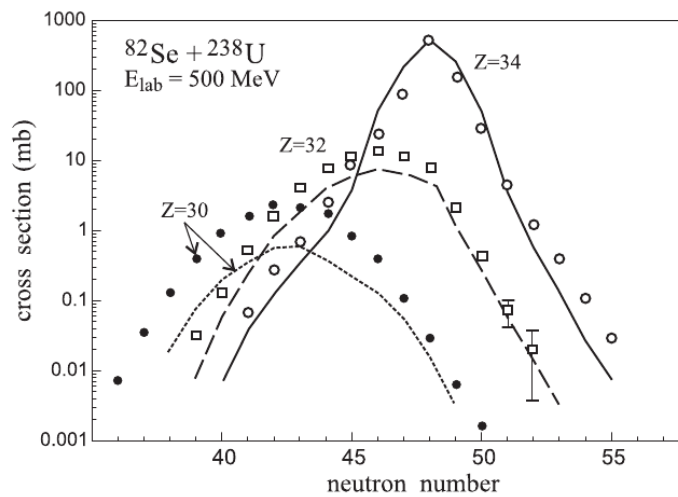


Figure 1.9: Mass distribution of the projectile-like fragments with $Z = 30, 32$ and 34 formed in the collision $^{82}\text{Se}+^{238}\text{U}$ @ $E_{\text{lab}} = 500\text{MeV}$. The experimental data are from [8].

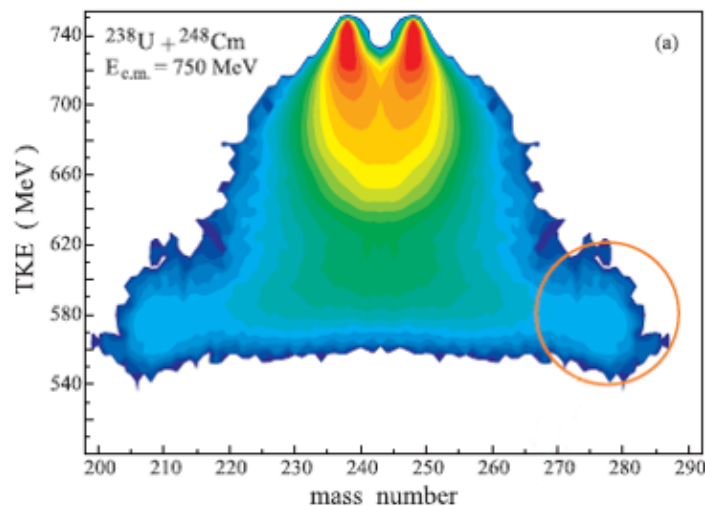


Figure 1.10: M-TKE distribution of the reaction $^{238}\text{U} + ^{248}\text{Cm}$, calculated within Zagrebaev and Greiner model [6]. The majority of events are Quasi-Elastic type, but there is the possibility to reach super heavy-fragments in transfers that increase the mass asymmetry. The circle shows that super-heavy species, close to the center of the Island of Stability, can be reached in these processes.

of near-barrier multinucleon transfer reactions producing heavy neutron-rich species. It is clear that an appropriate choice of colliding partners (thus the tuning of the injection point) is quite important for the production of nuclei in a specific region. Moreover, shell effects play a very important role in the mass rearrangement both in Fusion-Fission and Deep Inelastic processes, and may possibly help in the production of neutron-rich species.

An example of calculation conducted within this model [6] is shown in Fig. 1.10, a M-TKE distribution of fragments from the reaction $^{238}\text{U} + ^{248}\text{Cm}$. The most populated area lies around masses of projectile and target coming from Quasi-Elastic or Deep Inelastic reactions, but it is noticeable the possibility of massive transfer leading to strongly asymmetric final configurations, thus to super-heavy nuclei: the masses inside the circle in figure are in a region close to the center of Island of Stability.

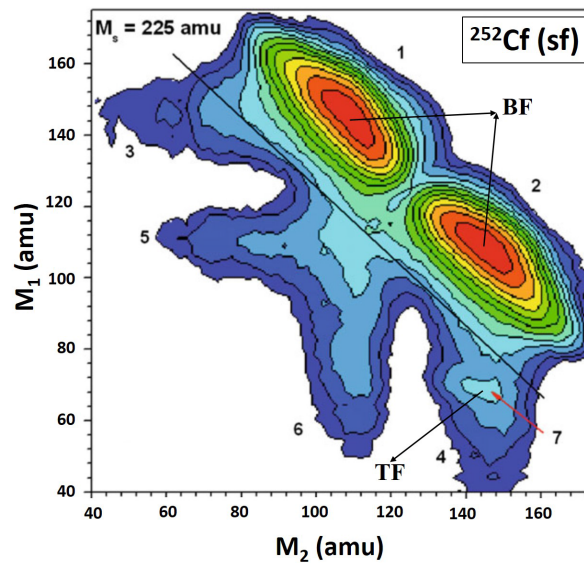


Figure 1.11: Mass-mass distribution of the collinear fragments, detected in coincidence, in the spontaneous decay of ^{252}Cf [11]. The black solid line refers to masses summing up to 225 u, some mass is missing: a hint that the fragments may not come from binary decay. The two most populated spots represent fragments summing up to 252 u mass, coming from binary fission.

1.2.2 True Ternary Decay

The expression "Ternary Fission", referring to the break up of the nucleus into three fragments, was often used in cases where the third fragment is much lighter (up to 30 mass units) than the other two [9, 10]. The break up into three fragments having similar masses is defined as a "True Ternary Fission" (TTF) and has been recently reported in the spontaneous fission of ^{252}Cf [11]. TTF decay occurs dominantly in a collinear geometry and when the three fragments have strong connection with shell closures (it was previously called Collinear Cluster Tripartition). Fig. 1.11 shows the mass-mass distribution of the collinear fragments, detected in coincidence, in the spontaneous decay of ^{252}Cf . There are events in which the masses of the two fragments does not sum up to the mass of the parent nucleus (252 u). For instance, the black solid line shows events with masses summing up to 225 u. Since there is a substantial missing mass, this can be taken as a hint that the fragments may not come from binary decay.

Fig. 1.12 shows, on the other hand, similar features also in induced fission of ^{236}U (neutron bombarding of ^{235}U).

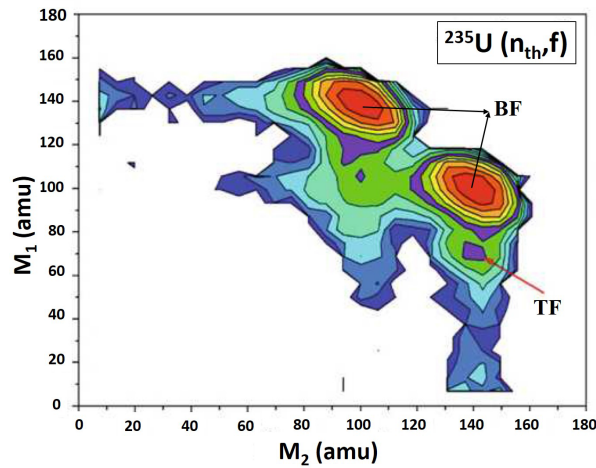


Figure 1.12: Mass-mass distribution of the collinear fragments, detected in coincidence, in the reaction $n + ^{235}\text{U}$ [11]. The two most populated spots represent fragments summing up to 252 u mass, coming from binary fission. The distribution shows also the possibility of events in which the sum of masses of the two fragments is less than 235 u.

It is known that a heavy nucleus generally fissions into two fragments rather than into three or more, even though division into three or more fragments would release more energy. Fig. 1.13 shows the results of calculations made by Swiatecki [12], within the Liquid Drop Model: the energy release for fission into n equal fragments depends on the fissility parameter χ . Clearly, a tripartition becomes exothermic for $\chi \geq 0.426$, and from $\chi = 0.611$ onwards its energy gain is greater than in binary fission. With increasing charge (fissility parameter), fission into even more than three fragments becomes energetically favored and it is clear that the height of the fission barrier rather than the energy release determines the yield of the process.

Diehl and Greiner, on the basis of a two and three center shell model, built a potential energy surfaces [13] depending on different shape parameters. With a more complex parametrization of the shapes they were able to study the paths in the PES bringing to prolate (three fragments aligned) or oblate (equilateral

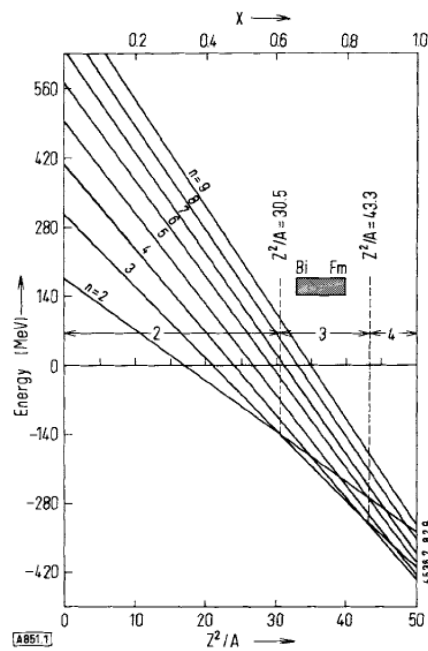


Figure 1.13: Decay energy of an ideal, electrically charged liquid drop vs. the fissility parameter. The parameter n gives the number of equally sized fragments obtained in the decay process [12].

triangle) configurations of the three nascent fragments and to provide an explanation of the lower ternary decay probability.

On the ternary fission path, the system comes across two barriers and the second one is more than three times higher than the liquid drop barriers for the binary fission path. An increase in the charge brings to a gradual reduction of this second barrier, which eventually disappears. At this point the choice of the fission mode falls on dynamical effects. With increasing nucleus mass, calculated barriers for ternary fission are only slightly higher than those for binary fission [13], while increasing temperature has the effect of reducing the surface tension of the liquid drop, resulting in decreasing barriers (Fig. 1.14).

Barrier height calculations, for binary and ternary fission, were also performed by Royer and Mignen [14], within the rotational liquid drop model at finite temperature and including the nuclear proximity energy as a function of the temperature of the nucleus. For larger masses, both barriers reach gradually

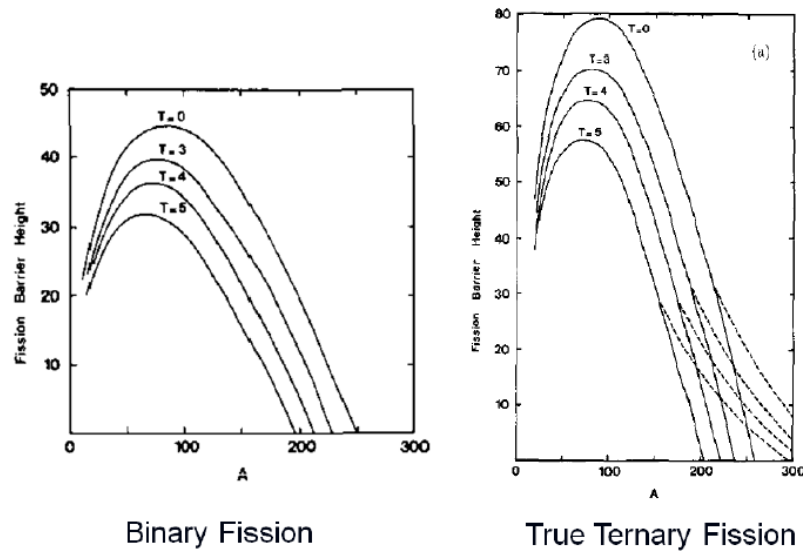


Figure 1.14: Barrier heights (in MeV) for symmetric binary and ternary fission of nuclei along the β stability valley as a function of temperature and mass number.

similar values as in [13].

Three-body decay may also be explored in quasi-fission, taking advantage of the fact that this process is strongly influenced by the shell closures of the emerging fragments [15]. The idea of ternary fission driven by shell effects was also proposed by Zagrebaev and Greiner [16]. Their potential surfaces, can describe an enormous set of experimental data on the Mass-TKE distributions of binary reactions between heavy nuclei leading to quasi-fission, and can possibly predict decay paths leading to three, similarly massive, fragment decay. These decays are due to shell-effects.

A reported case is the one of ^{248}Cm [16], in which a tripartition channel appears along with binary decays. Very recent calculations based on a macroscopic approach [17] show how a ternary fission path emerges from shell correction on a macroscopic liquid drop potential.

Theoretical studies were also conducted about ^{252}Cf , using a 3 cluster model, searching for all possible geometrical configuration leading to a tripartition of the type $A_1 > A_2 > A_3$. As visible in Fig. 1.15 strong shell effects produce

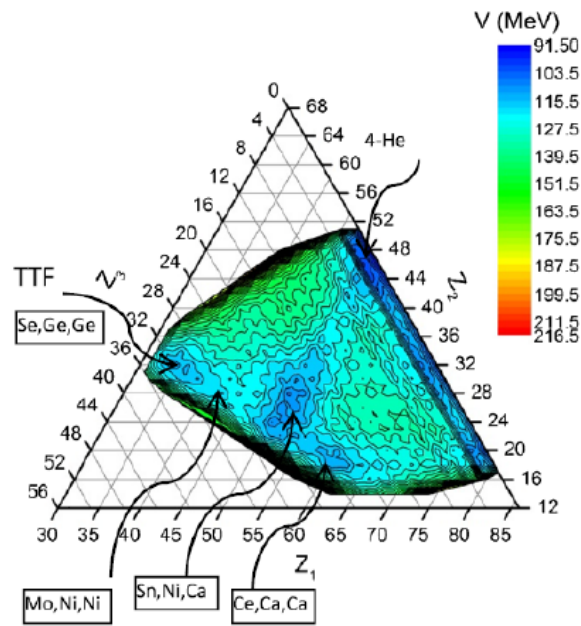


Figure 1.15: Potential energy as a function of charge number of ternary fission of ^{252}Cf [18, 19].

minima, in the potential energy, when fragments are magic nuclei, i.e. have shell-closures [18, 19]. Again, collinear configurations appear to increase the probability of emission of a *heavy* third fragment (such as ^{48}Ca , ^{50}Ca , ^{54}Ti , and ^{60}Cr) while an equatorial configuration may be preferred for light nuclei.

Three-body decay are also predicted for giant nuclear systems where no fusion is possible at all. This is the case of the collision $^{238}\text{U}+^{238}\text{U}$ [20] where the potential energy may have minima corresponding to three fragments in the final state. These minima, and relative final configurations, are shown in the potential landscape in Fig. 1.16.

Lastly, ternary fission is also an extremely important ingredient of the r-process nucleo-synthesis, being competitive with β -delayed fission [21] for heavy nuclei having $Z^2/A > 30.5$.

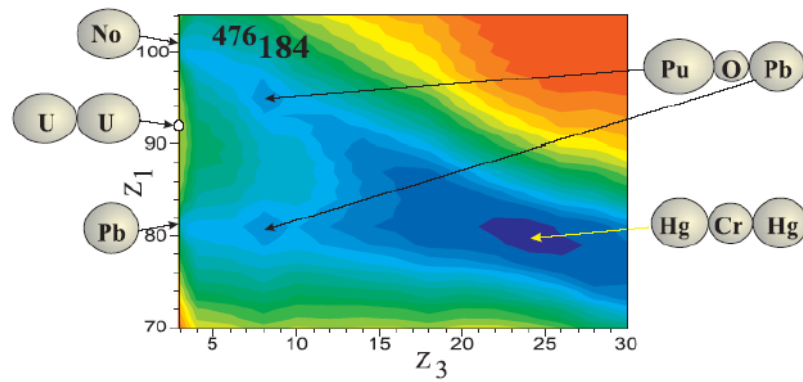


Figure 1.16: Potential energy surface for the collinear tripartition of ^{242}Cf vs. the charge of the three fragments (courtesy of M. Balasubramaniam).

Chapter 2

Xe + Pb LNL Experiment

2.1 Scientific Motivation

The exploration of the unknown regions of the Segré map (Fig. 1.6) and search for the predicted, so-called *Island of Stability* centered at $N = 184$, $Z = 114$ - 120 , represent some of the most interesting topics in nuclear physics. Quantities such as half-lives and masses (binding energies) are extremely important also for nuclear astrophysics investigations and for the understanding of the r-process: the last "waiting point" of the rapid neutron capture process, corresponding to the closed neutron shell $N = 126$, lies indeed deeply in the Terra Incognita. Aside from the astrophysical interest, the study of the structural properties of exotic neutron-rich nuclei would also contribute to the discussion of the quenching of shell effects in nuclei with large neutron excess.

Concerning their production, there are three known possibilities: the multi-nucleon transfer reactions [2], fusion reactions with neutron rich radioactive nuclei and rapid neutron capture process. On one hand, the last two channels look unfeasible because of low intensity of currently available radioactive beams and low neutron fluxes, for example in working nuclear reactors. On the other hand, the low energy multi-nucleon transfer reactions, along with the quasi-fission processes [22] offer a more feasible ground for the production of neutron-rich nuclei, even by means of stable beams, with cross sections of the

order of few mb or μb [23]. Emblematic is the collision $^{136}\text{Xe} + ^{208}\text{Pb}$ at energies close to the Coulomb barrier, already explored in a preliminary experiment in 2012 in Dubna [23] with beam energies of 700, 870 and 1020 MeV and Target-Like Fragment identification via catcher-foil activity analysis. The reaction was then re-proposed in 2014 in Legnaro, exploiting the PRISMA setup.

Both Xe and Pb nuclei have a closed neutron shell, respectively $N = 82$ and $N = 126$; because of this, proton transfer from Pb to Xe might be favorable, allowing the exploration of the closed shell $N = 126$ (Fig. 2.1).

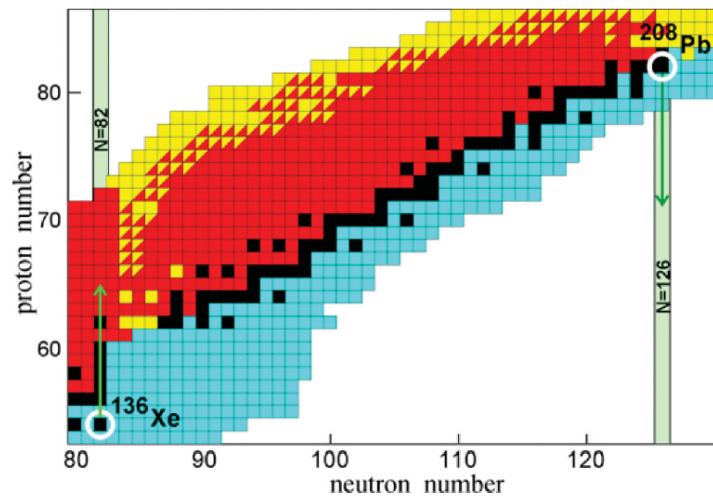


Figure 2.1: Schematic representation of (only proton transfer along neutron closed shell $N = 126$ in the low-energy collisions $^{136}\text{Xe} + ^{208}\text{Pb}$. Black squares indicate stable nuclei, red color stands for β^+ , blue for β^- and yellow for α instability.

The bombarding energy in the center of mass (CM) reference frame was then set to 526 MeV, slightly above the coulomb barrier (422 MeV in the Bass parametrization [24] and would result in an advantage: equations 1.3 show how a low bombarding energy leads to a low TKEL thus to a low excitation energy, increasing the probability of fragment survival against neutron evaporation or fission. As mentioned above, the stabilizing role of neutron shell closure in ^{136}Xe and ^{208}Pb might favor proton transfer from target to projectile and lead to the formation of well bound fragments in the exit channel, with reaction

Q-values distributed around zero (Fig. 2.2). As an example, the Q-values for two possible reactions are provide below:

- $Q(^{136}\text{Xe} + ^{208}\text{Pb} \rightarrow ^{140}\text{Ce} + ^{204}\text{Pt}) = 1.5 \text{ MeV};$
- $Q(^{136}\text{Xe} + ^{208}\text{Pb} \rightarrow ^{142}\text{Nd} + ^{202}\text{Os}) = -8.3 \text{ MeV}.$

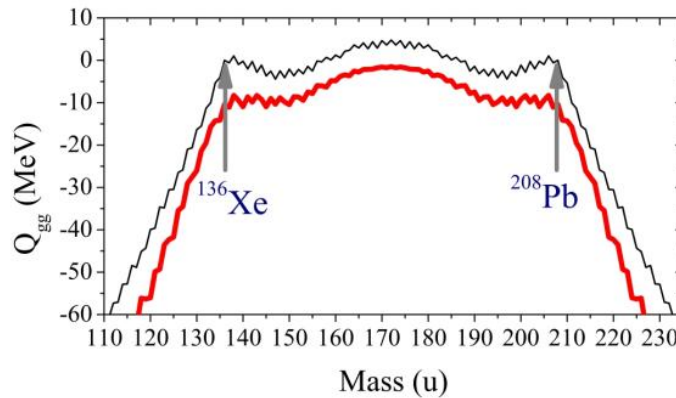


Figure 2.2: Q-value distribution in the ground state for all possible mass transfers in the reaction $^{136}\text{Xe} + ^{208}\text{Pb}$ ($Q_{gg} = M_P + M_T - M_{TLF} - M_{PLF}$). The red line represents the mean values while the black line the maximum ones [23]. For largely asymmetric transfers the Q-values are negative while the distribution is around zero for more symmetric configurations.

The results of the previous experiment [23] show possible transfers up to about 20 nucleons. Furthermore, there is a good agreement with cross section calculations [2] in the region of interest ($A \sim 200$ and $Q_{gg} \sim 0$) and the yield is even underestimated of up to a factor 2 in the region of super-asymmetric fragments, meaning that the model has good prediction capabilities and, most importantly, this production channel has a great potential in terms of exploration of the super-heavy region in the Segré chart.

Mass-TKE distributions of the products can be measured by using a kinematic method, namely by measuring the Time Of Flight (TOF) of two fragments in coincidence along with the momentum and mass number conservation laws. In this way the mass and energy distribution of primary fragments is obtained. The results of the experiment held at Laboratori Nazionali di Legnaro with the

PRISMA setup represents a step forward, for the possibility of atomic number identification of one of the fragments. The atomic number of the partner fragment can be derived indirectly using the fact that that emission of light charged particles (such as proton or alpha) has a nearly zero probability for this type of reactions. Each step of the analysis will be discussed separately in Appendix [A](#) while a setup overview, results and considerations will be shown in the further sections.

2.2 Experimental Setup

The experimental setup consists of two setups coupled together: the magnetic spectrometer PRISMA and a second arm (which will be referred to as "TOF" arm) also including a Bragg chamber. The ensemble, also called "modernized PRISMA", is shown in [Fig. 2.3](#) as a schematic drawing of two arms placed at 45° and 52° , respectively. [Fig. 2.4](#) is a 3D view of the apparatus, with examples of fragment trajectories. Position sensitive detectors and TOF spectrometers are exploited in order to evaluate velocity vectors and produce mass-energy distributions, as done by using the spectrometer CORSET [\[23\]](#). As it will be shown later, the fragments primary masses and kinetic energies, after proper corrections, are obtained by using two body kinematics, making use of velocity vectors of the secondary fragments (namely, after neutron evaporation). In PRISMA, the atomic number can be evaluated with the use of E- Δ E telescopes in one arm, and by Bragg peak analysis in the other arm. As a single arm, PRISMA is capable of measuring the fragment mass by means of the trajectory reconstruction in the known magnetic field.

PRISMA is a magnetic, large acceptance, spectrometer for heavy ions, installed at Legnaro National Laboratory of INFN [\[25\]](#). The principal features of the spectrometer are its large solid angle (80 msr) and momentum acceptance

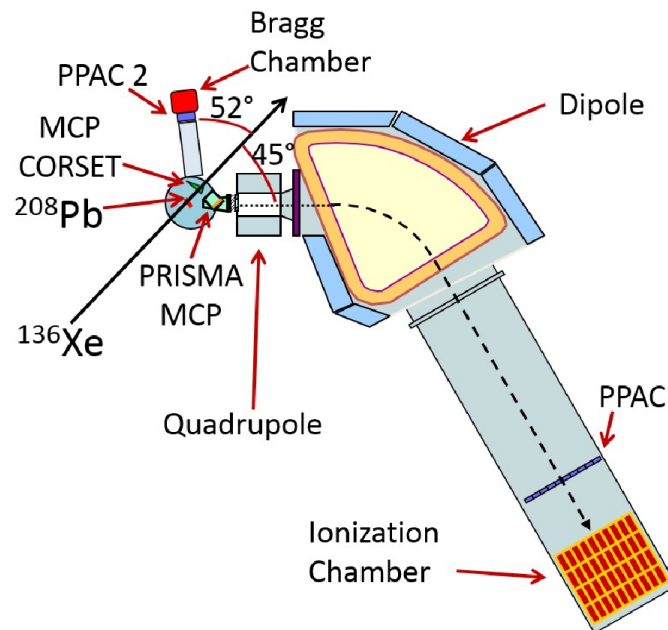


Figure 2.3: View of the modernized PRISMA setup. PRISMA arm is placed at 45° with respect to beam direction while the TOF arm is placed at 52° . The mass distributions of primary fragments are obtained by using the entrance detectors: PRISMA MCP (position sensitive, as Stop), CORSET MCP (Start) and a circular PPAC (position sensitive, Stop).

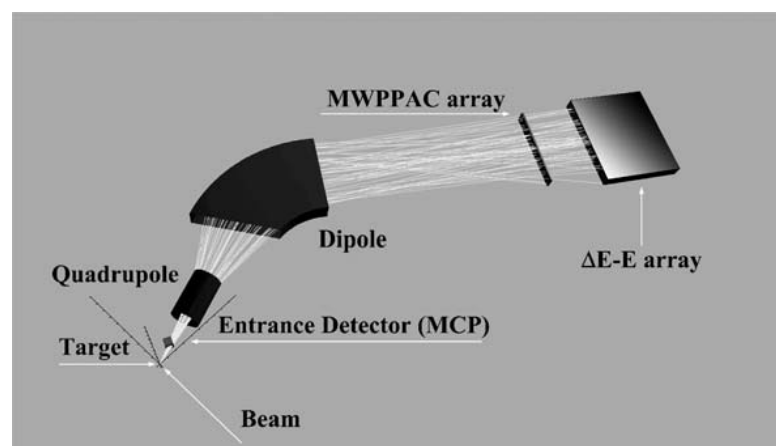


Figure 2.4: 3D sketch of PRISMA with some fragment trajectories. The transport is operated by magnetic optical elements .

($\pm 10\%$). The spectrometer is capable of rotation around the target in the angular range from 30° to 130° . With this very large acceptance, it is unfeasible to use complex magnetic elements to correct the optical aberrations and the best solution was to use of a simplified magnetic element configuration.

The included detectors are:

- a rectangular shaped, pass through, Micro-Channel Plate (MCP) entrance detector (area $76 \times 100 \text{ mm}^2$) capable of rotation, placed 25 cm from the target, providing X, Y (with 1 mm resolution) and a time signals [26];
- a set of focal plane detectors (area $100 \times 13 \text{ cm}^2$) [27], consisting of:
 - an array of ten multi-wire Parallel Plate Avalanche Counter (PPAC) detectors (area $10 \times 13 \text{ cm}^2$), placed at 300 cm from the dipole exit, providing X, Y position (1 mm and 2 mm resolution respectively) on the focal plane, and a time signal;
 - an array 10×4 of split-anode Ionization Chambers (IC) ($100 \times 13 \times 25 \text{ cm}^3$) working as E- ΔE telescope.

The TOF arm consists in the following cascade of detectors:

- A pass through MCP-based START detector ($4 \times 2 \text{ cm}^2$), taken from a CORSET setup (thus referred as "CORSET MCP"), not sensitive to the position hit by the fragment;
- A pass through circular PPAC ($10 \times 10 \text{ cm}^2$) with 1 mm resolution
- A Bragg chamber providing signals corresponding to the energy of the fragment (area below Bragg curve) and to the Bragg Peak (area below the peak).

The Bragg Chamber was not used during the experiment.

Tables C.1 and C.2 show the main specification parameters of the setup.

2.3 Results and Discussion

TOF data along with position information are used to measure the velocity vector of each fragment. Therefore event-by-event it is possible to apply the momentum conservation law and mass number conservation law to obtain the mass and energy distribution of primary fragments. The term “primary” stands for fragments before emission of neutrons, which in principle occurs before the detection of “secondary” fragments. Since the emission of few neutrons does not affect sensibly (due to the ratio between neutron and fragment masses) the velocity vector (direction and modulus) of the emitting (secondary) fragment the reconstruction method allows to obtain the primary masses with the hypothesis that the velocity of the primary fragments is conserved after neutron evaporation.

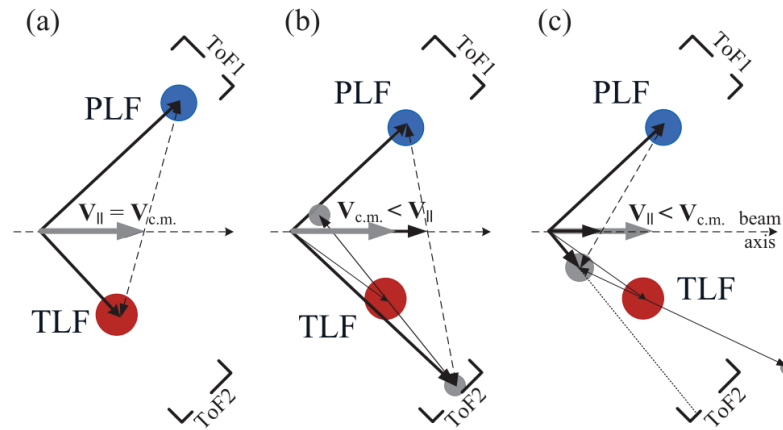


Figure 2.5: Kinematic Diagram, useful to tell if an event is FMT binary or a sequential fission. (a) $V_{||} = V_{cm}$, a FMT binary event; (b) $V_{||} > V_{cm}$, (sequential) fission of a fragment and the secondary fragment emitted forward is detected; (c) $V_{||} < V_{cm}$, similar to the previous but the secondary fragment emitted backward is detected [23].

Along with the two masses and TKE, many other useful quantities can be evaluated from the raw data. Some examples are the folding angle (both in center of mass and laboratory reference frame) and the projections of velocity vectors onto the reaction plane (V_{par}) and orthogonally to it (V_{per}), see also App. A. These two projections are an extremely useful probe in the search for binary

Full Momentum Transfer (FMT) events, for which V_{par} is distributed around the center of mass velocity and V_{per} around zero.

Fig. 2.5 shows a kinematic diagram explaining how the value of V_{par} can be used to tell three different cases:

- (a) $V_{par} = V_{cm}$, a FMT binary event for which the kinematic reconstruct is well interpreted;
- (b) $V_{par} > V_{cm}$, the case in which (sequential) fission of a (usually target-like) fragment occurs and the secondary fragment emitted forward is detected, leading to a misinterpretation of the velocities;
- (c) $V_{par} < V_{cm}$, similar to the previous but the secondary fragment emitted backward is detected.

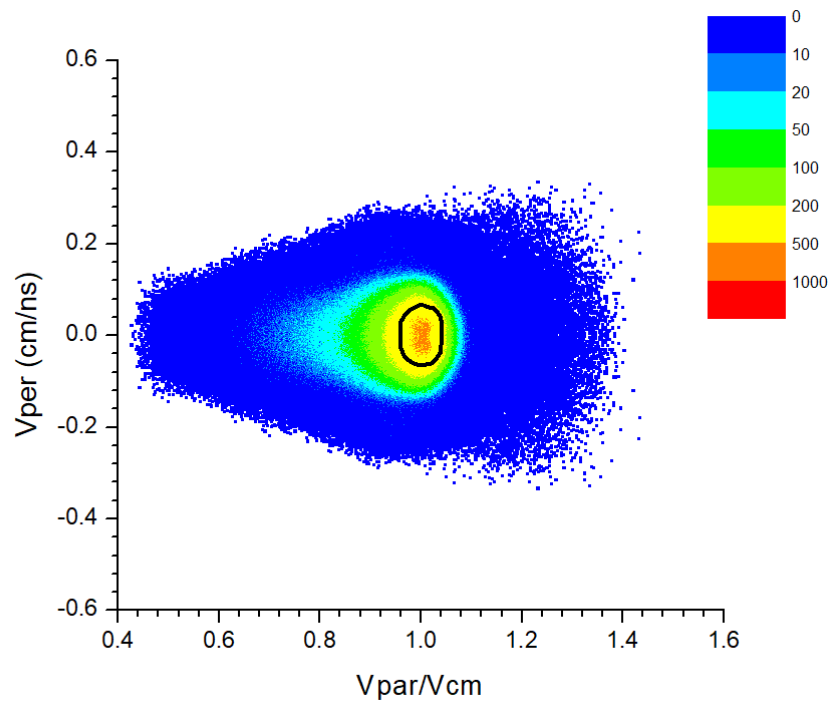


Figure 2.6: $V_{par} - V_{per}$ matrix. The black circle represents the gate used to select the binary, full momentum transfer events.

Fig. 2.6 is the experimental $V_{par} - V_{per}$ matrix. The most populated spot lies in region with V_{per} distributed around zero and V_{par} around the center of

mass velocity (1.39 cm/ns in this reaction) and a gate around this spot is used to select the FMT events.

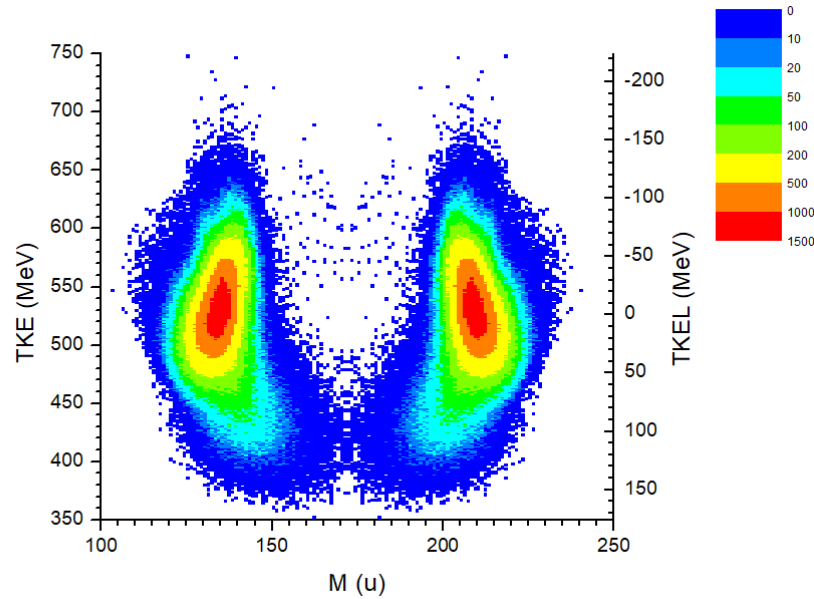


Figure 2.7: M-TKE distribution of primary fragments in the reaction $^{136}\text{Xe} + ^{208}\text{Pb}$ @ $E_{\text{cm}} = 526$ MeV. The right Y axis shows the TKEL (eq. 1.3). A significant part of the event has large energy dissipation.

The M-TKE distribution in Fig. 2.7 is obtained after the application of the mentioned gate (see A for detailed analysis steps). A significant part of the event has large energy dissipation. It is interesting to notice that for a fixed value of TKEL several masses can be produced, suggesting that the mass rearrangement may depend also on other observables.

The quasi-elastic peaks are centered around the masses of projectile and target (136 and 208 u, respectively) and around the center-of-mass energy of 526 MeV, as remarked by the markers in Fig. 2.8 and 2.9. Primary mass distribution was already published in [28].

Among the aims of the experiment there is the observation of species along the closed shell $N=126$, such as ^{202}Os (and companion ^{142}Nd), thus a particular attention will be put on this mass value.

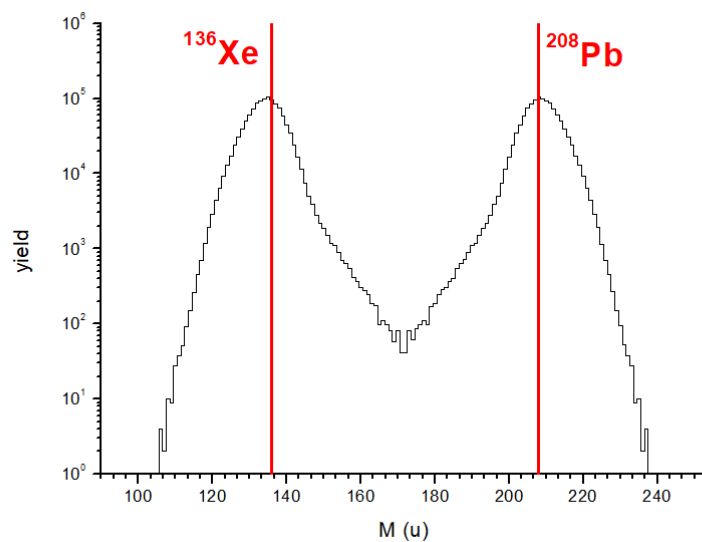


Figure 2.8: Mass distribution of primary fragments. The red markers highlight the masses of projectile and target. Data already published in [28].

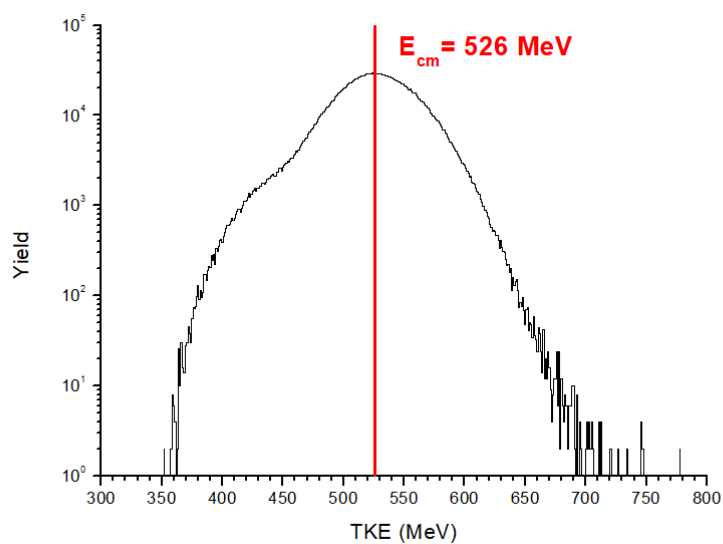


Figure 2.9: TKE distribution of primary fragments. The red marker highlights the bombarding energy in the Center of Mass reference frame (526 MeV).

Eq. 1.3 gives the definition of TKEL, which represent the amount of energy dissipated during the reaction. Quasi Elastic (QE) collision would have a TKEL ~ 25 MeV, DI collision usually have values smaller than 50 MeV, while multi-nucleon transfers may be interested by larger values. Fig. 2.10 represents the TKEL distribution. A gaussian fit in the Elastic and QE zone is used to mark the value (60 MeV) beyond which there damped collisions are located.

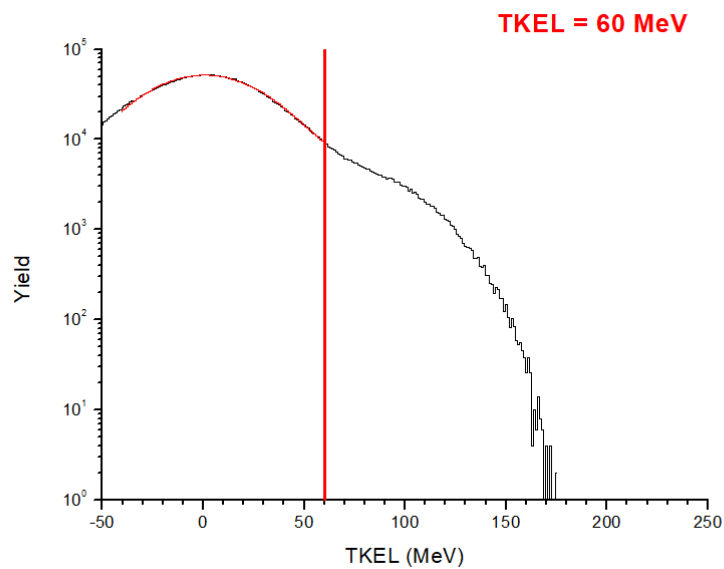


Figure 2.10: TKEL distribution (1.3). A gaussian fit in the Elastic and QE zone is used to mark the value (60 MeV) beyond which damped collisions appear.

Fig. 2.11 shows the effects of window selections in the TKEL distribution (Fig. 2.10) on primary TLF mass distribution in particular the ranges 80-90 MeV (black line), 90-100 MeV (red line), 100-110 MeV (blue line) and 110-120 MeV (green line). The marks show the position of the peaks: 204, 202, 201 and 200 u respectively. The aimed mass ($A = 202$) is produced in events with a dissipation in the range 90-110 MeV.

It is important to notice the contribution, even in such damped events, to the production of symmetrical masses. It is very unlikely that these fragments were formed in fusion-fission processes: the TKE value predicted by Viola systematics for the symmetric case should be 321 MeV, lower than all TKE values

measured (Fig. 2.7) and the large value of the Coulomb factor for the couple Xe and Pb makes it difficult for the fusion to happen.

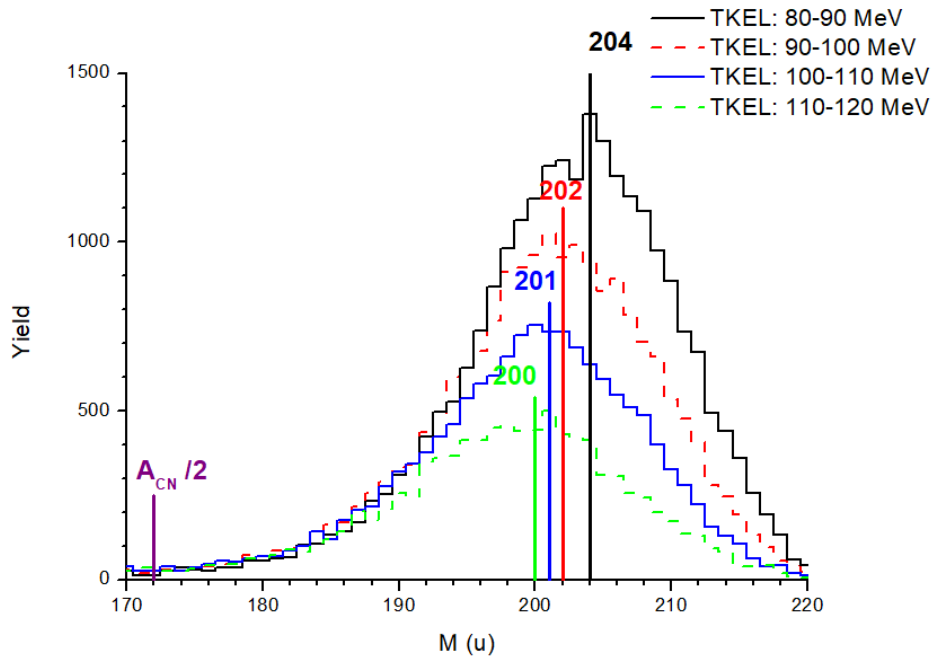


Figure 2.11: Primary TLF mass distributions obtained after window selection in TKEL distribution. The ranges 80-90 MeV (black line), 90-100 MeV (red line), 100-110 MeV (blue line) and 110-120 MeV (green line) are related to mass distributions peaked on 204, 202, 201 and 200 u respectively. There is a mark on half the mass of CN to show the possibility of production of symmetric fragments.

This kind of selection was performed over the TKEL distribution, ranging from -45 to 165 MeV. Each selection led to a TLF mass distribution whose centroid and width are schematically shown in the plot of Fig. 2.12. Fig. 2.13 represents the trend of the yield of TLF mass distributions depending on TKEL window, the mass related to the each window is shown. Colored lines show the change in the trend in the mass region of interest: the graph shows an increment of events with respect to the trend of the red line. This means that in this region the shell effects, in particular due to neutro shell closures, are sensibly affecting the mass transfer. A similar effect was already observed in other systems [29].

In order to provide further evidences about the production of mass 202, the results of the analysis of PRISMA Ionization Chamber data will follow. The

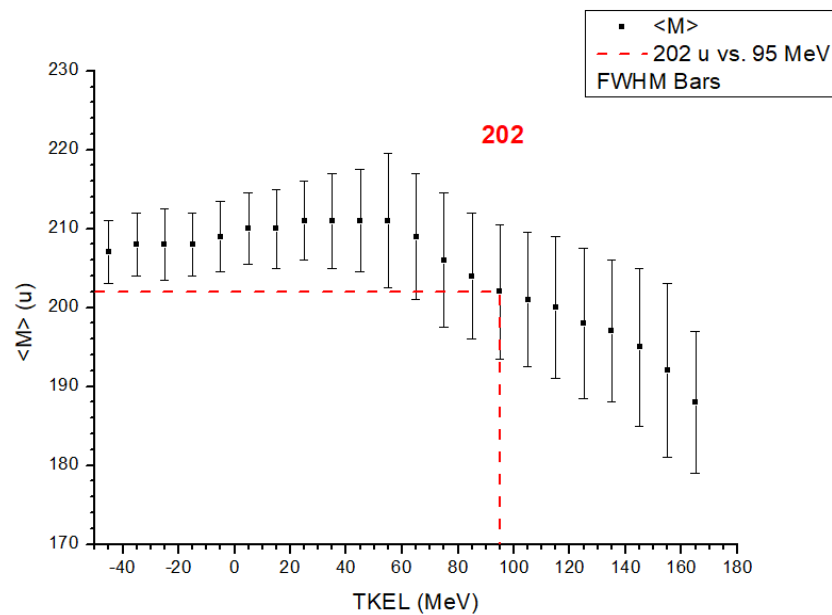


Figure 2.12: TLF mass distribution peaks and FWHMs depending on the choice of the TKEL window. There is a change in the trend around the mass 202 u.

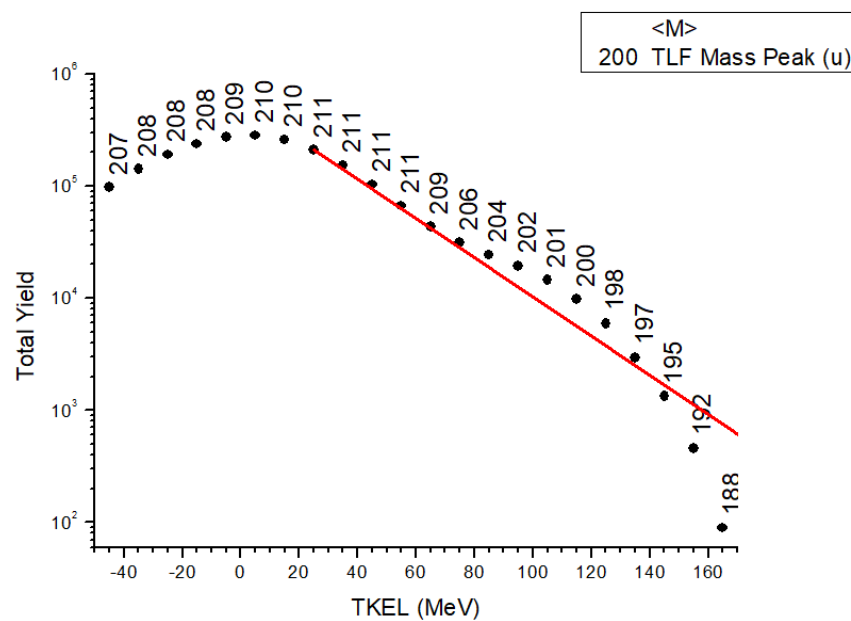


Figure 2.13: Trend of the yield of TLF mass distributions depending on TKEL window. Red line shows that there is a change in the trend in the mass region of interest, a signature of shell effects.

setup is designed to accept mostly PLFs and, among the possibilities, the ΔE stage is considered to be played by the first section of the IC (App. A.3.1).

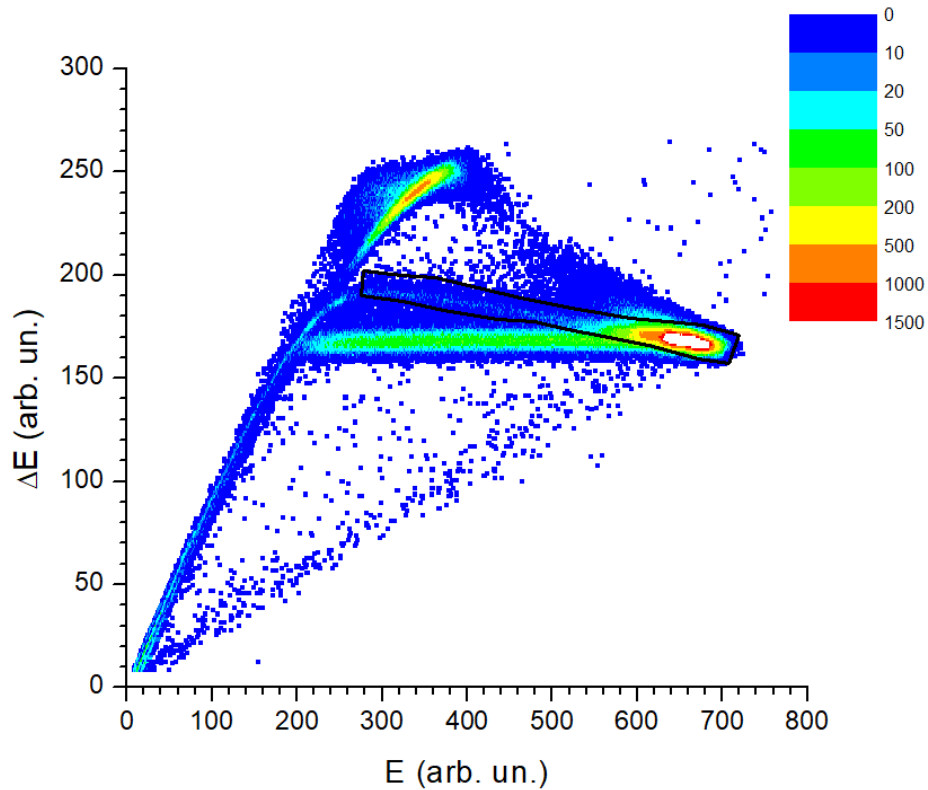


Figure 2.14: E- ΔE matrix concerning the PLFs flying in PRISMA arm, the ΔE stage is considered to be played by the first section of the IC (App. A.3.1). The black contour delimits the area in which it is possible to find the PLFs of interest. Elastic events overlap with other channels.

Fig. 2.14 shows the E- ΔE matrix concerning the PLFs flying in PRISMA arm. The black contour delimits the area in which it is possible to find the PLFs of interest, as it will be shown. By applying a gate (the black contour) on the E- ΔE matrix and a cut on TKEL distribution (values greater than 80 MeV), the result in Fig. 2.15 is obtained.

At this point, by looking at the PLF M-TKEL matrix for such damped events (TKEL > 80 MeV) in Fig. 2.16, there is a noticeable presence of events in the area with $M > 140$. If a gate is applied (black contour in the matrix), the distribution in Fig. 2.17 is the result. The red curve superimposed on the distribution of PLF

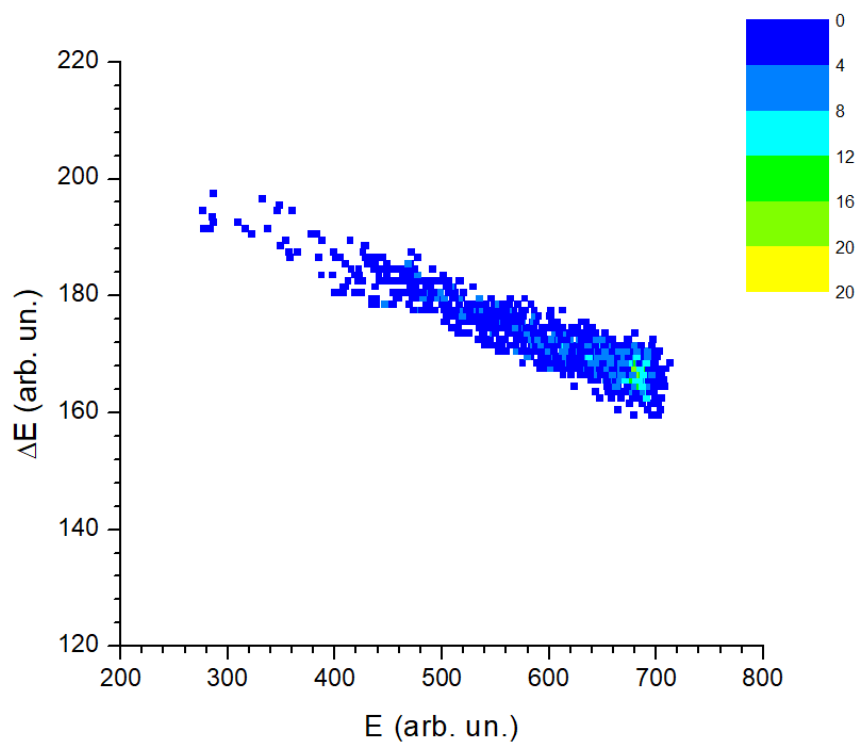


Figure 2.15: E- ΔE matrix obtained by application of the black contour gate and a cut on TKEL distribution (TKEL > 80 MeV), in this way it is possible to discard elastic and QE events.

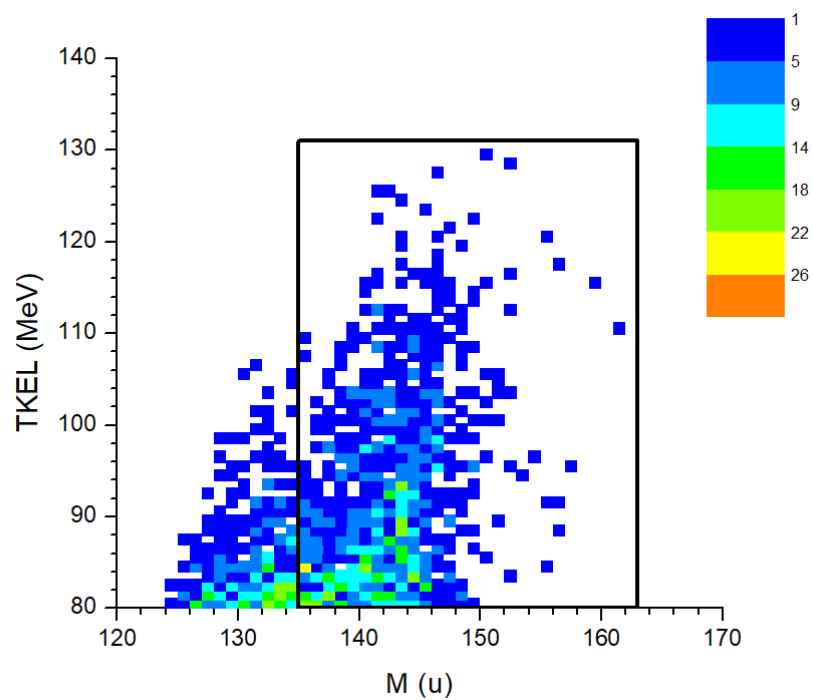


Figure 2.16: M-TKEL matrix of the projectile-like fragments in very damped events ($\text{TKEL} > 80$ MeV). The area in the black contour contains events around the aimed mass.

masses is a gaussian fit, the centroid is found to be 142 u. As stressed before, a mass of 142 u could belong to ^{142}Nd , product of a 6-proton transfer from ^{208}Pb (becoming ^{202}Os) to ^{136}Xe .

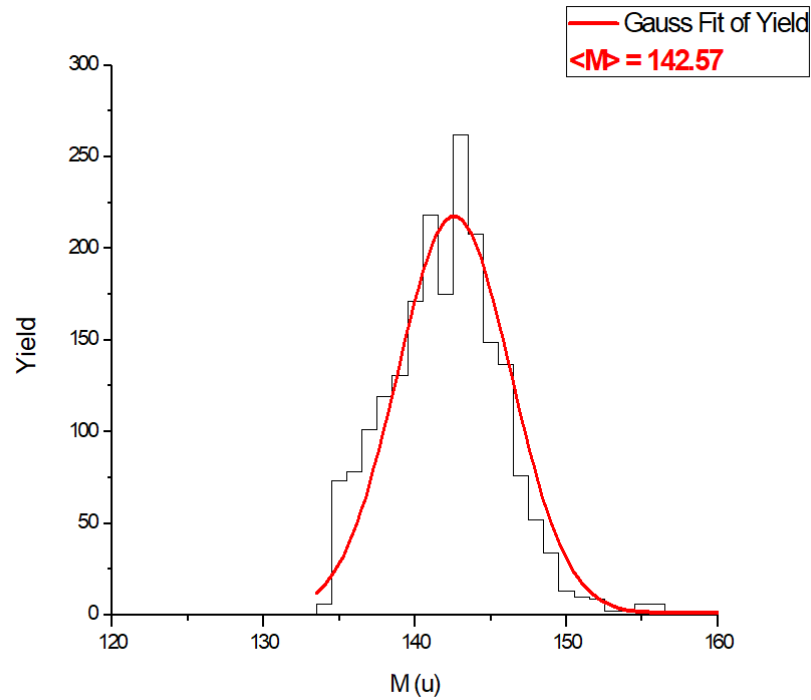


Figure 2.17: Mass distribution of PLF after application of gates on E- Δ E (Fig. 2.14) and M-TKEL (Fig. 2.16) matrices. The red curve is a gaussian fit with a centroid in 142 u.

	N	Z	TLF Product
a)	0	6	^{202}Os
b)	1	5	^{202}Ir
c)	2	4	^{202}Pt
d)	3	3	^{202}Au
e)	4	2	^{202}Hg
f)	5	1	^{202}Tl

Table 2.1: All possible configurations of 6 nucleon transfers, including at least one proton, leading to elements different from the projectile and target.

The resolution of the IC does not allow to identify the charge of the detected fragments, thus the production of ^{142}Nd (and ^{202}Os) is just one among six possible 6-nucleon transfers, involving at least one proton.

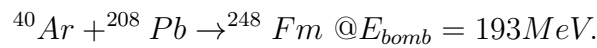
Chapter 3

NRO127 JYFL Experiment

3.1 Scientific Motivation

The aim of the experiment, carried out at JYFL laboratories, was to explore the possibility of simultaneous ternary decays in reactions induced at energies around the Coulomb barrier. Unlike spontaneous fission, a nuclear reaction would allow to reconstruct masses and energies through the kinematics thanks to the possibility to detect all the fragments.

The following reactions were explored in order to study both ternary and binary decay (the latter to be used as reference):



The bombarding energies were chosen according to the Coulomb barrier expected for the specific entrance channel. Relevant information are showed in tab. 3.1, where V_B is the height of the barrier in the Bass parametrization [24] and the excitation energy is evaluated as the sum of Q_{fus} (fusion Q-value) and E_{CM} (available energy in CM reference).

	MeV	MeV	MeV	MeV	MeV	deg
Reaction	E_{lab}	E_{CM}	V_B	Q_{fus}	E_{CN}^*	$\theta_{grazing}$
$^{37}\text{Cl} + ^{208}\text{Pb}$	195	165.6	154.0	-119.9	45.7	103.2
$^{37}\text{Cl} + ^{205}\text{Tl}$	195	165.2	152.4	-115.0	50.2	99.9
$^{40}\text{Ar} + ^{205}\text{Tl}$	193	161.5	160.2	-125.2	36.3	132.9
$^{40}\text{Ar} + ^{208}\text{Pb}$	193	161.5	161.8	-126.2	35.3	141.1

Table 3.1: Table of the most relevant quantities concerning the reactions. $E_{CN}^* = Q_{fus} + E_{CM}$.

For all the above reactions, several shell closures may favor the decay into three fragments if the excitation energy is kept low enough allowing the persistence of the shell effects, hence the choice of a bombarding energy near the Coulomb barrier height. Shell effects should be also considered from the reaction time point of view: nucleon transfer may be more facilitated by starting from nuclei without shell closures. In other words, the relation between reaction time and nucleons rearrangements is a crucial point. Thus, the comparison between the different reactions may provide further information on the mass transfer probability (toward closed shells) in relation to the characteristics of the entrance channel.

Similarly to other experiments aimed at the construction of a M-TKE distribution, also in this case the observables of choice for these reactions are the velocity vectors of the fragments.

It is possible to detect the binary fragments traveling in forward directions by placing two arms of a time of flight spectrometer symmetrically around the beam at the folding angle prescribed for symmetric decay by Viola systematics (Fig. A.1 Appendix A.1). Asymmetric decays are detected anyway thanks to detector openings.

Concerning the ternary decay, the configuration chosen for the setup allows the detection of (almost) only in-plane kinematics. Because of the available detectors (described in the following section), it was possible to detect the velocity

vectors of only two out of three fragments, namely the ones in forward directions, while the third fragment (backward) would have been detected with its energy in silicon detectors. Fig. 3.1, 3.2, 3.3 [33] show the expected in-plane 3-body kinematics for the reaction $^{37}\text{Cl} + ^{208}\text{Pb} \rightarrow ^{132}\text{Sn} + ^{65}\text{Cu} + ^{48}\text{Ca}$: two fragments, with different masses, are detected at forward angles, at a folding angle smaller than the one of the binary fission, and the third fragment at a backward angle.

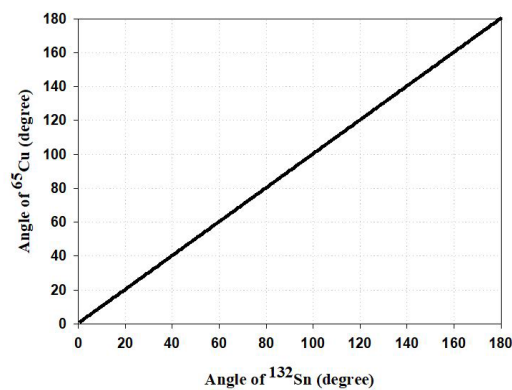


Figure 3.1: Kinematics plot for symmetric fission and for a typical 3-body decay of interest. ^{132}Sn vs. ^{65}Cu [33].

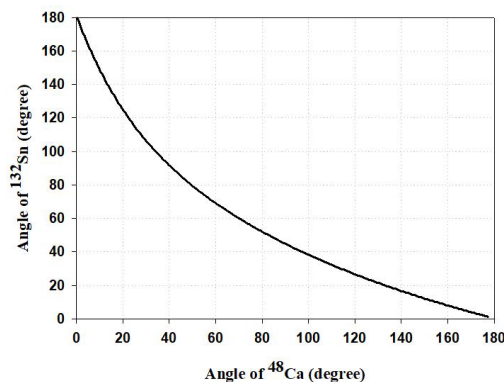


Figure 3.2: Kinematics plot for symmetric fission and for a typical 3-body decay of interest. ^{132}Sn vs. ^{48}Ca [33].

The geometrical configuration and triple coincidence logic, along with a proper analysis of the kinematics, allows to remove ternary coincidences coming from sequential decays, since the angular distribution is squeezed in the

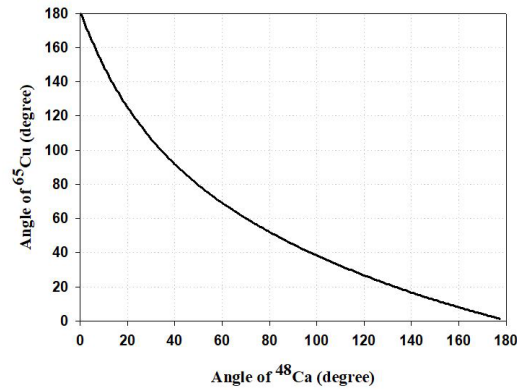


Figure 3.3: Kinematics plot for symmetric fission and for a typical 3-body decay of interest. ^{65}Cu vs. ^{48}Ca [33].

forward hemisphere, because of center of mass motion boost. There is, thus, almost no possibility that by kinematics or energy range a the detection of two out of three fragments in the forward hemisphere can be misidentified as coming from a sequential 3-body decay. Fig. 3.4 shows a typical sequential 3-body decay velocity diagram and in Fig. 3.5 is depicted the optimal detection geometry that allows to identify unequivocally a true ternary decay.

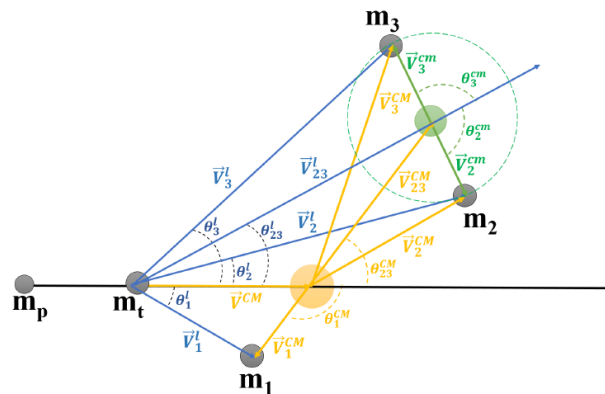


Figure 3.4: Velocity diagram for a 3-body sequential fission.

Energy - angle correlations further help in disentangling direct from sequential ternary decay. Fig. 3.6 shows angular correlation of a possible 3-body final state in terms of the energy of the third fragment [33]: clearly, looking for the heavier ones at angles around 40° , would force the third fragment in very backward angles with unequivocally high energy. The latter information is of

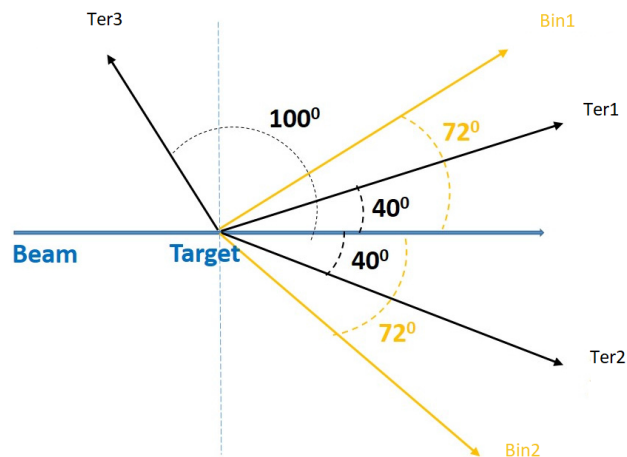


Figure 3.5: Proposed detection geometry for the binary and ternary decays.

paramount importance also from technical point view, namely for the dynamical range setting of the silicon detectors.

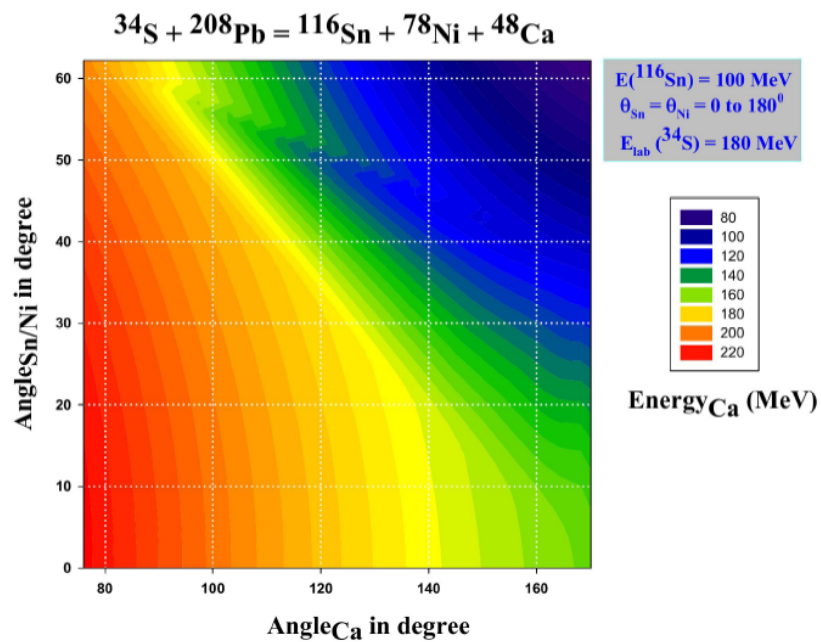


Figure 3.6: Angular correlation of three (^{132}Sn , ^{65}Cu , and ^{48}Ca) fragments in terms of ^{48}Ca energy [33].

Another important signature of a true three body decay would be the observation of multiple kinematics solutions (Fig. 3.7, 3.8).

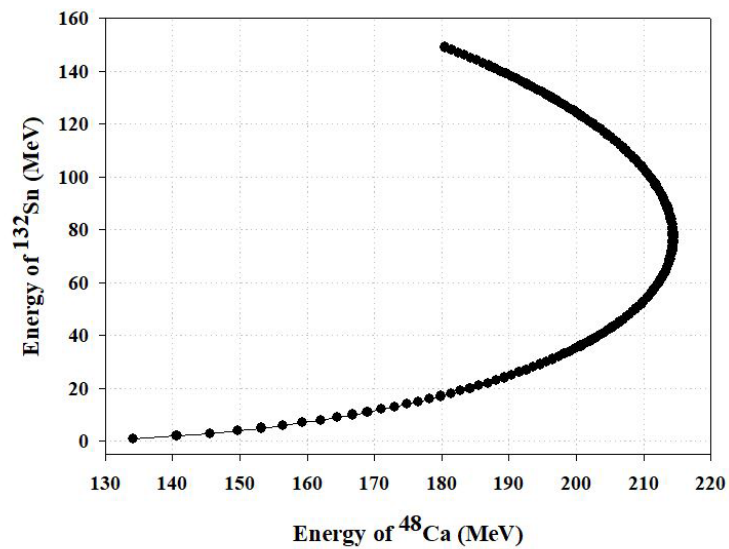


Figure 3.7: Double kinematics energy solution for ^{132}Sn for a fixed energy of ^{48}Ca [33].

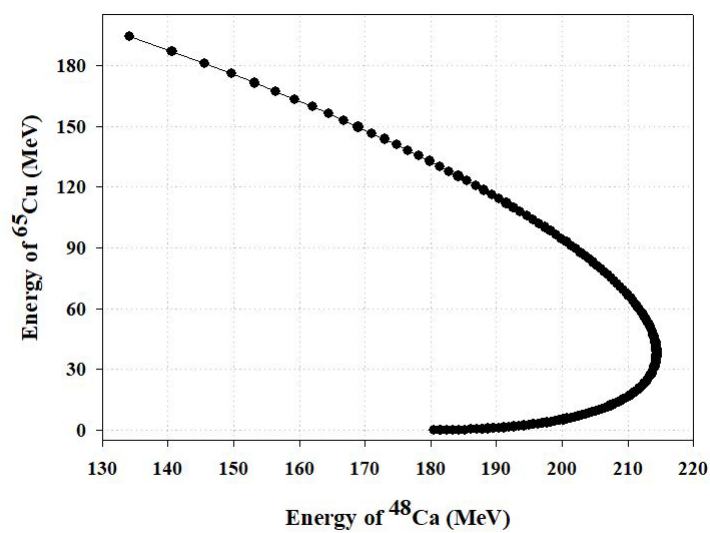


Figure 3.8: Double kinematics energy solution for ^{132}Sn for a fixed energy of ^{48}Ca [33].

Fig. 3.9 shows the angular correlation of fragments of a direct binary decay in the reaction $^{37}\text{Cl} + ^{208}\text{Pb}$ (see also App. A.1 and B.2). The black rectangle represents the angular coverage of the detectors placed at 65° and -65° in order to detect binary fission fragments: it is clear how binary decay cannot pollute the data collected by detectors placed at 40° and -40° .

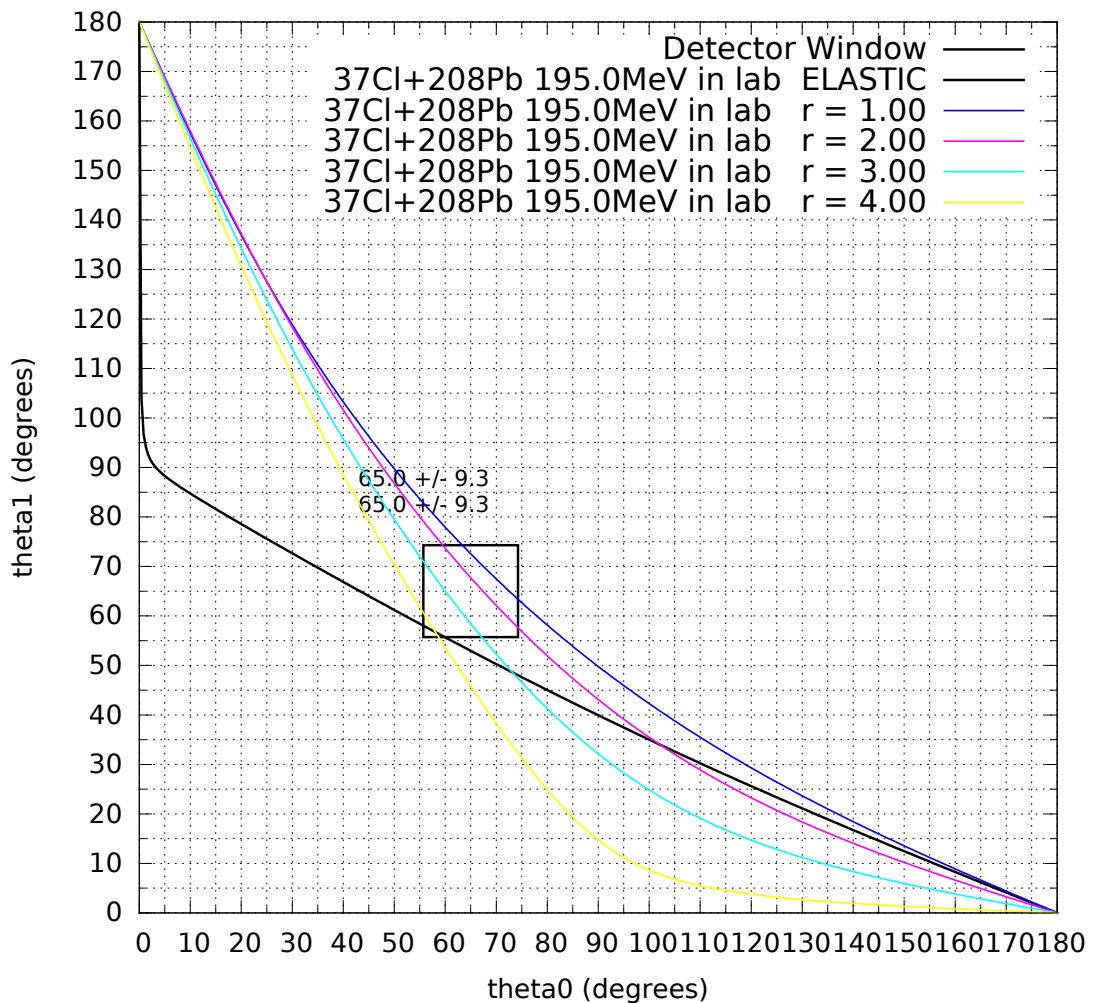


Figure 3.9: Angular correlation of fragments of a binary decay (App. A.1 and B.2) in the reaction $^{37}\text{Cl} + ^{208}\text{Pb}$, showing where to find a fragment once the angle of the other is fixed. Colored curves represent the correlation for some fixed value of the fragment mass ratio r . The black rectangle represents the angular coverage of the detectors placed at 65° and -65° .

3.2 Experimental Setup

The key feature of the setup developed and used for this experiment is its small size, simplicity and portability. The setup consists of:

- a four arms Time of Flight MCP based spectrometer, CORSET (CORrelation SETup), each including:
 - Start Detector (3×2.2 and 2.2×2.2 cm² sensitive area) providing a timing signal;
 - Stop Detector (8.6×6.9 cm² sensitive area) providing a timing signal and two coordinate signals (X and Y of the point hit by a particle);
- silicon detectors, used for energy measurement of charged particles:
 - six with a thickness of $300 \mu\text{m}$, 5×5 cm², in the backward hemisphere;
 - three $20 \mu\text{m}$, covered by a 1 cm diameter circular collimator, used as ΔE stage of as many telescopes, in the backward hemisphere;
 - three $50 \mu\text{m}$, covered by a 1 cm diameter circular collimator and aluminum foil absorber, used as beam monitors.

CORSET is a mass spectrometer used for measuring TOFs in coincidence. The four arms of the present version were placed symmetrically around the beam line and working in coincidence two-by-two (see Fig. 3.10): the one at 65° (arm 0) with the one at -65° (arm 3), the one at 40° (arm 1) with the one at -40° (arm 2). The reason of this choice lies in the necessity of measuring both binary and (expected to be) ternary decays, which are interested by different output angles in the laboratory reference frame. In other words, the most external ones were used to detect binary decay, the other two to detect ternary events.

The silicon detectors coupled with CORSET are placed at very backward angles with respect to the beam line, i.e. where the third particle is expected to

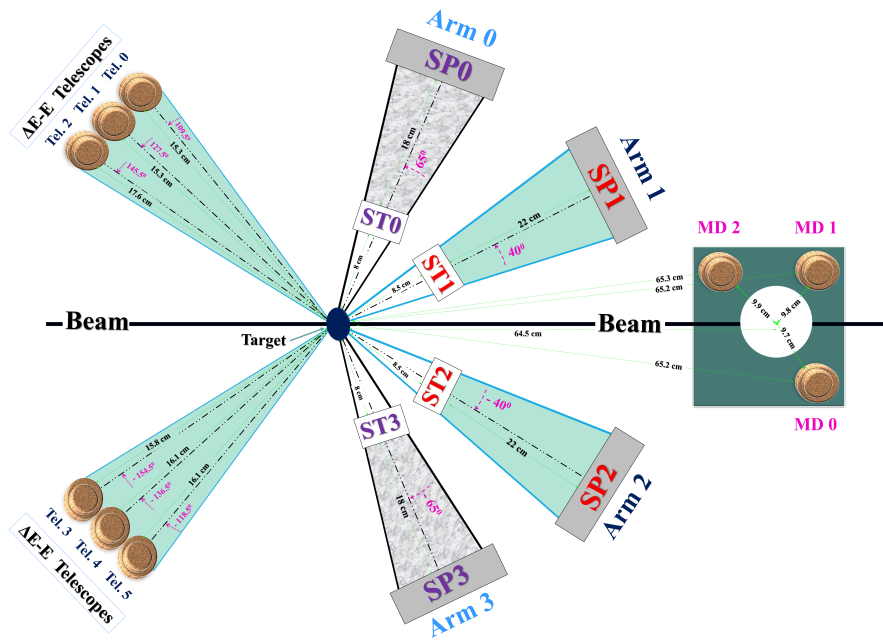


Figure 3.10: Detailed overview of the setup used in the experiment [33]. The four CORSET arms are placed at -65° , -40° , 40° and 65° respectively. Start and Stop detectors are fixed in order to have a 18 cm distance in arm 0 and 3 and 22 cm in arm 1 and 2. The telescopes are placed at backward angles 109.5° , 127.5° , 145.5° , -154.5° , -136.5° , -118.5° respectively from Tel. 0 to 5.

be observed: 109.5° , 127.5° , 145.5° , -154.5° , -136.5° , -118.5° respectively from Tel. 0 to 5.

Each TOF arm consists of a MCP based Start (ST) and position sensitive Stop detector (SP). The first consists of a conversion foil, an accelerating grid, an electrostatic mirror and a chevron MCP assembly. The second is composed of a conversion entrance foil, a chevron assembly of two MCPs and coordinate system. The distance between start and stop is fixed during the mounting and affects the final mass resolution. The covered solid angle, thus the rate of particle impinging on the detector, depends on the distance between target and Stop detector. The chosen distances are showed in Tab. C.5. The TOF is found as difference in time between the timing signals coming from ST and SP detectors.

The backward silicon detector are used both in single and in E- Δ E combination: while the thick detectors are placed almost symmetrically around the

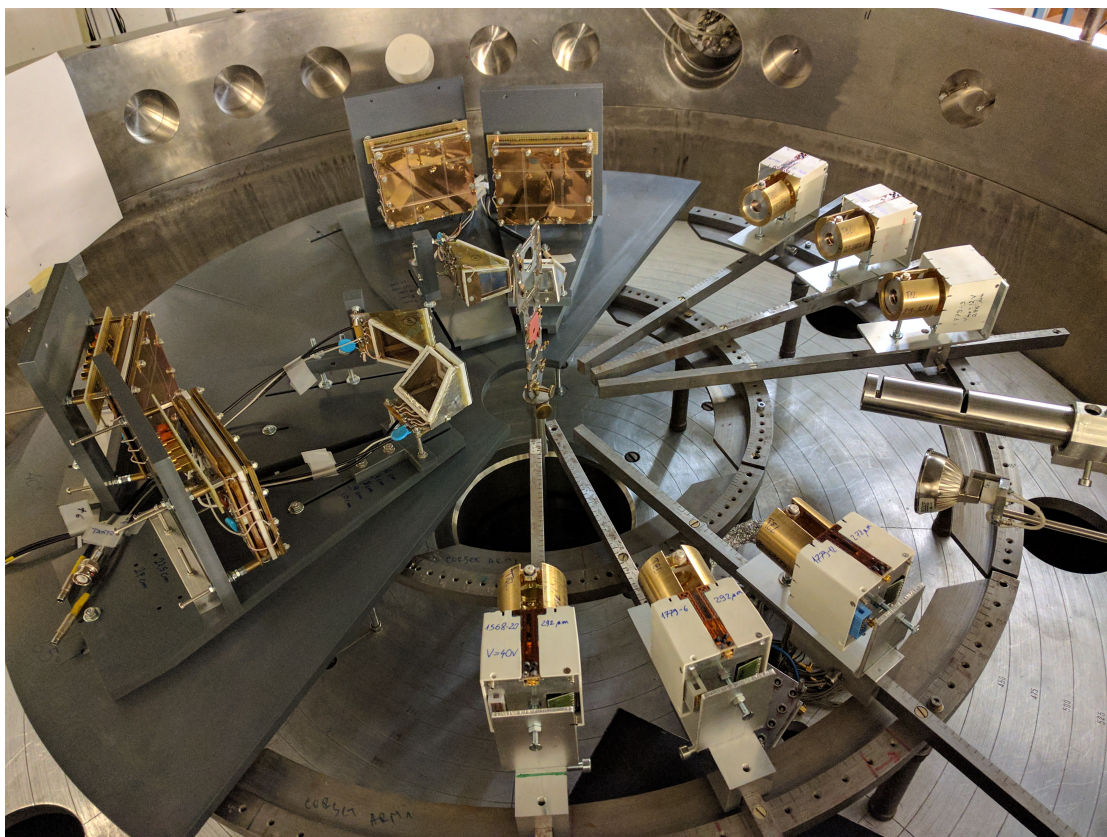


Figure 3.11: Photograph of the actual setup and scattering chamber mounted at JYFL, taken during the mounting phase. On the right it is noticeable the end of the beam pipeline. A target holder is placed in the center. Clockwise from the pipe there are: three silicon detectors, TOF arms from 0 to 3, three silicon detectors.

beam line, only one side is equipped with the thin ones, namely detectors from 3 to 5 (see Fig. and Tab. C.6). Where present, the ΔE stage function is performed by 20 μm thick Ortec silicon detectors. The large size and small distances of the E detectors allow to cover a larger solid angle, thus a larger angular range, but on the other hand it worsen the angular resolution, see Tab. C.6.

Three 50 μm silicon detectors plus 30 μm aluminum absorbers, installed around the beam line, were used for online and offline monitoring of beam properties and, possibly, for cross section evaluation by ratio to Rutherford scattering of projectile on target. Tables in App. C show the main parameters of the setup.

3.3 Results and Discussion

3.3.1 Binary Decay

In this section the results of the analysis (see App. A, A.3.5 for the analysis procedure) on binary decay data (from arm 0 and arm 3 at -65° and 65° respectively) will be shown.

This analysis can be considered as a parallel, separate experiment concerning reactions nowadays still not explored and serve as a reference for the ternary decay analysis, as it will be shown in Par.3.3.2.

The experimental V_{par} - V_{per} matrix for the reaction $^{37}\text{Cl} + ^{208}\text{Pb}$ is reported in panel a) of Fig. 3.12, along with the FMT events gate. It is important to notice the shape of the graph, typical for binary decay (see also Fig. 2.6)The matrix is populated by binary events with a central, more populated, spot given by FMT events having $V_{par} \sim V_{cm}$ and $V_{per} \sim 0$, while all data around can be interpreted as prescribed in App. A.3.5.

After the application of the gate on the matrix, as stressed also in Par. 2.3 and App. A.3.5, the M-TKE distribution of panel b) is obtained.

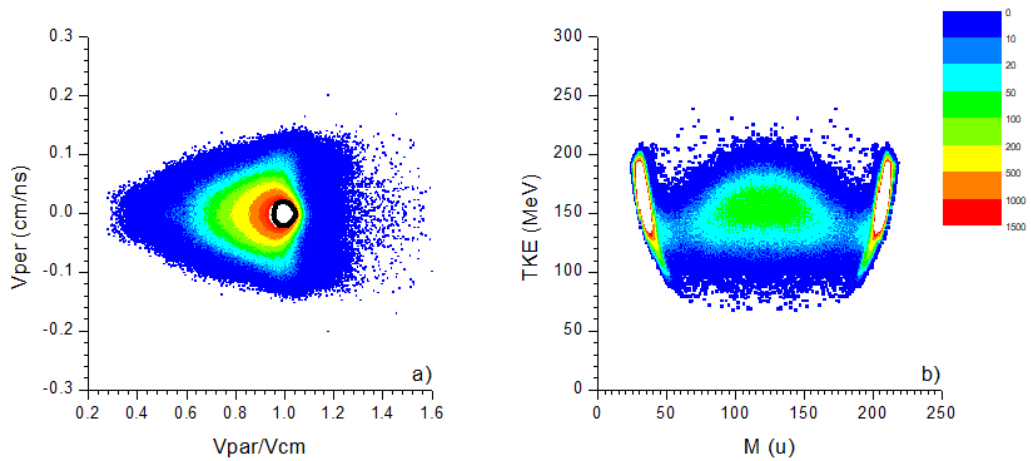


Figure 3.12: a) Experimental $V_{par}-V_{per}$ matrix for the reaction $^{37}\text{Cl} + ^{208}\text{Pb}$ @ $E_{lab} = 195$ MeV. The Black curve represents the gate applied for the selection of FMT events. b) Experimental M-TKE matrix for the same reaction. Quasi-Elastic *loci* are present on the sides, the fission fragment area is centred around the mass of the symmetric division of Compound Nucleus and energy prescribed by Viola systematics [A.1](#).

The following figures show the data concerning the remaining reactions.

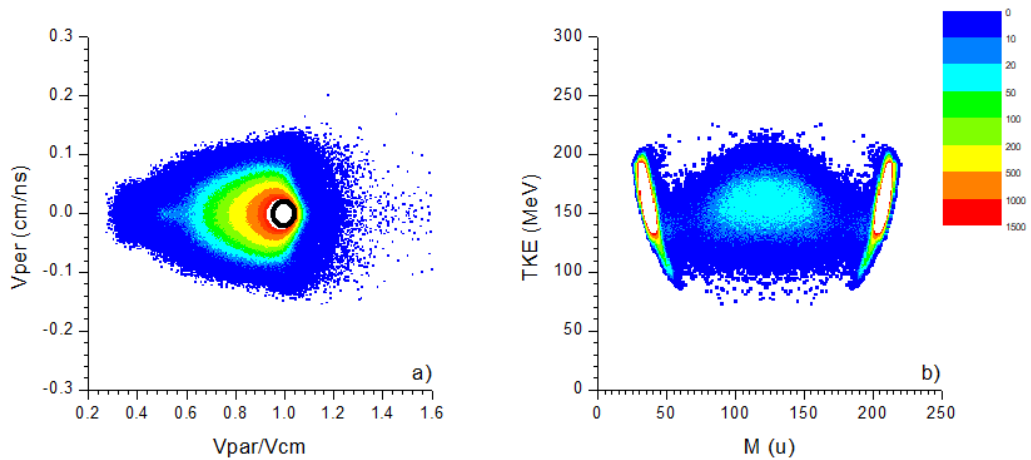


Figure 3.13: a) Experimental $V_{par}-V_{per}$ matrix for the reaction $^{40}\text{Ar} + ^{208}\text{Pb}$ @ $E_{lab} = 193$ MeV. b) Experimental M-TKE matrix for the same reaction.

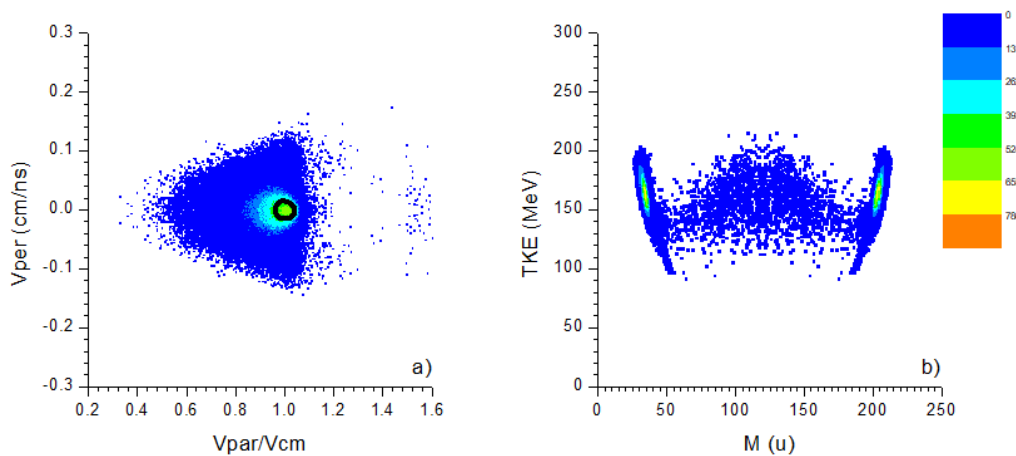


Figure 3.14: a) Experimental $V_{par}-V_{per}$ matrix for the reaction $^{37}\text{Cl} + ^{205}\text{Tl}$ @ $E_{lab} = 195$ MeV. b) Experimental M-TKE matrix for the same reaction.

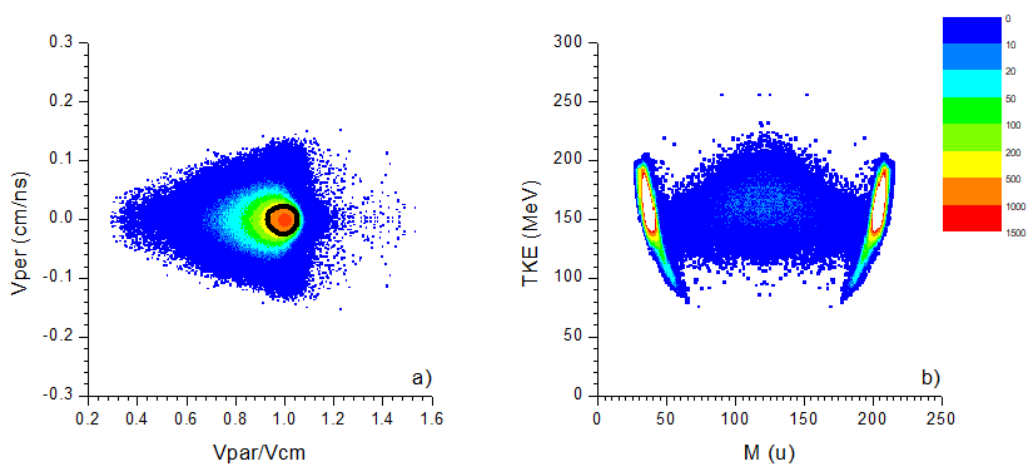


Figure 3.15: a) Experimental $V_{par}-V_{per}$ matrix for the reaction $^{40}\text{Ar} + ^{205}\text{Tl}$ @ $E_{lab} = 193$ MeV. b) Experimental M-TKE matrix for the same reaction.

3.3.2 Ternary Decay

The measured quantities, mostly related to the kinematics of the reactions, allow to perform several tests in order to rule out possible interpretations of data as non-ternary decay. In Appendix A.3.6 these tests are discussed in slightly more detail.

In the first steps of the analysis signatures of ternary decay will be searched in the measurement of only two fragments in CORSET arms 1 and 2 (at -40° and 40° respectively).

Results follow below with a detailed explanation. In the next sections, data coming from preliminary measurement runs performed in June 2017 (discussed in [34]) and February 2018 are shown together as they consistently overlap. A detailed description is provided for the results of $^{37}\text{Cl} + ^{208}\text{Pb}$, while is omitted for the other reactions since the analysis methods are the same. It as to be mentioned that the best results are those from the reaction $^{40}\text{Ar} + ^{208}\text{Pb}$, because of their match with the simulations appears to be better than the other reactions.

3-body Interpretation of the Kinematics of Two Fragments

Fig. 3.16 shows the $V_{par}-V_{per}$ matrix obtained using the velocities measured through CORSET arms 1 and 2 during the reaction Cl + Pb. By comparison with Fig. 3.12, panel a), it is clear that there is a deep difference which can be considered as a hint of the non-binary nature of these events.

The kind of structure found for binary decays is absent in Fig. 3.16 that, in turn, shows the presence of many *loci* at several values of $V_{par}/V_{cm} > 1$ (but also including $V_{par}/V_{cm} \sim 1$) and a wide V_{per} distribution. Each of these *loci* is related to a region of the velocity matrix.

Fig. 3.17 shows the velocity matrix of fragments measured by CORSET arms 1 and 2. The colored contours represent the areas related to a specific *locus* of

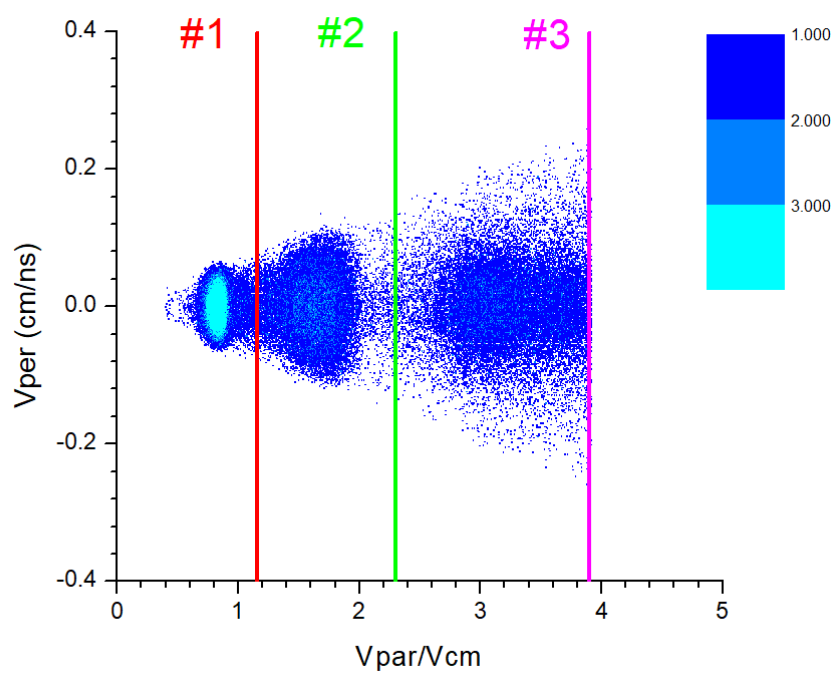


Figure 3.16: V_{par} - V_{per} matrix obtained using the velocities measured through CORSET arms 1 and 2, in $^{37}\text{Cl} + ^{208}\text{Pb}$. Many *loci* at several values of $V_{par}/V_{cm} > 1$ are present, suggesting the non-binary nature of the events.

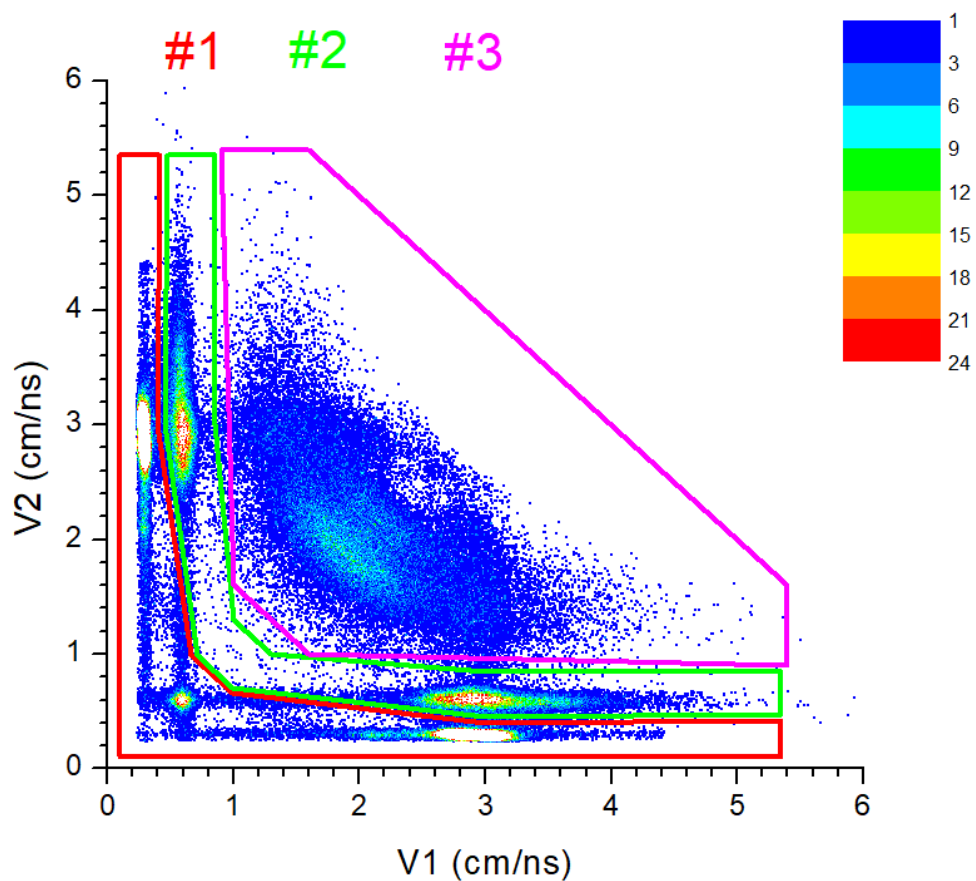


Figure 3.17: Distribution of the velocities measured in CORSET arms 1 and 2, in $^{37}\text{Cl} + ^{208}\text{Pb}$. Several *loci* can be noticed and are related to the ones in $V_{par}-V_{per}$ matrix in Fig. 3.16. The link between the areas is marked by the color system of the contours.

the $V_{par}-V_{per}$ matrix in Fig.3.16. Area #1 and #2 represent events caught in random coincidence, respectively elastic scattering and sequential fission. Area #3 contains ternary decays (according to the present interpretation). Other observables relevant to distinguish between 2- and 3-body decays are the relative angle between the velocity vectors of the detected fragments.

Fig. 3.18 represents the distribution of relative angles (between fragment 1 and 2 velocity vectors). In a binary, full momentum transfer reaction, a distribution centered at 180° is expected. The three peaks are directly linked to the *loci* in $V_{par}-V_{per}$ matrix (thus in V_1-V_2 matrix), from right to left:

1. a peak linked to the *rightmost* area in $V_{par}-V_{per}$ matrix (ternary events);
2. a peak linked to the *central* area in $V_{par}-V_{per}$ matrix (sequential fission/random);
3. a peak linked to the *leftmost* area in $V_{par}-V_{per}$ matrix (elastic/random).

It is clear that the events under investigation do not present a 180° angle between the velocity vectors but rather a smaller relative angle, less than 100° , definitely not compatible with a binary decay.

It is important to notice that the above data are not corrected for the energy loss of the fragments in target and start detector because of the lack of mass measurements. The absence of these corrections affects the velocity vector in its modulus and its orientation in the CM reference frame, so that is why the random elastic component does not appear centred on $V_{par}/V_{cm} = 1$ in $V_{par}-V_{per}$ matrix and 180° in the relative angle distribution.

In order to exclude another possible misinterpretation, the velocities above mentioned were assumed as the velocities of particles evaporated from a Compound Nucleus. Fig. 3.19 shows the reconstruction of the energy spectra in the left panel there is the conversion of velocity into alpha particle energy, in the right panel velocity into proton energy.

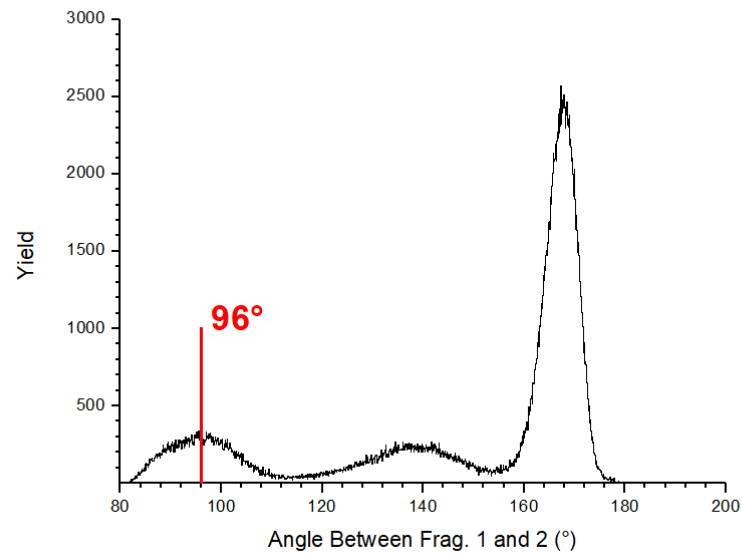


Figure 3.18: Angle between the velocities of fragment 1 and 2 in CM reference frame in $^{37}\text{Cl} + ^{208}\text{Pb}$. In a binary, FMT reaction this angle should be distributed around 180° due to momentum conservation law. The red line marks the peak linked to the supposed-to-be ternary events.

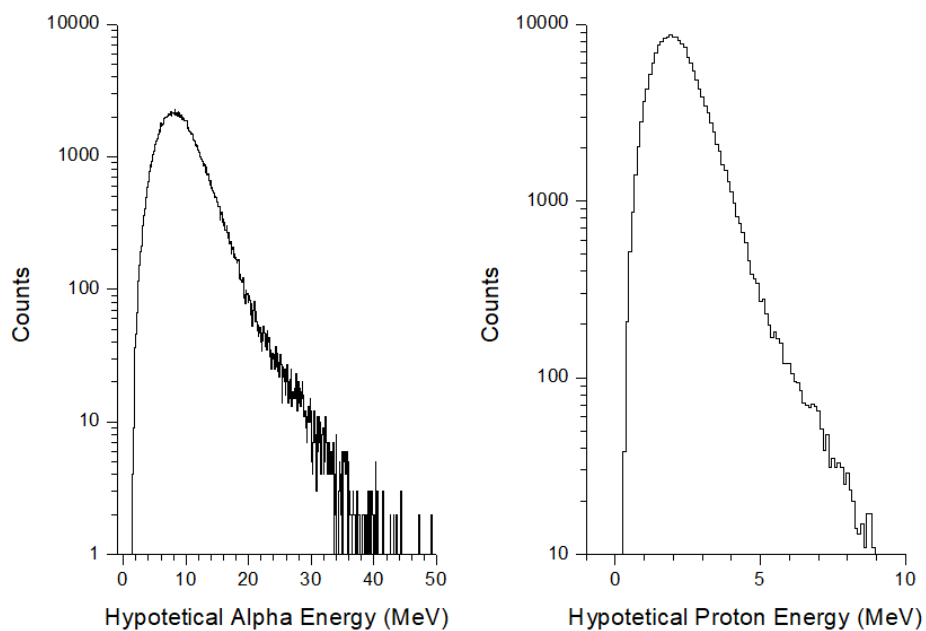


Figure 3.19: Data concerning reaction $^{37}\text{Cl} + ^{208}\text{Pb}$. Left panel: conversion of measured velocity into alpha particle energy. Right panel: conversion of measured velocity into proton energy.

It is possible to notice that the peak of "hypothetical" alpha particle energy is placed below 10 MeV and for the protons it is near 2 MeV. These values are not compatible with the peaks of the Maxwellian distribution of alpha and proton evaporated from the ^{245}Es .

Moreover, such emissions would be inaccessible from the energy point of view because of the low excitation energy (see Tab. 3.1). A statistical model code LILITA simulation confirmed the presence of only neutron evaporation and allowed to exclude the possibility of alpha and proton emission from a compound nucleus obtainable by the fusion of chlorine and carbon (target backing), again because of incompatibility in the energy spectra peak.

Inclusion of the Third Particle

Figure 3.20 shows the energy spectra of fragments detected by the silicon detectors in the backward hemisphere. Beside the fact that only few events are detected in coincidence with arm 1 and 2, it can be noted that a large density of events is above 20 MeV and up to 80 MeV, while the events having energy below 10 MeV fall under the so-called "pedestal" (electronic noise). Such energy range is compatible with the kinematic prediction of a 1-step ternary decay in which a fragment flies in backward direction.

However it must be acknowledged the abundant 2-fragments coincidence in arm 1 and 2 with respect to the triple coincidence, the ones including the silicon detectors. One of the reasons could be the small solid angle coverage.

Using energy and momentum conservation laws, it is possible to build a system of three second degree equations in the variables M_1 , M_2 and M_3 [34] in order to make an estimate of masses (see App. A.3.6). A restraining condition on the total mass was not among the equations used to evaluate fragment masses so, because of error propagation, M_{tot} may be different from the compound nucleus mass. Only the cases in which $M_{tot} > 200$ (Tab. 3.2) were chosen

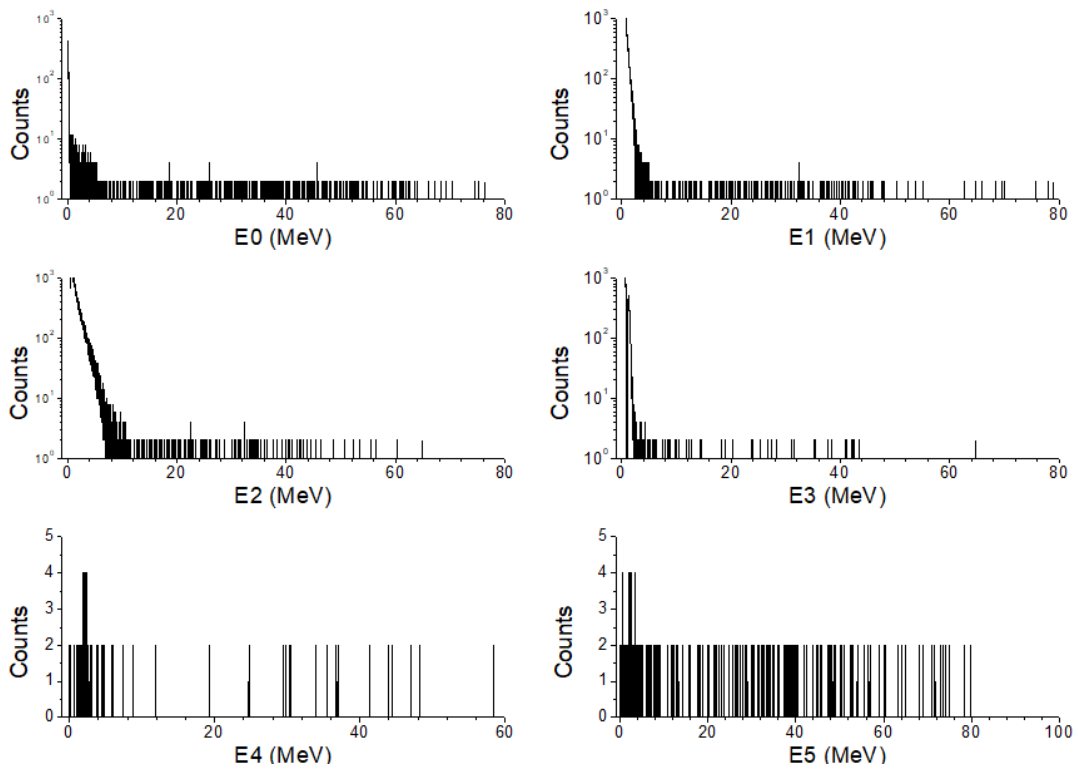


Figure 3.20: Energy spectra measured in $^{37}\text{Cl} + ^{208}\text{Pb}$ by backward silicon detectors (see App.C.2.2). High energy fragments have been detected.

in order to cut too low M_1 values. According to a rough estimate, the mass resolution for each fragment should not be smaller than 7 u. It is interesting to note how the heaviest fragment goes mostly in backward directions, a feature confirmed by the simulations, as it will be shown in the next section.

Comparison with Simulations

The successive step is the comparison between measured quantities and calculations. A direct three-body decay simulation code, based on conservation laws, produces quantities such as velocities, angles (in laboratory and CM reference frame) etc. , once entrance and exit channel are specified: projectile, target and beam energy; mass and atomic numbers of the three final fragments (the "tripartition"). The code solves the equation of 3-body direct decay only in plane providing all kinematic quantities, exploiting also a Q-value database for

MeV	u	u	u	u
E_3	M_1	M_2	M_3	M_{tot}
4.86	65	40	101	206
5.11	50	53	103	206
5.46	46	52	111	209
5.51	22	76	111	209
5.86	39	101	78	218
5.93	27	66	128	221
5.98	48	40	114	202
6.34	34	76	110	220
6.95	61	42	103	206
8.79	26	60	136	222

MeV	u	u	u	u
E_3	M_1	M_2	M_3	M_{tot}
9.00	64	42	112	218
16.71	87	17	109	213
18.62	23	116	114	253
20.39	14	92	98	204
25.11	8	131	106	245
25.13	10	103	122	235
31.23	25	85	108	218
50.90	18	128	98	244
75.54	10	110	125	245

Table 3.2: A selection of results of the mass reconstruction in $^{37}\text{Cl} + ^{208}\text{Pb}$.

all possible configurations involving at least two doubly magic final fragments having $A_3 \geq A_2 \geq A_1$.

As it was already stressed in Fig. 3.18, the distribution of fragments 1 and 2 relative angle in CM frame appears to be far from 180° (typical for binary decay). The comparison between the relative angle spectrum for events in gate #3 (ternary events, Fig. 3.17) and the calculations will be discussed below.

Fig. 3.21 shows the experimental distribution of relative angles (in red) and the calculated one (black). They do not match at a first glance, but it has to be taken into account the fact that the calculated spectrum contains all possible triples having at least two doubly magic nuclei and each triple counts with the same weight, including those with a heavy fragment flying in forward directions. To understand which one contributes a selection, triple by triple, is needed.

Fig. 3.22 shows six tripartitions, chosen because of their good match with experimental data. It has to be noted that all those configurations have light fragments flying in forward directions, with the third, heavier one going backward. In most cases, the two light fragments are doubly magic, with the only exception of ^{132}Sn , and quite similar masses. The resemblance in the shape is visible, even considering the absence of energy loss corrections.

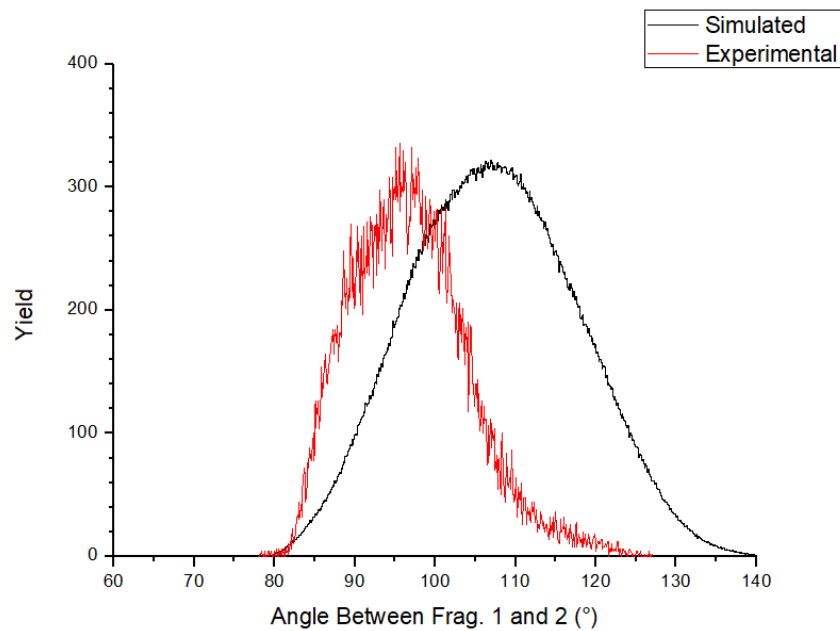


Figure 3.21: Superposition of experimental spectrum (red) of relative angles in CM reference frame, measured in Cl + Pb, with the calculated one (black). Latter includes all possible triples having $A_3 \geq A_2 \geq A_1$ and two doubly magic nuclei, including those with a heavy fragment flying in forward directions.

In Fig.3.23 there is the relative angle - V_{par} matrix, to compare experimental and calculated data. The resemblance confirms the similarities noticed in Fig. 3.22.

Another comparison is carried out between the measured velocity matrix V_1 - V_2 and the homologue calculated data. In Fig. 3.24 calculated velocities are represented by black curves, well matching experimental data. It has to be remarked the absence of energy loss corrections that would shift the matrix data slightly towards the top-right corner and would improve the matching of the data.

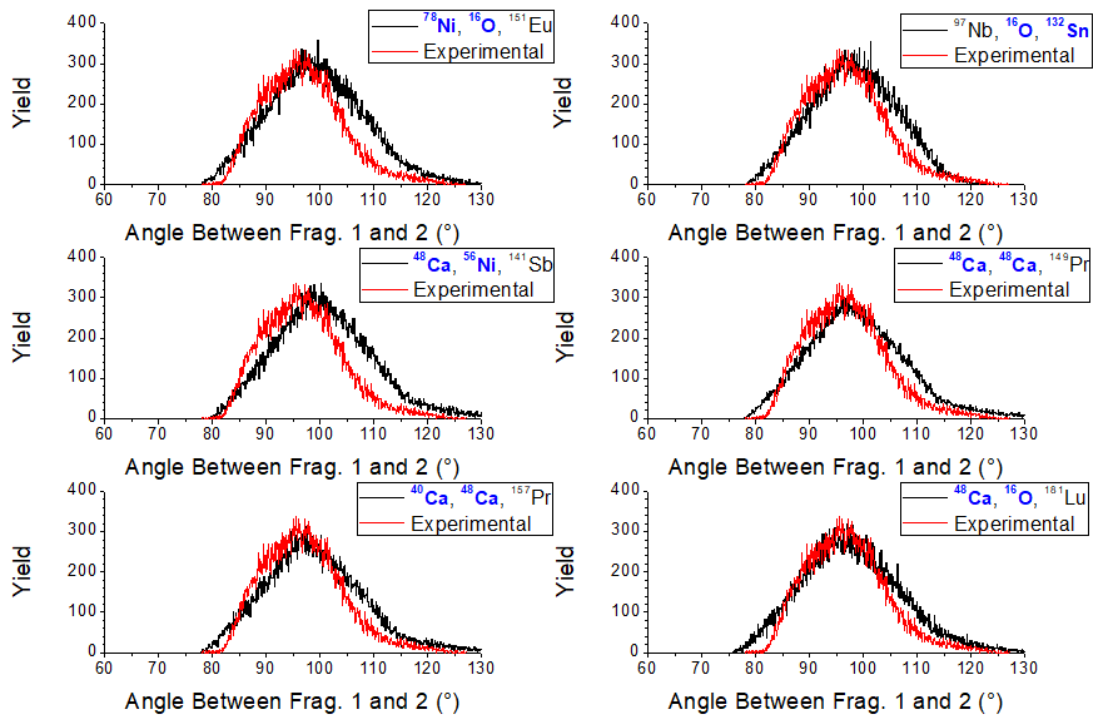


Figure 3.22: In red: experimental distribution of relative angles, measured in $^{37}\text{Cl} + ^{208}\text{Pb}$. In black: calculated distribution for indicated triple. Doubly magic nuclei are highlighted in blue characters. Most triples have light, doubly magic nuclei flying forwards and the heaviest backwards.

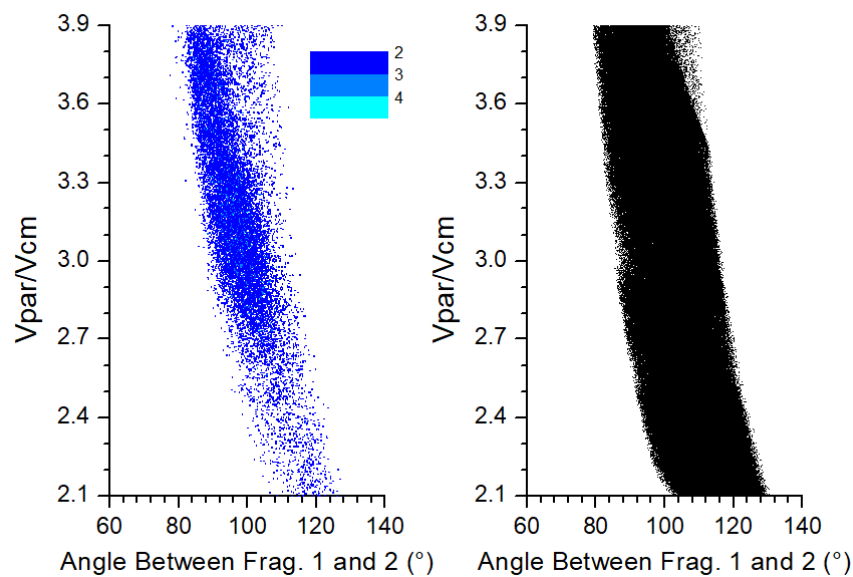


Figure 3.23: Left panel: experimental relative angle - V_{par} matrix measured in $^{37}\text{Cl} + ^{208}\text{Pb}$. Right panel: calculated one (with no intensity).

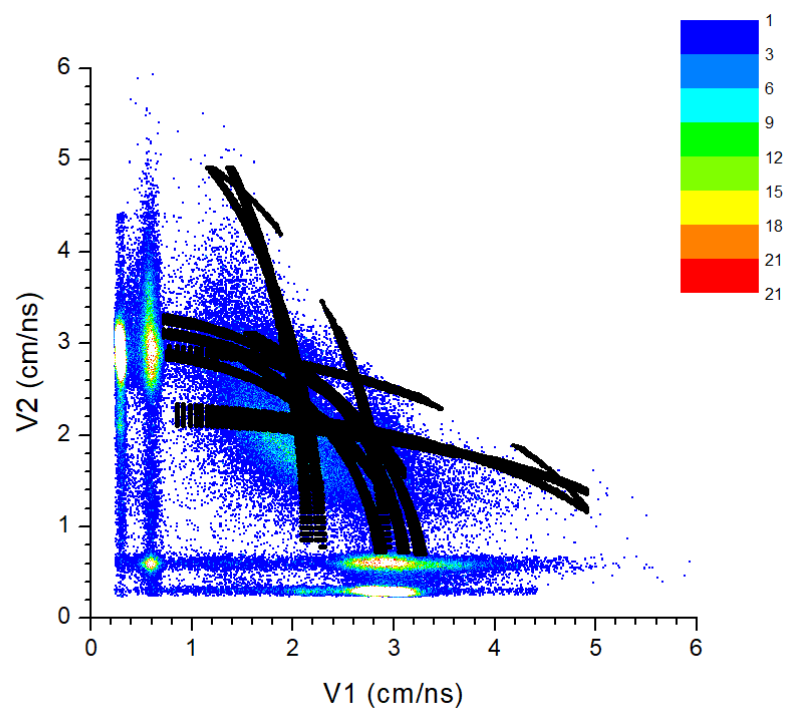


Figure 3.24: Distribution of the velocities measured in CORSET arms 1 and 2, in $^{37}\text{Cl} + ^{208}\text{Pb}$. The black curves are calculated velocities, well overlapping the experimental data.

Other Reactions Results

The following figures refer to results of $^{40}\text{Ar} + ^{208}\text{Pb}$ data analysis.

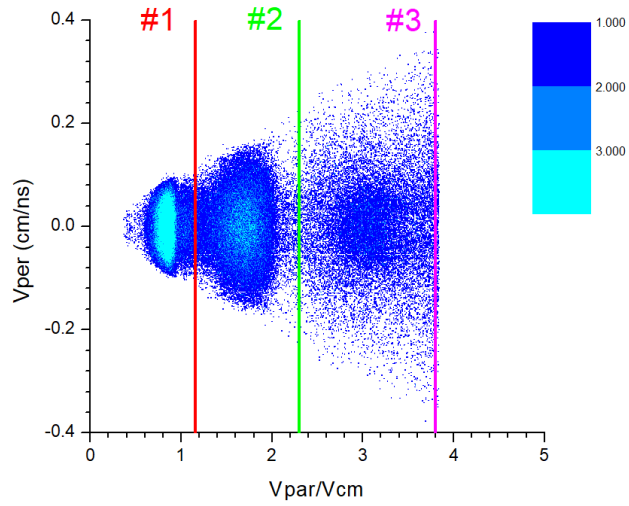


Figure 3.25: $V_{par}-V_{per}$ matrix obtained using the velocities in arms 1 and 2, $^{40}\text{Ar} + ^{208}\text{Pb}$.

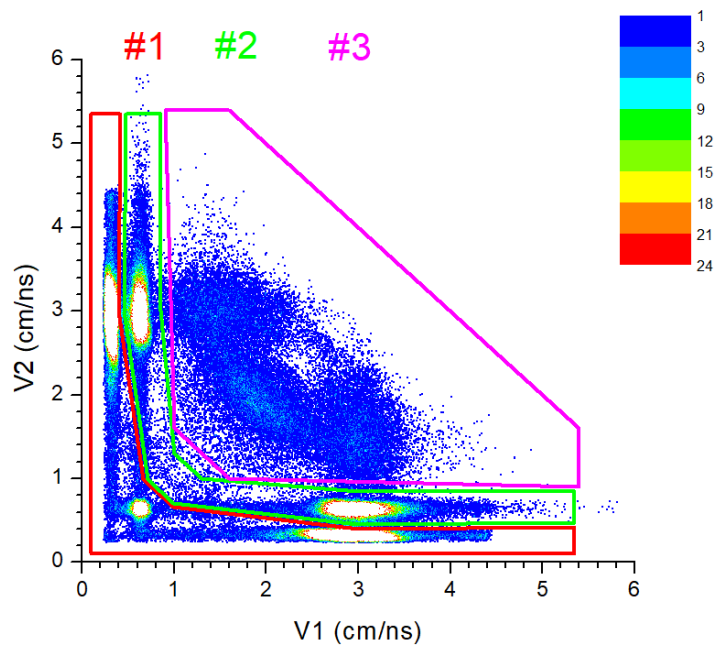


Figure 3.26: Distribution of the velocities measured in arms 1 and 2, $^{40}\text{Ar} + ^{208}\text{Pb}$.

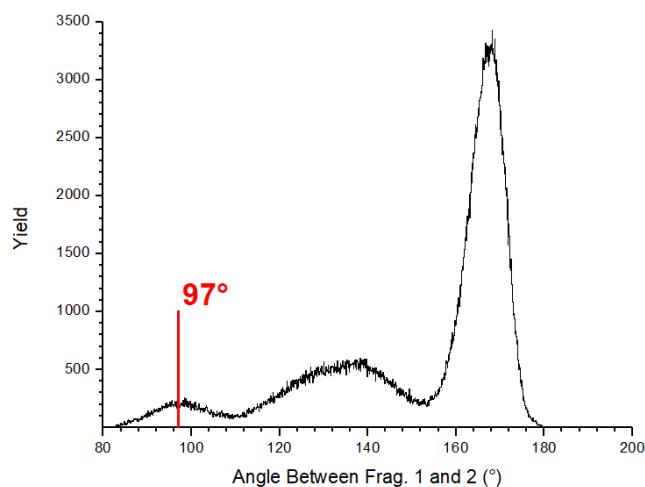


Figure 3.27: Angle between the velocities of fragment 1 and 2 CM reference frame in $^{40}\text{Ar} + ^{208}\text{Pb}$.

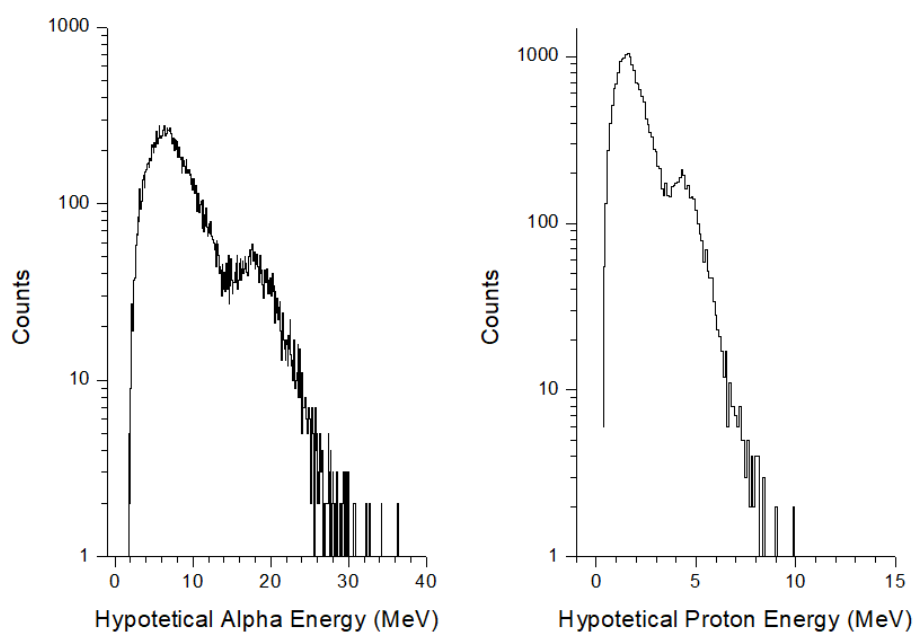


Figure 3.28: Data concerning reaction $^{40}\text{Ar} + ^{208}\text{Pb}$. Left panel: conversion of measured velocity into alpha particle energy. Right panel: conversion of measured velocity into proton energy.

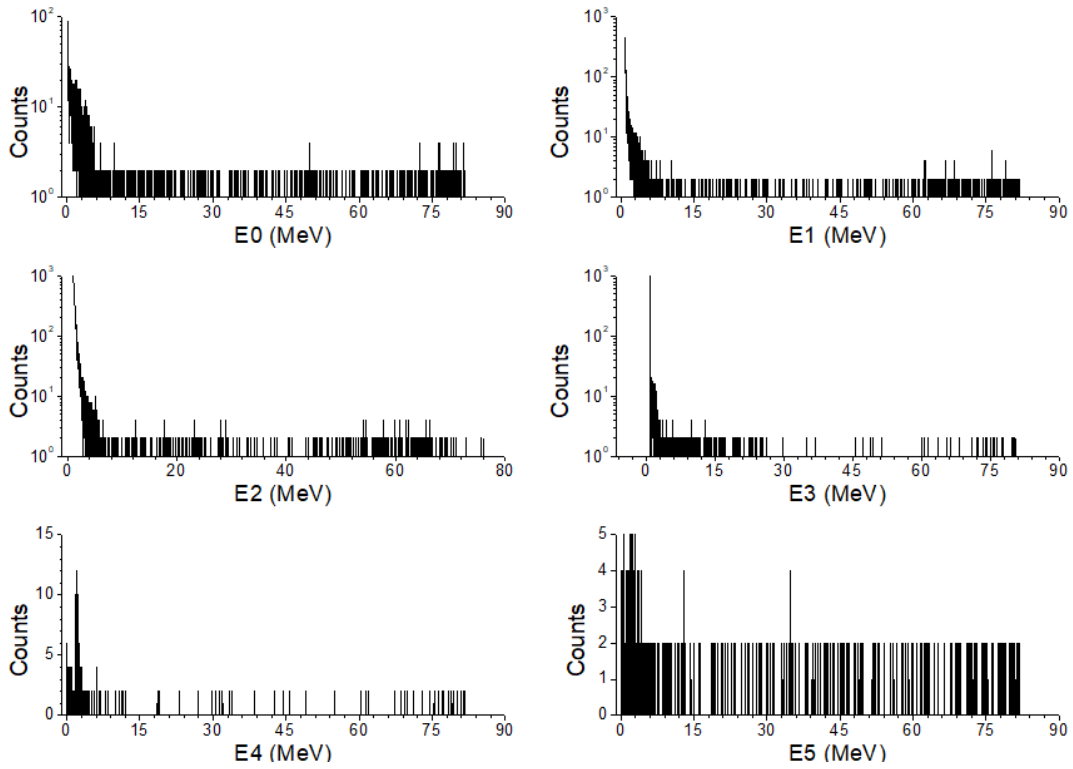


Figure 3.29: Energy spectra measured in $^{40}\text{Ar} + ^{208}\text{Pb}$ by silicon detectors in backward angles (see App. C.2.2).

MeV	u	u	u	u
E_3	M_1	M_2	M_3	M_{tot}
8.62	75	36	88	199
9.37	84	20	96	200
38.81	112	10	105	227

Table 3.3: A selection of results of the mass reconstruction in $^{40}\text{Ar} + ^{208}\text{Pb}$.

Slightly less data, with respect to $^{37}\text{Cl} + ^{208}\text{Pb}$, were collected during $^{40}\text{Ar} + ^{208}\text{Pb}$ reaction. This is the cause of a reduced number of events showing coincidence between the TOF arms and the silicon detectors but, on the other side, the agreement between experimental data and simulations appears to be better than the other three reactions (Fig. 3.31).

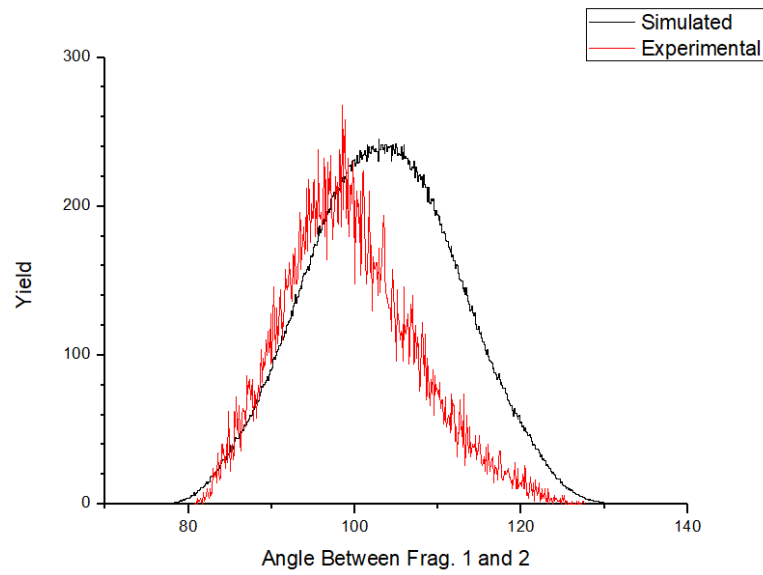


Figure 3.30: Experimental (red) and calculated (black) relative angles distributions in CM reference frame, measured in $^{40}\text{Ar} + ^{208}\text{Pb}$.

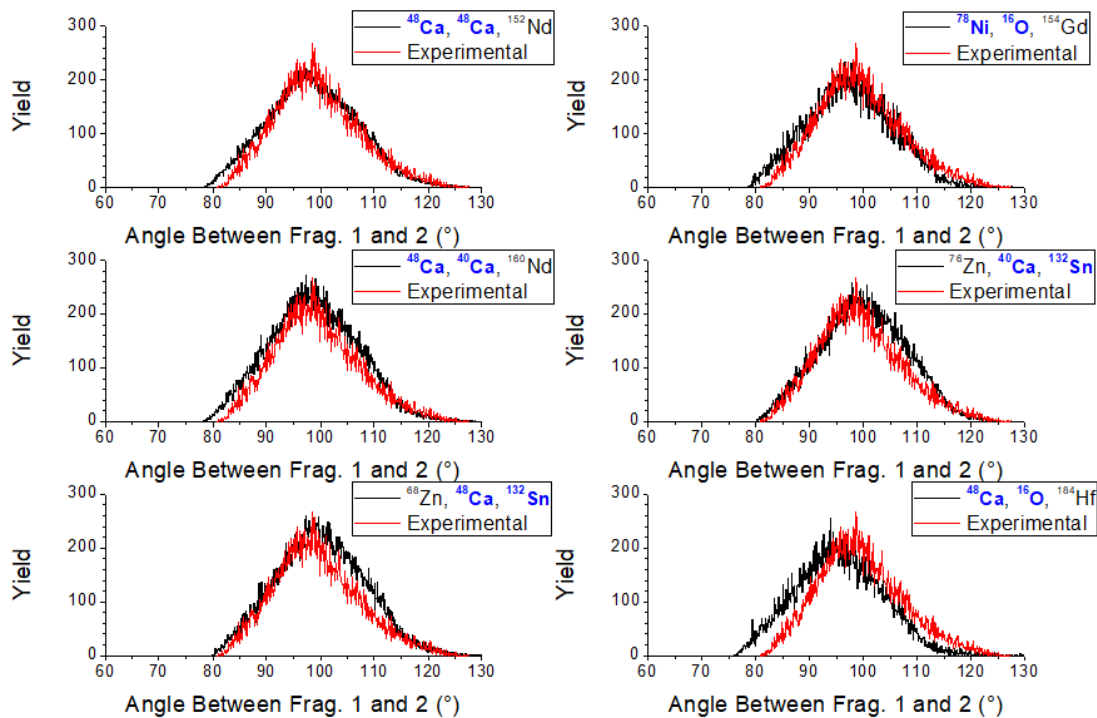


Figure 3.31: Experimental distribution (red) of relative angles, measured in $^{40}\text{Ar} + ^{208}\text{Pb}$ and calculated distribution (black) for indicated triple. Magic nuclei in blue characters. The agreement with simulations appears to be better for this reaction.

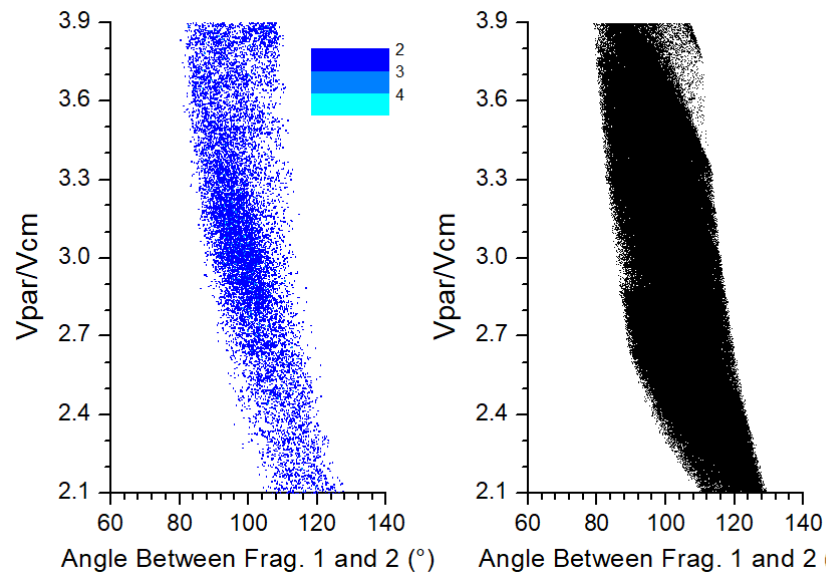


Figure 3.32: Left panel: experimental relative angle - V_{par} matrix measured in $^{40}\text{Ar} + ^{208}\text{Pb}$. Right panel: calculated one (with no intensity).

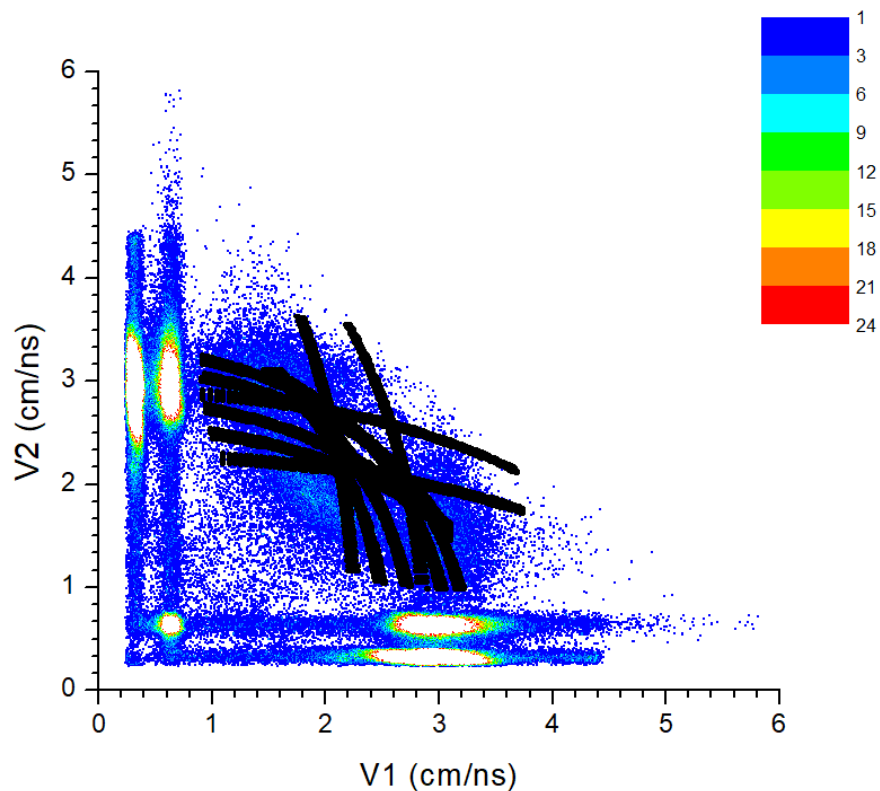


Figure 3.33: Distribution of the velocities measured in CORSET arms 1 and 2, in $^{40}\text{Ar} + ^{208}\text{Pb}$. The black curves are calculated velocities, well overlapping the experimental data.

The following figures refer to results of $^{37}\text{Cl} + ^{205}\text{Tl}$ data analysis.

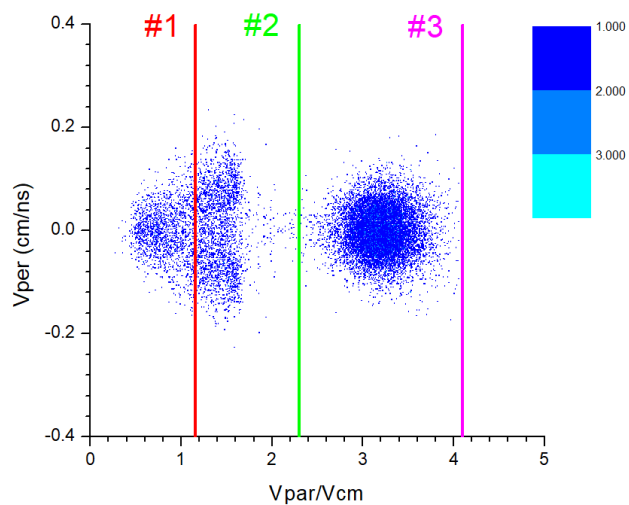


Figure 3.34: $V_{\text{par}}-V_{\text{per}}$ matrix obtained using the velocities in arms 1 and 2, $^{37}\text{Cl} + ^{205}\text{Tl}$.

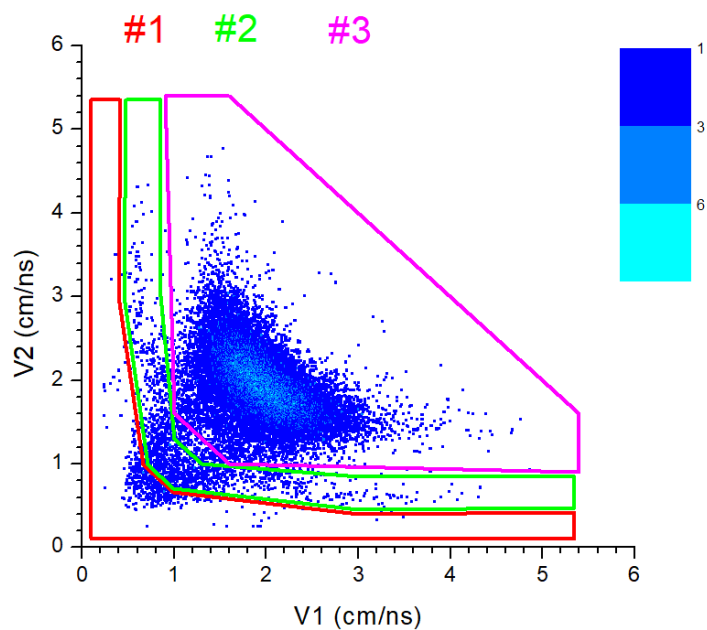


Figure 3.35: Distribution of the velocities in arms 1 and 2, $^{37}\text{Cl} + ^{205}\text{Tl}$.

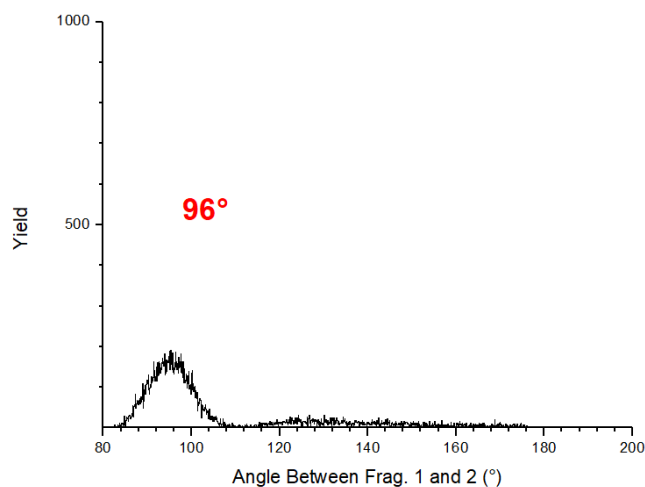


Figure 3.36: Angle between the velocities of fragment 1 and 2 CM reference frame in $^{37}\text{Cl} + ^{205}\text{Tl}$.

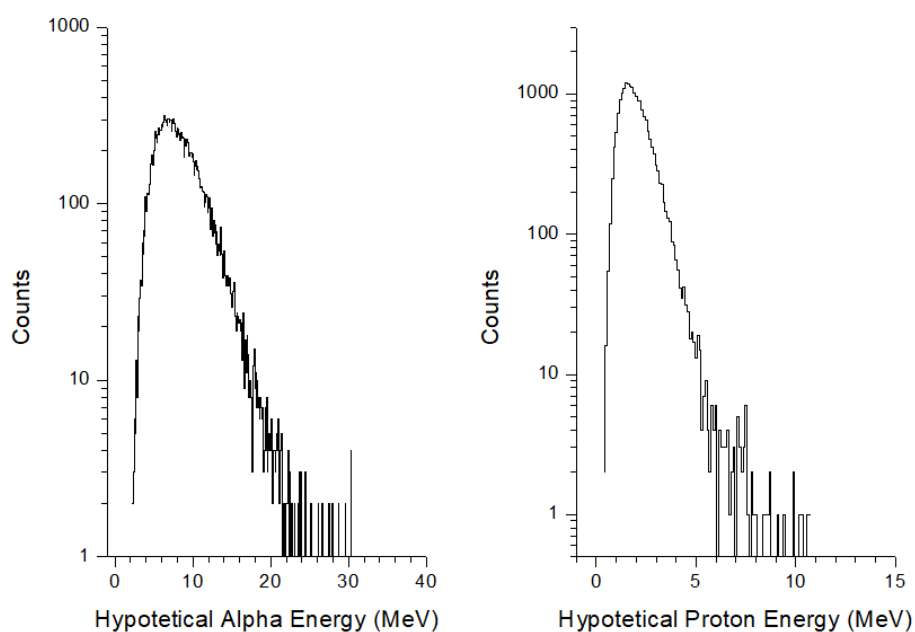


Figure 3.37: Data concerning reaction $^{37}\text{Cl} + ^{205}\text{Tl}$. Left panel: conversion of measured velocity into alpha particle energy. Right panel: conversion of measured velocity into proton energy.

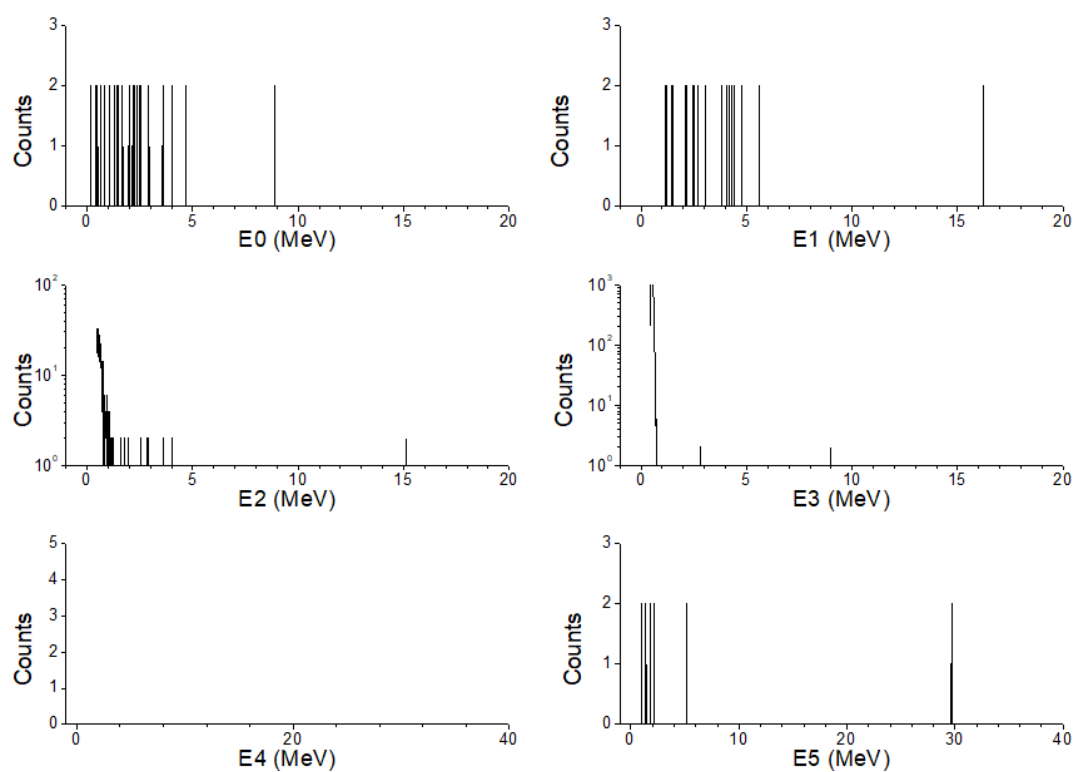


Figure 3.38: Energy spectra measured in $^{37}\text{Cl} + ^{205}\text{Tl}$ by silicon detectors in backward angles (see App. C.2.2).

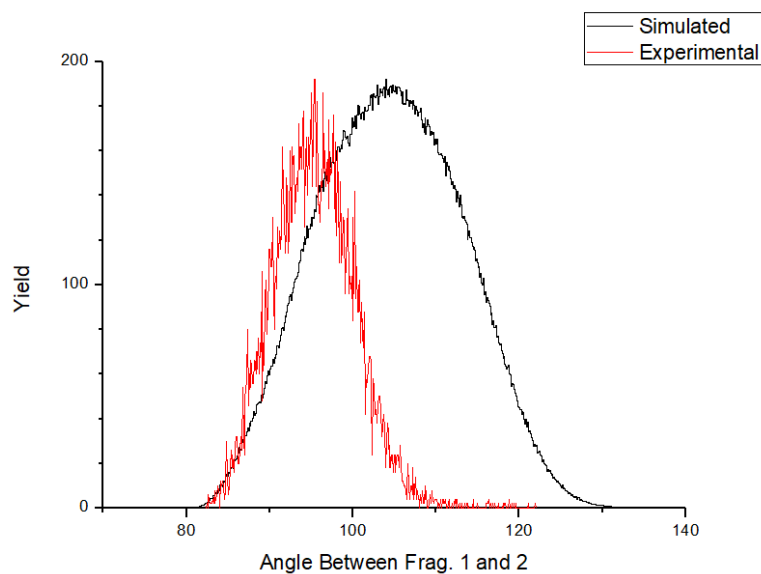


Figure 3.39: Experimental (red) and calculated (black) relative angles distributions in CM reference frame, measured in $^{37}\text{Cl} + ^{205}\text{Tl}$.

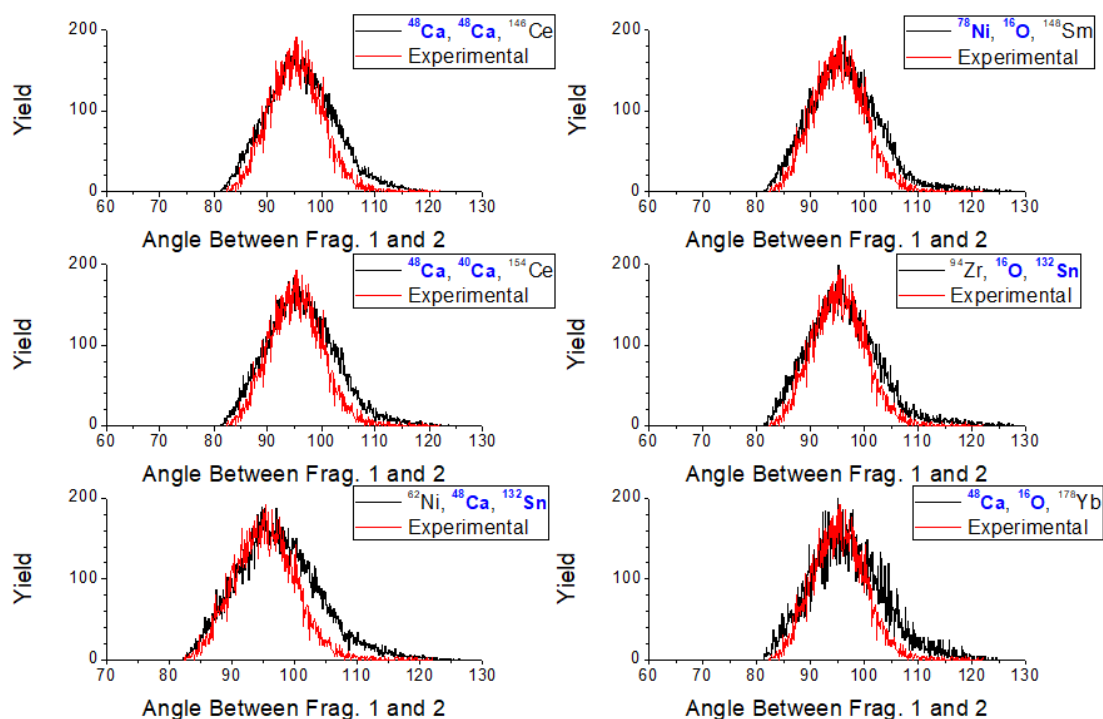


Figure 3.40: Experimental distribution (red) of relative angles, measured in $^{37}\text{Cl} + ^{205}\text{Tl}$ and calculated distribution (black) for indicated triple. Magic nuclei in blue characters.

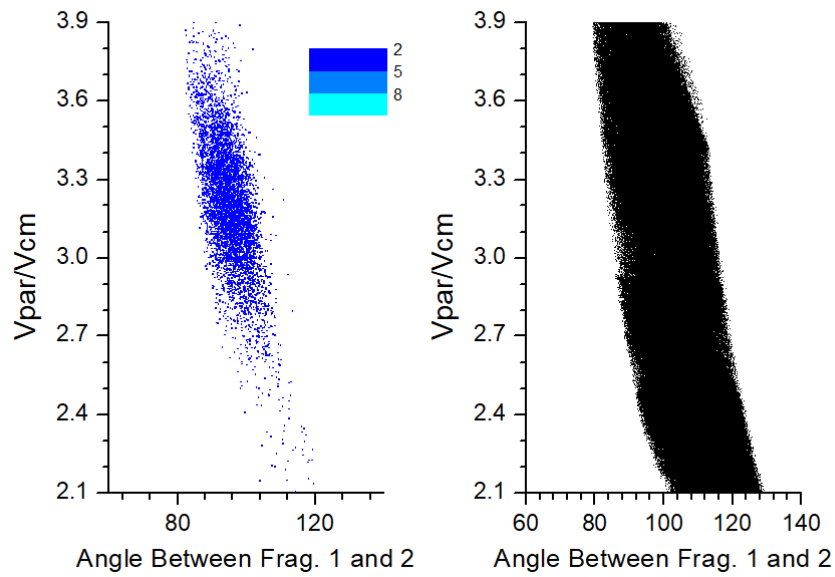


Figure 3.41: Left panel: experimental relative angle - V_{par} matrix measured in ^{37}Cl + ^{205}Tl . Right panel: calculated one (with no intensity).

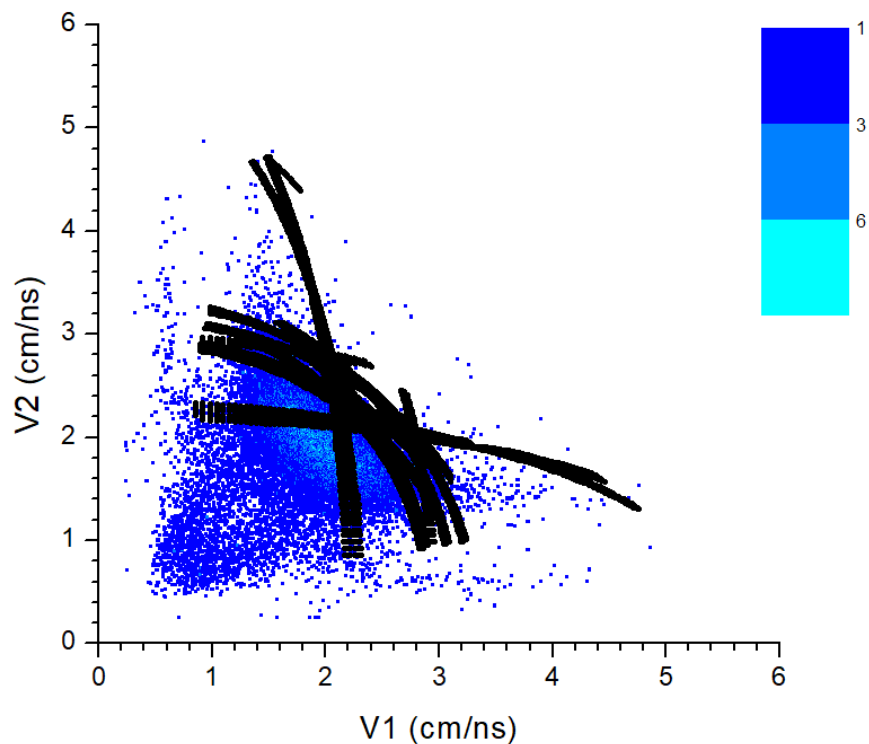


Figure 3.42: Distribution of the velocities measured in CORSET arms 1 and 2, in ^{37}Cl + ^{205}Tl . The black curves are calculated velocities, well overlapping the experimental data.

The following figures refer to results of $^{40}\text{Ar} + ^{205}\text{Tl}$ data analysis.

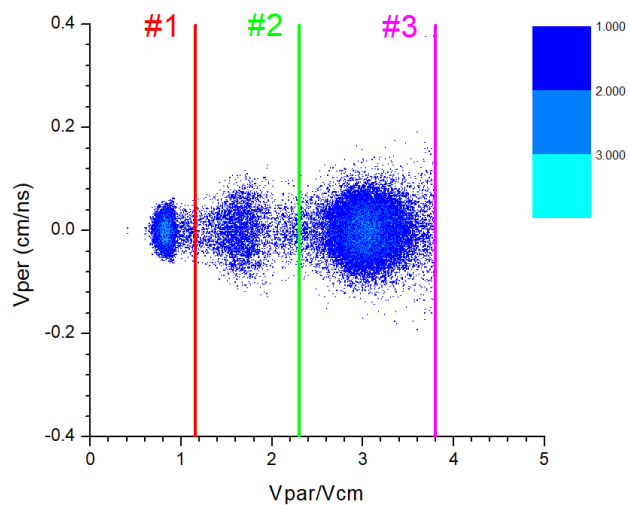


Figure 3.43: $V_{par}-V_{per}$ matrix obtained using the velocities in arms 1 and 2, $^{40}\text{Ar} + ^{205}\text{Tl}$.

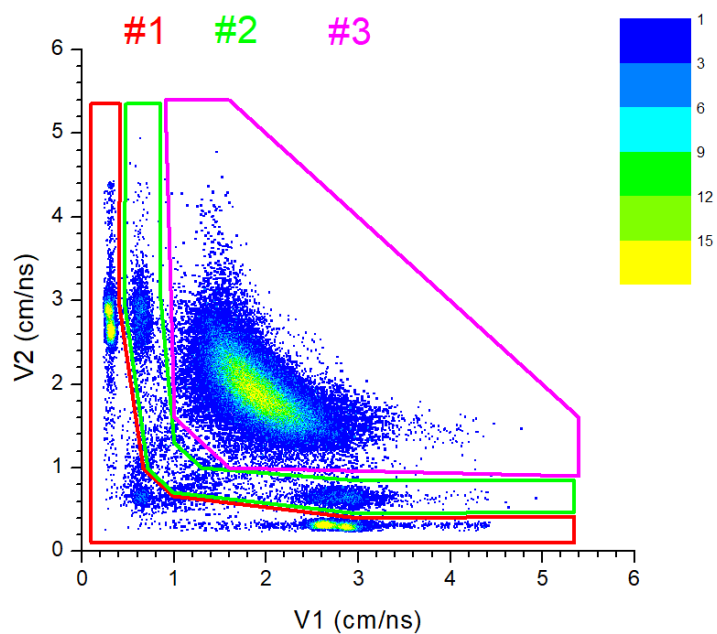


Figure 3.44: Distribution of the velocities in arms 1 and 2, $^{40}\text{Ar} + ^{205}\text{Tl}$.

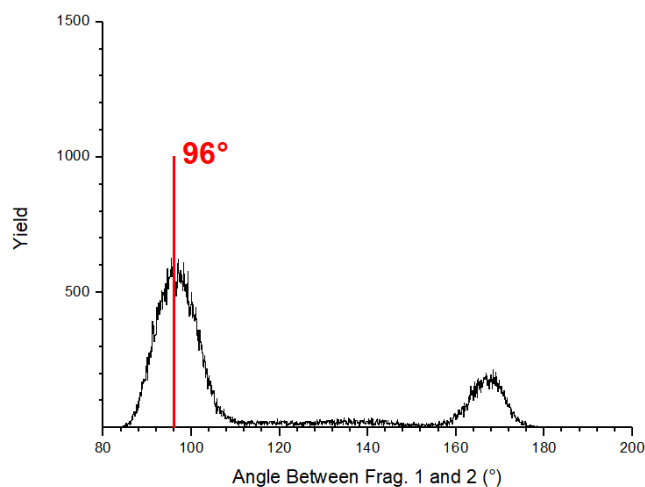


Figure 3.45: Angle between the velocities of fragment 1 and 2 CM reference frame in $^{40}\text{Ar} + ^{205}\text{Tl}$.

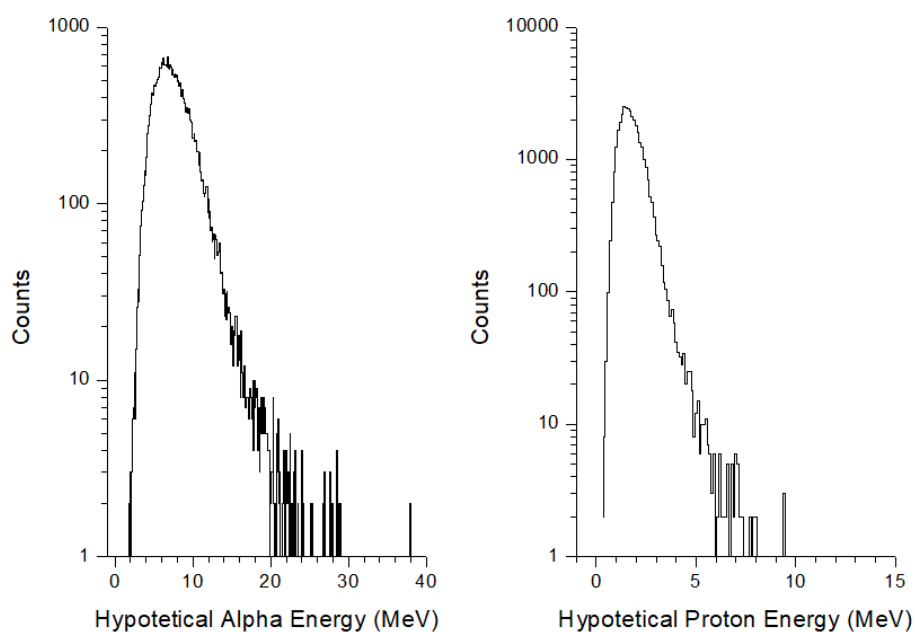


Figure 3.46: Data concerning reaction $^{40}\text{Ar} + ^{205}\text{Tl}$. Left panel: conversion of measured velocity into alpha particle energy. Right panel: conversion of measured velocity into proton energy.

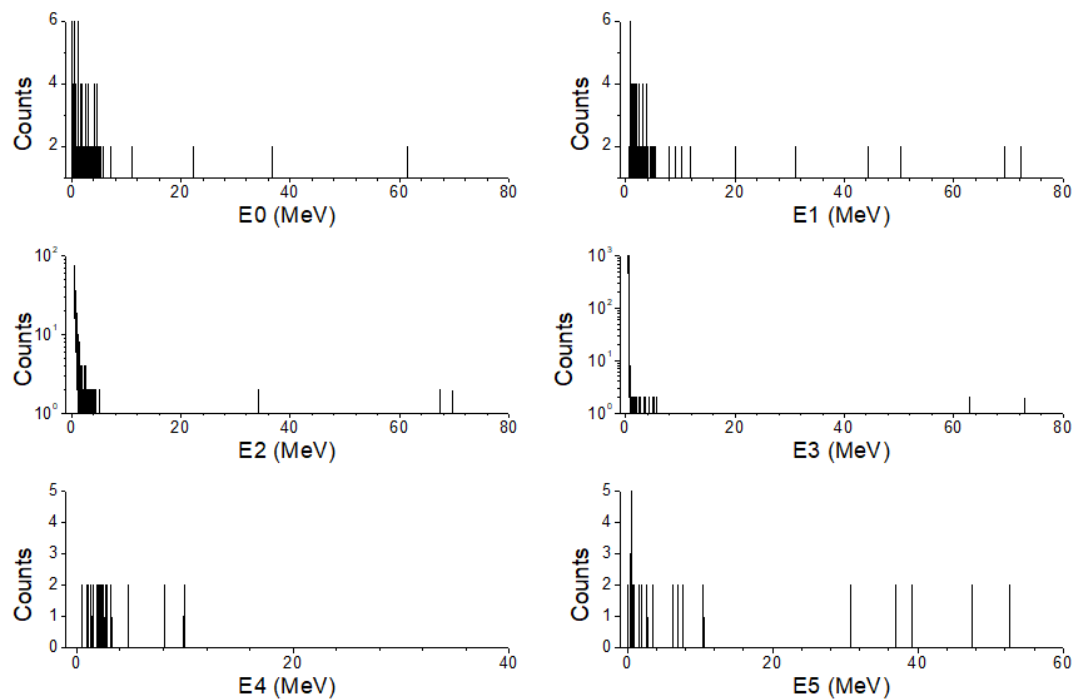


Figure 3.47: Energy spectra measured in $^{40}\text{Ar} + ^{205}\text{Tl}$ by silicon detectors in backward angles (see App. C.2.2).

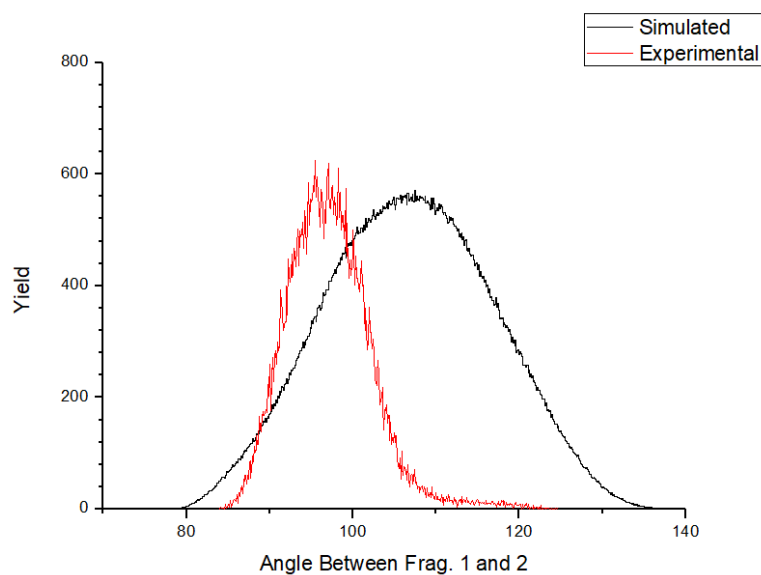


Figure 3.48: Experimental (red) and calculated (black) relative angles distributions in CM reference frame, measured in $^{40}\text{Ar} + ^{205}\text{Tl}$.

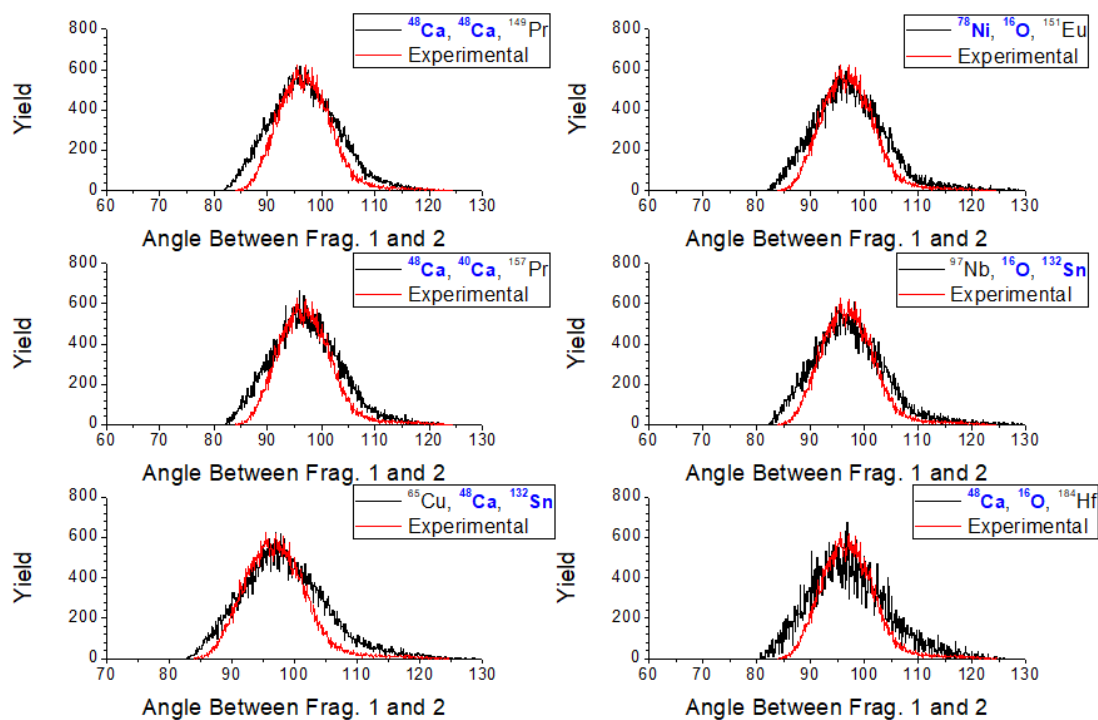


Figure 3.49: Experimental distribution (red) of relative angles, measured in $^{40}\text{Ar} + ^{205}\text{Tl}$ and calculated distribution (black) for indicated triple. Magic nuclei in blue characters.

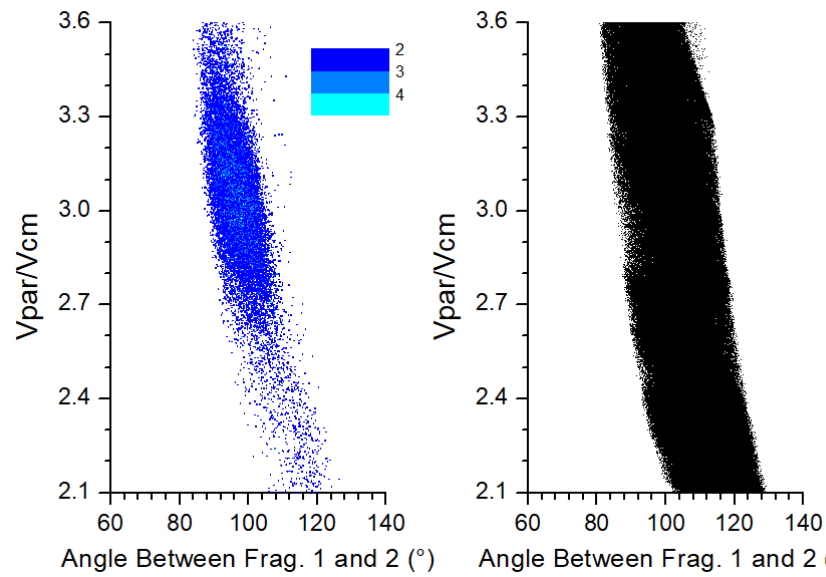


Figure 3.50: Left panel: experimental relative angle - V_{par} matrix measured in $^{40}\text{Ar} + ^{205}\text{Tl}$. Right panel: calculated one (with no intensity).

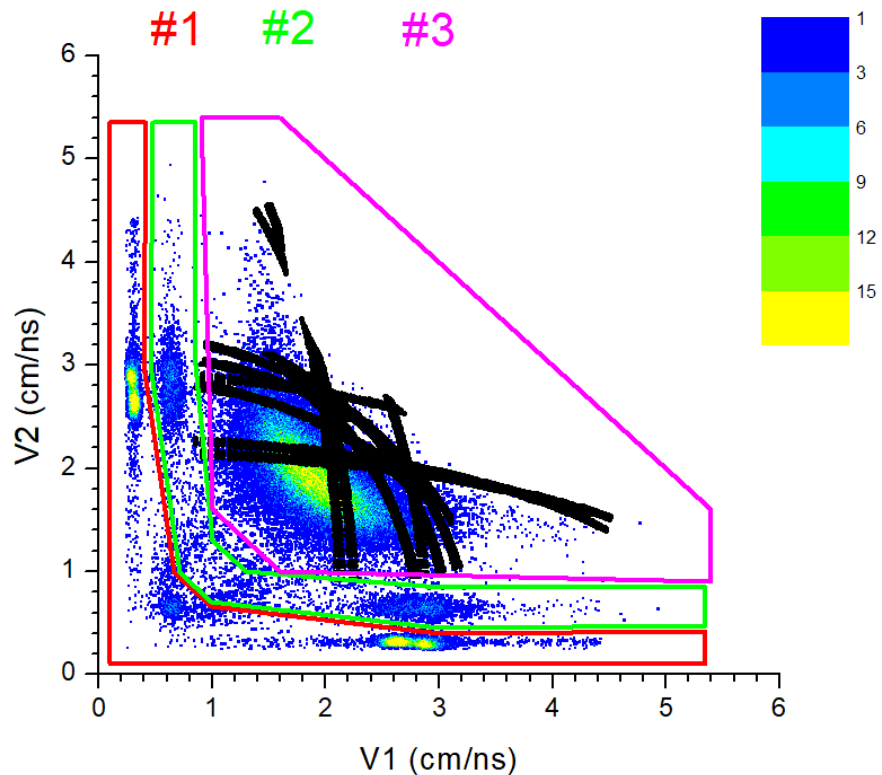


Figure 3.51: Distribution of the velocities measured in CORSET arms 1 and 2, in $^{40}\text{Ar} + ^{205}\text{Tl}$. The black curves are calculated velocities, well overlapping the experimental data.

Chapter 4

Summary and Conclusions

4.1 Xe + Pb LNL Experiment

Fig. 2.11 shows how different values of TKEL are linked to different TLF mass distributions: the more the energy dissipation, the bigger the mass transfer. The masses of interest appear to be produced in very damped events, namely with $\text{TKEL} > 80 \text{ MeV}$.

It is interesting to note the trend shown in Fig. 2.13. The plot is obtained by rebinning of the TKEL distribution, with the adjoint of information about the TLF peak corresponding to each TKEL bin. It is noticeable a change in the slope of the spectrum near the mass value 202 u, meaning that the production of TLF around mass 202 is enhanced by shell effects.

Even if there are evidences from the point of view of a specific mass production, the use of E- Δ E telescope separation is needed for atomic number evaluation. As showed in Chap. 2.3, the IC analysis allows to confirm the production of PLFs of masses around 142 (Fig. 2.17), corresponding to 202u TLFs. This is clearly a confirmation of what found before but the only visible and usable "banana" in the E- Δ E matrix is the one of Fig. 2.15. Thus, because of this low resolution, it is not possible to tell if protons or neutrons are transferred.

These low resolution results still allow to acknowledge the potentiality of the multinucleon transfer channel: the observed persistence of shell effects for

magic numbers $N = 82, 126$ makes this channel interesting for the production of nuclei in the Terra Incognita, in particular in the region of the r-process and possibly near or inside the Island of Stability. The research may continue by exploring reactions involving different choices of colliding nuclei: heavier, in order to reach the region of super heavy nuclei in the Segré Chart or lighter, in order to extend the study to other closed shells. Another interesting possibility would be the exploitation of neutron-rich radioactive ion beams to be provided at SPES facility at LNL.

4.2 NRO127 JYFL Experiment

The use of two supplementary CORSET arms at 65° along with the ones at 40° allowed the observation of pure binary fission decays that may serve as a reference for the type of events. The clear difference between the $V_{par}-V_{per}$ matrices (Fig. 3.12, 3.13, 3.15, 3.14 vs. Fig. 3.16, 3.25, 3.34, 3.43), in each of the four reactions, represents the first hint of the occurrence of non-binary decays, detected by CORSET arm 1 and 2. This hint is confirmed by the further steps of the analysis.

It has been excluded the possibility of confusing these events with proton or alpha evaporation, from both CN and target backing, through considerations about energy distribution of this hypothetical particles (see Fig. 3.19, 3.28, 3.37, 3.46).

Ulterior trust in support of the ternary nature of the events detected in arm 1 and arm 2 is provided by the analysis of other observables such as the relative angle and V_{par} . Fig. 3.18, 3.27, 3.36, 3.45 show the distribution of the relative angle measured in CM reference frame. By application of gates on $V_{par}-V_{per}$, which automatically select regions in V_1-V_2 matrices in Fig. 3.17, 3.26, 3.35, 3.44, it is possible to find that the relative angle distribution is peaked at $\sim 96^\circ$ with

negligible differences in the four reactions. In the case of binary decay, this angle should distribute around 180° , and around 120° in the case of perfectly symmetric tripartition. Such a small angle suggests the occurrence of a tripartition with two fragments sensibly lighter than the third one, with the heaviest emitted backwards.

A comparison with simulations confirms the latter assumption.

A simulation code was used to produce velocities and angles of the three fragments for each possible initial and final configuration involving at least two doubly magic nuclei. The choice of restricting the analysis only to tripartitions involving two doubly magic nuclei is suggested by the analogy in spontaneous binary fission, in which only one fragment is usually doubly magic. Extending this concept to ternary fission, it is reasonable to figure out a decay with two doubly magic nuclei and the third one taking away the remaining mass. If ternary decay is favored by this condition, it should be less likely in cases where the mass of the CN can be split into three magic fragments, e.g. $^{252-258}\text{Cf}$.

It should be noted that only for the system Cl + Tl it is possible, by mass conservation, a tripartition into two doubly magic nuclei plus a single magic one.

In Fig. 3.22, 3.31, 3.40, 3.49 it is clear how the experimental relative angle distribution is more well reproduced by calculations involving two light, doubly magic nuclei having similar masses and flying in CORSET arm 1 and 2. The only exception is represented by the case of ^{132}Sn (doubly magic, flying backward) having as companions a light doubly magic nucleus and a light non-magic nucleus. From this comparison it seems that:

- the experimental distribution matches with the above discussed configurations;
- the experimental distribution may be reproduced by a superposition of all cases, each with a different weight (this is a work in progress).

The comparison between the measured matrix V_1-V_2 and the homologue calculated data in Fig. 3.24, 3.33, 3.42, 3.51 represents another confirmation of how well experimental and calculated data match.

Considering the few events in which the third fragment was detected, it is possible to assert that is mostly the heaviest one to fly in backward direction. However, several technical problems arose concerning the energy measurement of the third fragment, ranging from few MeV to 100 MeV and this, along with a small solid angle coverage, brought to rough mass estimates, reported in Tab. 3.2 and 3.3 (no available data for $^{40}\text{Ar} + ^{205}\text{Tl}$ and $^{37}\text{Cl} + ^{205}\text{Tl}$ reactions). The best solution to overcome these difficulties would be the implementation of two (or more) ulterior CORSET arms, to be placed at backward angles in substitution of the silicon detectors. In this way, it would be possible not only to exploit the high time resolution of MCP based detectors but also the possibility of measuring three velocities instead of two plus one energy. Another path to follow could be the study of a possible tripartition of $^{252-258}\text{Cf}$, in order to prove the hypothesis according to which a final configuration of two doubly magic nuclei plus a non magic one is more favorable than three doubly magic fragments.

Appendix A

Data Analysis

This Appendix has the purpose of showing, in a summary, all the relevant analysis processes studied or developed by the author. Further, in Appendix B are also showed some related original code, developed during the three years of PhD school.

All geometrical calculations, such as evaluation of plane or line equations, intersections etc. or other, less relevant, details will be omitted in order to clearly show the analysis method in its general form.

A.1 Preliminary Calculations: Angular Correlation

The Viola Systematics [31, 32] is a powerful and solid instrument in nuclear fission analysis and simulations. Viola et al. found an empirical law which shows how the Total Kinetic Energy of fission fragments depend linearly on the Coulomb parameter $Z_{CN}^2/A_{CN}^{1/3}$, where Z_{CN} and A_{CN} refer to the atomic and mass number of the fissioning nucleus, both in case of induced fission (thus a compound nucleus is formed) and spontaneous fission. $A_{CN}^{1/3}$ is proportional to the nuclear radius. The meaning of the systematics is that the primary responsible for the TKE of fission fragments is their electrostatic repulsion.

$$TKE_s = 0.1189 \frac{Z_{CN}^2}{A_{cn}^{1/3}} + 7.3MeV \quad (\text{A.1})$$

The equation A.1 stands for the case of strictly symmetrical separation while the following can be used if the system separates in fragments having masses A and $A_{CN} - A$ respectively:

$$TKE = TKE_s A_{cn}^{-5/3} 2^{8/3} \frac{A(A_{CN} - A)}{A^{1/3} + (A_{cn} - A)^{1/3}}. \quad (\text{A.2})$$

Knowing the available energy and applying the momentum conservation law, it is possible to simulate the 2-body kinematics in the Centre of Mass reference frame: the two fragments are emitted back to back and no direction is preferred. By adding the Centre of Mass motion (no motion in spontaneous fission) to the relative one, for each exit angle with respect to the beam in the Centre of Mass reference frame, it is possible to evaluate the angle in the Laboratory frame and thus build a correlation curve as the one in Fig A.1.

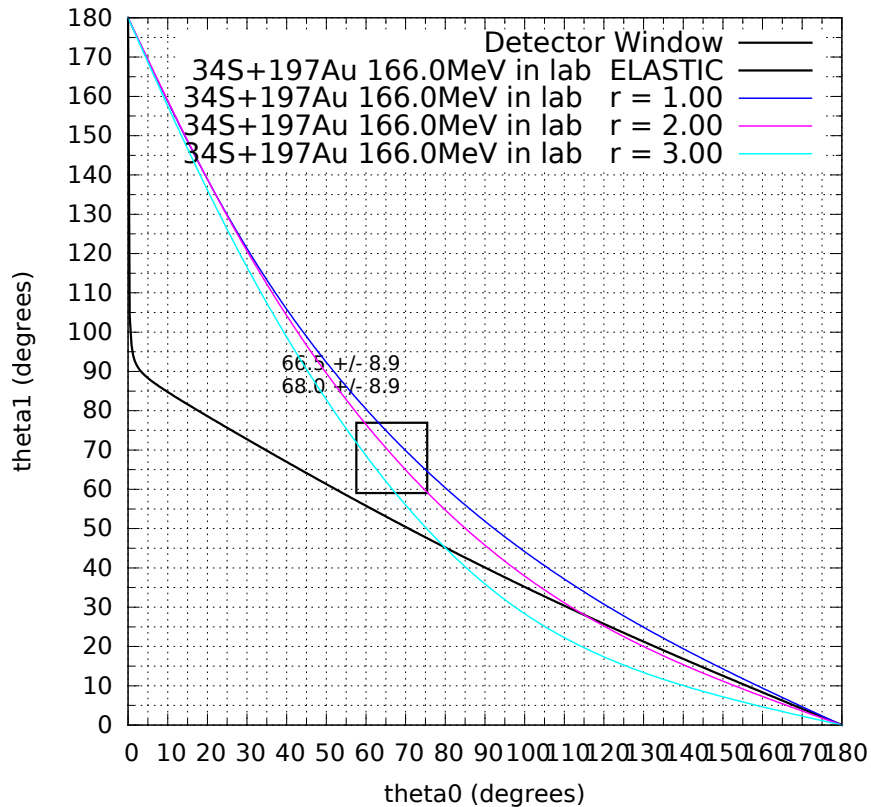


Figure A.1: Example of the angular correlation curve produced by the code in App. B, applying Viola systematics.

If the total mass is known and the mass ratio of the fragments is provided, the fragment masses are unambiguously found by:

$$r = m_0/m_1 \quad (\text{A.3})$$

$$m_1 = A_{cn}/(r + 1) \quad (\text{A.4})$$

$$m_0 = A_{cn} - m_1 \quad (\text{A.5})$$

Then eq. A.5 can be used to find the TKE, which will be redistributed accordingly to the mass ratio. Thus, the velocity of the fragments in the CM frame of reference are:

$$V_{cm}^0 = \sqrt{TKE/0.5183/m_0/(r + 1)} \quad (\text{A.6})$$

$$V_{cm}^1 = V_{cm}^0 r \quad (\text{A.7})$$

If the bombarding energy (equal to zero in the case of spontaneous fission) is known, such is also the velocity of the centre of mass. In the centre of mass frame, the exit angles of the fragments with respect to an arbitrary axis (for example the beam) are always supplementary because of momentum conservation:

$$\theta_{cm}^1 = 180 - \theta_{cm}^0; \quad (\text{A.8})$$

Fixing one immediately gives the other and the corresponding angle in laboratory frame depends only on the centre of mass motion:

$$\theta_{lab}^i = \arctan\left(\frac{V_{cm}^i \sin(\theta_{cm}^i)}{V_{CM} + V_{cm}^i \cos(\theta_{cm}^i)}\right); \quad (\text{A.9})$$

In this way, it is possible to build a curve of the exit angle in lab frame of the fragments in coincidence. This curve is of paramount usefulness in the preliminary phases of an experiment, allowing to predict where to put the detectors,

in an experimental environment, in order to detect fission fragments in coincidence. This also applies to elastic scattering.

In order to perform such prediction, a code in C language was written by the author. Fig. shows an example output of the program. In appendix B more details are shown about the tool developed by the author.

A.2 Detectors Calibration

This section will shortly explain the usual calibration techniques.

A.2.1 Time Calibration

The time calibration consists in the calibration of both TAC (Time to Amplitude Converter) and TDC (Time to Digital Converter) electronic modules. A Time Calibrator module (aka "Pulser") is plugged into the TACs and TDCs, providing a series of equally distant (in time) peaks used for the evaluation of the slope of the linear calibration. Since the position information is extracted from time measurements, the TDC channels X, Y, Start and Stop are separately calibrated and their slope is used to convert position raw data in time. The further step is to provide the differences X-Stop and Y-Stop, still measured as time, which will be calibrated as shown in A.2.2. Times of Flight (TOFs) may be measured by the difference Stop-Start (TDC channels) or by means of a TAC, which output is plugged into an ADC (most suitable choice if an ADC offering more bits than the TDC is available). In both cases, the difference Sp-St from TDC and the output of TAC+ADC chain provide a spectrum in which a known peak may be

used to find the intercept of the linear calibration:

$$\text{intercept}(ns) = \text{KNOWNTIME}(ns) - \text{centroid}(\text{arb.un.}) \times \text{slope}(ns/\text{arb.un.}) \quad (\text{A.10})$$

Usually the known peak is the one related to elastic scattering of the projectile on target and specific calibration runs are conducted using the detectors in “single” coincidence logic. Another, less preferable or backup, option is to use, whenever possible, elastic scattering peaks of both projectile and target to perform a 2-point linear calibration.

A.2.2 Position Calibration

The position-sensitive detectors are calibrated in order to extract the fragments position from raw data. This calibration is based on the well-known position (along X and Y axis) of at least two points on the detector surface: in many cases a wire mask with some known positions is put in front of the sensitive area (e.g. a metal cross in front of PRISMA entrance MCP or a plastic reticule in front of CORSET Stop) while in absence of this tool the edges (size of the detector) are used. Since position information is obtained in a delay lines system of the stop MCP, this data are essentially time measurement: a preliminary time calibration with a pulser [A.10](#) is needed also for X and Y data. Then, another linear regression produces the calibration parameters that convert the time measurements in mm. In many cases the middle step of converting raw data in time can be skipped if the slopes obtained during the TDC calibration appear to be very similar to each other.

A.2.3 PRISMA Ionization Chamber Calibration

The Ionization Chamber in PRISMA setup is used for Z identification of PLFs. The latter do not need an absolute energy calibration since it is based on qualitative analysis of E - βE matrix, the recognition of the so-called "bananas": the most populated "banana" refers to elastic and quasi-elastic scattering then, moving up or down in the matrix, the other "bananas" refer to higher or lower Z values respectively; two successive "bananas" differ for one charge unit. For this purpose, since the IC sensitive component is the segmented anode, the calibration just serves as alignment of data coming from each section. The resulting E - βE matrix remains in arbitrary units but, nonetheless, allows the qualitative analysis.

A.3 Analysis

A.3.1 PRISMA Ionization Chamber

After the alignment calibration it is possible, through several logics, to treat the IC as a set of ten E -DE telescopes. Since the IC consists of a 10×4 array of sensitive pads, the easiest possibilities are to take the first section of each telescope or the sum of the first two as a βE stage and, of course, the sum of the four as E . In this way, the E - βE matrix can be provided and qualitatively analysed in order to find "bananas" and their link to the mass distribution.

A.3.2 TOF-TOF Analysis

This kind of analysis is performed if the experimental setup consists of two (or more) CORSET-like arm having each a Start and a Stop detector thus the Time of Flight is defined by the difference in time between Stop and Start signals. This kind of analysis was performed for NRO127 Experiment (3).

Laboratory Frame of reference

In order to perform the geometrical calculations the lead to the velocity evaluation, it is necessary to choose and fix the laboratory frame of reference. The frame origin is arbitrarily fixed in the centre of the target, the beam line corresponds to the Z axis, X and Y axis are respectively vertical and horizontal (with respect to the lab) axis. The needed geometrical quantities are:

- Angular position of the arms;
- Tilt angles of the detectors (if different from zero);
- Distances between Start Detectors and Target;
- Distance between Stop Detector and Start Detector of each arm.

From those quantities above it is possible to evaluate all useful information, such as the position of the centre of each target, the equation of the plane representing the start detectors, the absolute position of the particle impinging the stop detectors and the equation of their trajectories as will be shown in detail further. An example is given in the schematic view of the detectors (projection onto X-Z axis) shown in Fig. A.2, representing the layouts of CORSET-like setups in different experiment.

Flight Paths

In order to evaluate the velocity vector (thus the trajectory) of the fragments in the laboratory frame, it is necessary the evaluation of times of flight and flight paths. Since the geometrical concept of the arms is identical, the arm index "i" in the following formulas means that the equations can be applied to each arm separately. The position (H_i), in laboratory frame, of the fragment hitting a STOP detector are given by the following equations, where X_{stop} and Y_{stop} are the coordinates of the fragment onto the detecting surface:

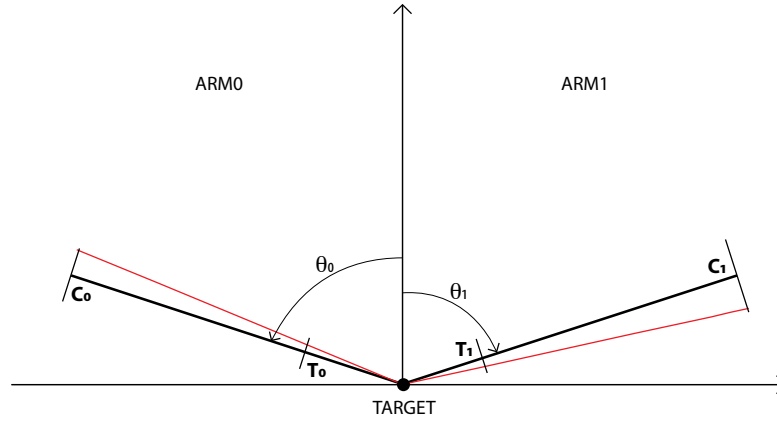


Figure A.2: Schematic view of a CORSET or CORSET-like setup. The black, bold lines represent the central axis of each arm, with the detectors placed perpendicularly to them. The red lines are an example of fragment trajectories originating from the target and hitting the Stop after passing through Start. C_i represents the center of the stop detector, while T_i the center of the start detector.

$$H_i(x) = C_i(x) + Y stop_i \quad (\text{A.11})$$

$$H_i(y) = C_i(y) + X stop_i \cos \theta_i \quad (\text{A.12})$$

$$H_i(z) = C_i(z) + X stop_i \sin \theta_i \quad (\text{A.13})$$

$$\theta_0 < 0 < \theta_1 \quad (\text{A.14})$$

which are transformation from coordinates on the detector surface to 3D Cartesian coordinates in laboratory reference frame, C_i represents the center of the stop detector. These transformations plus the knowledge of the geometry allow to evaluate the (linear) trajectory for the fragment from target to STOP detector, being assumed that the fragment velocity vector direction is not sensitively affected while emerging from the target, after the reaction took place, and passing through the start detector: because of the small thickness of target and detector foils it is possible to neglect the straggling. The flight path of the fragment flying in the arm is then the distance between the intersection of the

trajectory with the START detector (h_i) and the hit point on stop detector:

$$L_i = \sqrt{(H_i(x) - h_i(x))^2 + (H_i(y) - h_i(y))^2 + (H_i(z) - h_i(z))^2} \quad (\text{A.15})$$

the polar and azimuthal angles defining the direction are:

$$\vartheta_i = \arccos \frac{H_i(z)}{\sqrt{H_i^2(x) + H_i^2(y) + H_i^2(z)}} \quad (\text{A.16})$$

$$\varphi_i = \arctan \frac{H_i(y)}{H_i(x)} \quad (\text{A.17})$$

Velocity Calculation

The velocity modulus of the fragment in each arm is immediately obtained, being tof_i the actual time of flight between start and stop detector in the i -th arm:

$$V_i = \frac{L_i}{tof_i} \quad (\text{A.18})$$

A.3.3 TOF-DTSP Analysis

This kind of analysis is performed if the experimental setup consists of one CORSET-like arm (namely TOF arm) and a DTSP (Delta Stop) arm, having the latter only a Stop detector. The Time of Flight in the DTSP arm is evaluate exploiting the TOF in TOF arm and difference in time between the stop signals, hence the name DTSP.

Laboratory Frame of reference

In order to perform the geometrical calculations the lead to the velocity evaluation, it is necessary to choose and fix the laboratory frame of reference. The

frame origin is arbitrarily fixed in the centre of the target, the beam line corresponds to the Z axis, X and Y axis are respectively vertical and horizontal (with respect to the lab) axis. The needed geometrical quantities are:

- Angular position of the arms;
- Tilt angles of the detectors (if different from zero);
- Distances between Start Detector and Target, between Stop and Start Detector (TOF arm);
- Distance between Stop Detector and Target (DTSP arm).

An example is given in the schematic view of the detectors (projection onto X-Z axis) shown in Fig. 2.3 and 2.3: the PRISMA and Bragg arms are located respectively at 45° and 52° with respect to the beam (Z) axis, the PRISMA MCP is tilted by 45° so it is parallel to the beam axis and the TOF arm PPAC is perpendicular to the line at 52° with respect to the beam axis (Fig A.3).

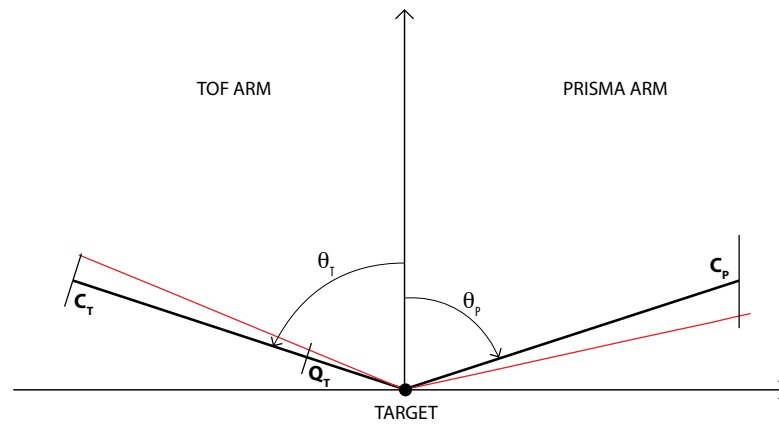


Figure A.3: Schematic view of PRISMA setup, based on one TOF arm and one (PRISMA) DTSP arm. The black, bold lines represent the central axis of each arm, TOF arm Stop is perpendicular to the axis while PRISMA MCP is tilted and parallel to the beam. The red lines are an example of fragment trajectories originating from the target and hitting the Stop after passing through Start. C_i represents the center of the stop detector, while T_i the center of the start detector.

Flight Paths

In order to evaluate the velocity vector (thus the trajectory) of the fragments in the laboratory frame, it is necessary the evaluation of times of flight and flight paths. The position, in laboratory frame, of the fragment hitting the Stop detector of TOF arm are given by the equations A.11, A.12, A.13 and the flight paths and angles are the same as stressed in A.15, A.16, A.17. The DTSP Arm provides only Stop information so, reasonably, the flight path is the line conjoining the hit point on STOP surface (H_{DTSP} , which coordinate are obtained again by transformations refeq:hittof1, A.12, A.13) and the origin of the frame of reference, assuming that the fragment velocity vector direction is not sensitively affected while emerging from the target after the reaction took place:

$$L_{DTSP} = \sqrt{H_{DTSP}^2(x) + H_{DTSP}^2(y) + H_{DTSP}^2(z)} \quad (\text{A.19})$$

$$\vartheta_{DTSP} = \arccos \frac{H_{DTSP}(z)}{L_{DTSP}} \quad (\text{A.20})$$

$$\varphi_{DTSP} = \arctan \frac{H_{DTSP}(y)}{H_{DTSP}(x)} \quad (\text{A.21})$$

Velocity Calculation

The velocity modulus of the fragment in TOF arm is immediately obtained, having the actual time of flight between start and stop detector in this arm: see eq. A.18. The time of flight of the fragment in DTSP arm is calculated event by event by means of the following formula:

$$tof_{DTSP} = tof_{TOF} + \frac{\sqrt{h_{TOF}^2(x) + h_{TOF}^2(y) + h_{TOF}^2(z)}}{V_{TOF}} - DTSP \quad (\text{A.22})$$

Where $\frac{\sqrt{h_{TOF}^2(x) + h_{TOF}^2(y) + h_{TOF}^2(z)}}{V_{TOF}}$ is the time of flight of the fragment flying from the target to the START in TOF arm and DTSP is the time between the two

stop signals. Once tof_{DTSP} is known, the velocity modulus of the fragment in DTSP arm is simply given by:

$$V_{DTSP} = \frac{L_{DTSP}}{tof_{DTSP}} \quad (\text{A.23})$$

A.3.4 Quantities in Centre of Mass Reference Frame

Since the bombarding energy, thus the velocity of centre of mass, is known as a reaction parameter, it is possible to evaluate, without ambiguity, the velocity vectors (modulus and direction) in the CM frame of reference.

The fragments have velocity in the CM frame given by:

$$\vec{V}_i^{CM} = \vec{V}_i^{lab} + \vec{V}_{CM} \quad (\text{A.24})$$

where the velocity direction of the centre of mass is the beam direction and the modulus is:

$$V_{CM} = \frac{M_{proj} V_{proj}}{M_{proj} + M_{tar}} \quad (\text{A.25})$$

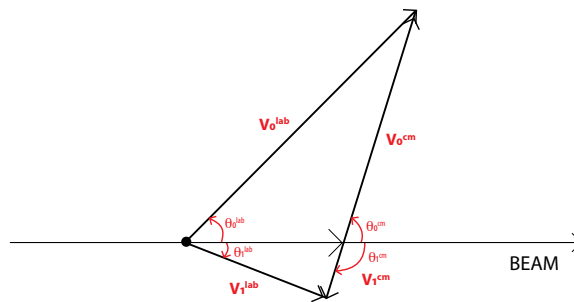


Figure A.4: Triangle of velocity vectors of a binary reaction. Using simple trigonometric formulas it is possible to transfer velocities and angles from laboratory reference frame to CM frame.

Fig. A.4 shows the triangle of velocity vectors in a binary FMT reaction: angles and velocities in the CM frame are obtained by simple trigonometric

considerations. The angle defining the fragment velocity direction in the CM frame is given by:

$$\tan \vartheta_i(CM) = \frac{V_i(lab) \sin \vartheta_i(lab)}{V_i(lab) \cos \vartheta_i(lab) - V_{CM_i}} \quad (A.26)$$

while its modulus is:

$$V_i(CM) = \frac{V_i(lab) \sin \vartheta_i(lab)}{\sin \vartheta_i(CM)} \quad (A.27)$$

The folding angle Ψ is equal to the sum of the angles corresponding to the two fragments and is equal to 180° in the case of FMT binary events, thus being another probe in the search of the latter.

A.3.5 Binary Reaction Analysis

Vpar-Vper Test for Binary Decay

Once both velocity vectors are fully evaluated, a useful 2D distribution can be built; namely the V_{\parallel} vs. V_{\perp} matrix, being respectively the projections of the velocity vectors on and orthogonally to the reaction plane (the plane orthogonal to the angular momentum axis). These projections are the results of the following formulas:

$$V_{\parallel} = \frac{u_0 w_1 + u_1 w_0}{u_0 + u_1} \quad (A.28)$$

$$V_{\perp} = \frac{u_0 u_1 \sin(\varphi_0 - \varphi_1)}{\sqrt{u_0^2 + u_1^2 - 2u_0 u_1 \cos(\varphi_0 - \varphi_1)}} \quad (A.29)$$

Being

$$u_i = V_i \sin \vartheta_i \quad (\text{A.30})$$

$$w_i = V_i \cos \vartheta_i \quad (\text{A.31})$$

As stressed in Chapters 2 and 3, for full momentum transfer (FMT) binary reactions, $V_{||}$ is equal to V_{cm} while V_{\perp} , should be around zero. In the case of sequential fission of a fragment (usually the target-like one), $V_{||}$ deviates from V_{cm} and only two cases can occur:

- (a) if the detected sequential fission fragment is the one flying *forward* in the frame of reference of the fissioning fragment, $V_{||}$ is *greater* than V_{cm} ;
- (b) if the detected sequential fission fragment is the one flying *backward* in the frame of reference of the TLF, $V_{||}$ is *lower* than V_{cm} .

The three possibilities are schematically pictured in the kinematic diagram in Fig. 2.5. The evaluation of energy and masses of the fragments is based on the assumption that the analyzed reaction is a *binary* one. The $V_{||}$ vs. V_{\perp} matrix is therefore, clearly, a powerful tool to filter the events and discard the sequential fission cases.

Angular Correlations

The relative velocity of the fragments and the angle between their velocity vectors are useful quantities, mostly for correlation test. The angle between fragment trajectories is calculated using the scalar product:

$$\vec{V}_0 \cdot \vec{V}_1 = V_0 V_1 \cos \vartheta_{rel} = V_0(x)V_1(x) + V_0(y)V_1(y) + V_0(z)V_1(z) \quad (\text{A.32})$$

Where the cartesian coordinates are obtained by transformation of spherical coordinates, which are computed in each event. The relative velocity is calculated by means of Carnot's Theorem:

$$V_{rel} = \sqrt{V_0^2 + V_1^2 - 2V_0V_1 \cos \vartheta_{rel}}. \quad (\text{A.33})$$

Mass and Energy Calculations

In a full momentum transfer binary reaction, the masses of the two reaction products can be obtained using the momentum conservation law and the mass conservation law:

$$M_{proj} \vec{V}_{proj} = M_0 \vec{V}_0 + M_1 \vec{V}_1 \quad M_{proj} + M_{tar} = M_0 + M_1 + \vartheta_{pre} \quad (\text{A.34})$$

where M_{proj} , M_{tar} and ϑ_{pre} are the mass of projectile, the mass of target and the multiplicity of preequilibrium neutrons respectively. Projecting [A.34](#) onto the beam axis results in:

$$M_{proj} V_{proj} = M_0 V_0 \cos \vartheta_0 + M_1 V_1 \cos \vartheta_1 \quad 0 = M_0 V_0 \sin \vartheta_0 + M_1 V_1 \sin \vartheta_1 \quad (\text{A.35})$$

-

Solving the system of eq. [A.35](#) and [A.34](#) knowing V_i and ϑ_i from the previous calculations, the masses of the fragments are:

$$M_0 = \frac{(M_{proj} + M_{tar} - \vartheta_{pre}) V_1 \sin \vartheta_1}{V_0 \sin \vartheta_0 + V_1 \sin \vartheta_1} \quad (\text{A.36})$$

$$M_1 = M_{proj} + M_{tar} - \vartheta_{pre} - M_0 \quad (\text{A.37})$$

The Total Kinetic Energy is defined as the sum of the kinetic energy of the fragments in the exit channel, evaluated in the CM frame:

$$TKE = 0.5183M_0V_0^2(CM) + 0.5183M_1V_1^2(CM) \quad (A.38)$$

where the factor 0.5183 is a modification to the classical kinetic energy formula, applied in order to match masses in atomic units and velocities in cm/ns into energies in MeV. The Total Kinetic Energy Loss (TKEL) is, on the other hand the difference between the available kinetic energy in CM frame and the TKE of the fragments: $TKEL = E_{CM} - TKE$, where E_{CM} (the bombarding energy in the CM frame) is the available energy. Since the excitation energy of the fragments is given by eq. 1.3, the TKEL can be considered as a rough measure of excitation energy in reactions with Q-value near zero.

Energy Loss Corrections

After the first mass-velocity extraction, a correction for energy loss in both target and start detectors has to be done. This correction, again, is based on the assumption that the interaction with thin start detectors and target layers do not affect sensibly the direction of the fragment. At each step i of the recursive algorithm, the masses $M_{0,1}^i$ are re-calculated using the kinematic formulas A.36 and A.37, $V_{0,1}^i$ are obtained by means of the correction:

$$V_{0,1}^{i+1} = V_{0,1}^0 + \delta V_{0,1}^i. \quad (A.39)$$

where $V_{0,1}^0$ are the velocities calculated from measured TOFs and flight paths and $\delta V_{0,1}^i$ are the i -th estimation of the velocity correction. The latter quantity is related to the energy loss, ΔE , of the fragment passing through matter which is difference between the fragment energy before and after passing through an absorber. The measured velocity provides the final energy while the initial

one is obtained by means range extrapolation: The range of an ion (A_{ion}, Z_{ion}) passing through an absorber (A_{tar}, Z_{tar}) is a function of its kinetic energy:

$$R(E) = \int_0^{E_i} \frac{1}{(-dE/dx)} dE \quad (\text{A.40})$$

which is known as set of points once a numerical integration of stopping power data is done. Given the final energy E_f and its related range $R(E_f) = R_f$, the range related to the initial energy would be $R_i = R(E_i) = R_f + T$ where T is the thickness of the absorber and the initial energy E_i is found by extrapolation. In appendix B a pseudo code shows the details of the algorithm developed during data analysis.

Since only the fragment mass is known, its atomic number is assumed to be the one of a stable nucleus having the measured mass A_{ion} :

$$Z_s = \frac{A_{ion}(1 + 0.0077A_{ion}^{-1/3})}{2 + 0.0154A_{ion}^{2/3}}. \quad (\text{A.41})$$

The formula A.41 provides Z of a nucleus of given A_{ion} , on the stability line through an interpolation of the latter [35]. Once E_f and i are found, ΔE is given by

$$\Delta E = E_i - E_f = 0.5183M(V_i^2 - V_f^2), \quad (\text{A.42})$$

being $V_i - V_f = \delta V$. Solving the 2nd-degree equation A.42 for δV and discarding the negative solution (with no physical meaning):

$$\delta V = \sqrt{V_f^2 - \frac{\Delta E}{0.5183M}} - V_f. \quad (\text{A.43})$$

Once the correction $\delta V_{0,1}^i$ is evaluated, the velocity (eq. A.39) is used in the formulas A.36 and A.37 to re-calculate a new approximation of the masses. This approximation $M_{0,1}^i$ is used as starting value for the successive step, in which

a new correction $\delta V_{0,1}^{i+1}$ is calculated and added again to $V_{0,1}^0$. The loop stops when $|M_1^{i+1} - M_1^i| < tol$. A chosen tolerance $tol=0.01$ is reached after a number of steps in the range 1-5. The correction is applied event-by-event taking into account the exit angle ϑ_i (with respect to the beam axis) of each fragment, which extends the thickness of each absorber by a factor $1/\cos \vartheta_i$.

In appendix B are shown ore details about the tool developed by the author.

A.3.6 Ternary Reaction Analysis

Data Filtering for Ternary Decay through *Pattern Spectra*

In the analysis of data containing both binary and (to be confirmed) ternary events, a first discrimination can be performed using *pattern* concept. When signals from several detectors are received by the Data Acquisition, a coincidence unit can perform logic operations such as AND or OR. By taking as example the experiment reported in Chapter 3, the CORSET arm where put in coincidence two by two (0-3 and 1-2): the AND between their timing signal can be considered as a TRIGGER for the acquisition. This AND signal can be, in turn, acquired through a TDC thus obtaining a "time" spectra which can be referred as a counting events, showing a peak of reasonably binary event and a background that can be discarded. The same goes for ternary events, by computing and acquiring the AND of three signals, in the experiment namely the signal from the the two inner arms and the OR of the fast signals coming from backward silicon telescopes: in this way is considered as ternary an event with TOF signals and at least one energy signal from backward. An example is given in Fig. A.5. The discrimination is performed by cutting the data outside the peak.

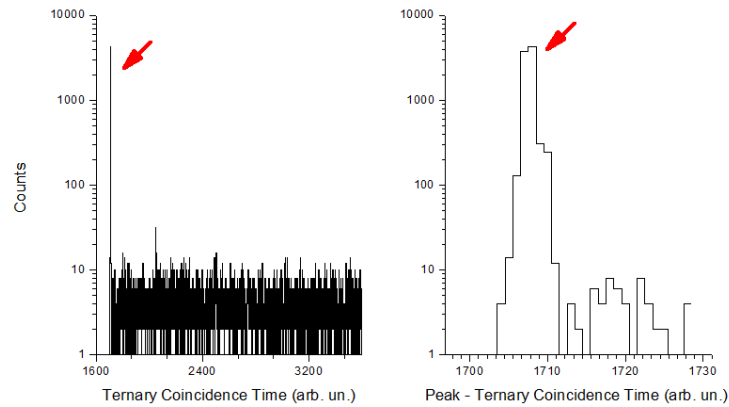


Figure A.5: Time spectra of triple coincidences. The background, related to random triple coincidences, can be discarded while the peak (highlighted in the right panel) contains all the "true" triple coincidences.

Vpar-Vper Test for Ternary Decay

After the gate applied on the ternary coincidence spectrum, it is possible to look at quantities which are strictly related to binary events, namely V_{\parallel} and V_{\perp} . Fig. shows a typical $V_{\parallel} - V_{\perp}$ matrix in which it is possible to recognize FMT binary events and ternary, but sequential, events (see par. 2.3 and A.3.5). Anomalies in the matrix can be interpreted as possible clues of non-binary, non-sequential decays. In par. 3.3.2 it is shown how different gates on this matrix are used to explore the anomalies, by looking at the corresponding areas in the coincidence matrix of the velocities of fragments detected by CORSET. For binary cases, it is possible to refer to the previous section about binary fission in the same reaction and section 2.3.

Test for Evaporated Particles

A further check consists in assuming that the most forward CORSET arms detected protons and alpha particles evaporated from the Compound Nucleus. Starting from this assumption, it is possible to compute the energy distribution of the particles/fragments and compare it to the Maxwellian distribution, typical for evaporation events.

Ternary Decay Mass Reconstruction

Once an event is assumed to be a true ternary decay, exploiting some measured quantities it is possible to reconstruct the masses of the three fragments by solving a system of three equations, derived from energy and momentum conservation laws.

The system would contain nine unknown quantities and only three equations, meaning that six quantities must be measured.

In the experiment of Chap. 3, $V_{1,2}$, $\vartheta_{1,2}$, E_3 and ϑ_3 are measured, leaving the three masses evaluable by solving the system.

In the specific case also a recursive correction on energy loss was performed on fragments 1 and 2, of the same typ as in par. A.3.5. Moreover, since the E detector in the E- Δ E assembly, covers a wide angular range (see par. 3.2), it was also included an algorithm which searches the ϑ_3 value in this range which minimize the difference $|M_{proj} + M_{tar} - M_1 - M_2 - M_3|$.

Details on the equations follow [34].

Energy conservation law is:

$$E_p = E_1 + E_2 + E_3 - Q,$$

$$\text{or, } M_1(V_1^2 + 2) + M_2(V_2^2 + 2) + 2(E_3 - E_p - M_p - M_t + M_3) = 0 \quad (\text{A.44})$$

The momentum conservation along the perpendicular to the beam direction is:

$$M_p V_p \sin 0^0 = M_1 V_1 \sin \theta_1 + M_2 V_2 \sin \theta_2 + M_3 V_3 \sin \theta_3,$$

$$\text{or, } M_1 = \frac{-M_2 V_2 \sin \theta_2 - \sqrt{2M_3 E_3} \sin \theta_3}{V_1 \sin \theta_1}. \quad (\text{A.45})$$

The momentum conservation along the beam direction is:

$$M_p V_p = M_1 V_1 \cos \theta_1 + M_2 V_2 \cos \theta_2 + M_3 \sqrt{\frac{2E_3}{M_3}} \cos \theta_3. \quad (\text{A.46})$$

Using equation A.45 in the equation A.46, the expression for mass M_2 is:

$$M_2 = \frac{M_p V_p \sin \theta_1 - \sqrt{2M_3 E_3} \sin(\theta_1 - \theta_3)}{V_2 \sin(\theta_1 - \theta_2)} \quad (\text{A.47})$$

Using equation A.47 into equation A.45, the result is

$$M_1 = \frac{-M_p V_p \sin \theta_1 \sin \theta_2 + \sqrt{2M_3 E_3} \sin \theta_2 \sin(\theta_1 - \theta_3) - \sqrt{2M_3 E_3} \sin \theta_3 \sin(\theta_1 - \theta_2)}{V_1 \sin \theta_1 \sin(\theta_1 - \theta_2)}. \quad (\text{A.48})$$

Now using equation A.47 and A.48 into equation A.44, the result is

$$M_3 \alpha + \sqrt{M_3} \beta + \gamma = 0, \quad (\text{A.49})$$

where,

$$\begin{aligned} \alpha &= 2V_1 V_2 \sin \theta_1 \sin(\theta_1 - \theta_2), \\ \beta &= \sqrt{2E_3} V_2 (V_1^2 + 2) \{ \sin \theta_2 \sin(\theta_1 - \theta_3) - \sin \theta_3 \sin(\theta_1 - \theta_2) \} \\ &\quad - \sqrt{2E_3} V_1 (V_2^2 + 2) \sin \theta_1 \sin(\theta_1 - \theta_3), \\ \gamma &= M_p V_p \sin \theta_1 \{ V_1 (V_2^2 + 2) \sin \theta_1 - V_2 (V_1^2 + 2) \sin \theta_2 \} \\ &\quad + 2V_1 V_2 \sin \theta_1 \sin(\theta_1 - \theta_2) (E_3 - E_p - M_p - M_t). \end{aligned}$$

The solution of equation A.49 is:

$$M_3 = \frac{\beta^2 - 2\alpha\gamma \pm \sqrt{\beta^4 - 4\alpha\beta^2\gamma}}{2\alpha^2}, \quad (\text{A.50})$$

- M_1 is calculated from equation A.48 by using equation A.50.

- M_2 is calculated from equation A.47 by using equation A.50.
- M_3 is calculated equation A.50.

Appendix B

Developed Tools and Relative Pseudo Code

The following are pseudo codes explaining in slightly more details the algorithms developed by the author.

B.1 Eloss Code

Getting the initial energy:

```
double dq_Eloss_get_initial_energy (  
    double Ef, // mesured final energy of fragment  
    double Aion, double Zion, //A and Z of fragment  
    double Atar, double Ztar, T) //A, Z, thickness of absorber  
{  
  
    Open_range_data (Atar, Ztar); // ascending order in energy and range  
  
    while (E<=Ef){  
        search range date since the closest value to Ef is found  
    }  
  
    Rf = linear interpolation to find the range value related to Ef  
    Ri = Rf + T;
```

```

while (R<=Ri){
  search range date since the closest value to Ri is found
}

Ei = linear interpolation to find the energy value related to Ri
return Ei;
}

```

Getting velocity correction:

```

double dq_velocity_correction (
  double measured_E, \\ Measured energy
  double theta, double V, \\exit angle in lab frame, velocity of
  fragment
  double Aion, double Atar0, double Ztar0 ...) \\parameters
  identifying the ion and several absorbers
{

Interpolate the stability line
Use Aion to estimate Zion using the interpolated stability line
//assuming that the ion having mass Aion would have the atomic
  number of the most stable species having this mass

```

The following block is repeated for each absorber, starting from the last and going backward. For each absorber, the final energy equals the initial energy of the previous step. In the first step, $E_f = measured_E$.

```

Ei = Ef
while (diff > 0){
  Q2 = charge state projection (Ei); //evaluation of charge
  state using Schwietz-Grande mean charge state formula
  (ref..)

  Ei = dq_Eloss_get_initial_energy (Ef, Aion, Zion, Atar, Ztar,
  T/cos (theta) );

```

```

diff = fabs(Q1-Q2);
Q1 = Q2;

e = Ei;
}

```

The routine tries to find the initial energy taking into account the charge state, which depends on initial energy. Starting from the zero step approximation of $E_i = E_f$, the charge state is evaluated and then E_i is evaluated. At this point everything is repeated starting from the new value of the initial energy, leading to another evaluation of charge state. The routine continues until two successive evaluations of charge-state are equal, usually it takes 1 to 3 iterations. After the last absorber (first from the point of view of the fragment) the correction on velocity can be evaluated.

```

DE = Ef - measured_E;

//Velocity correction
DV = sqrt( V*V + DE/(0.5183*Aion) ) - V;

return DV;
}

```

B.2 Viola Systematics and prediction of Laboratory correlation angles of Fission fragments

```

void labangles (
    double r, //mass ratio of the fragments
    double Ap, double At, //masses of proj. and target
    double Ebomb) //bombarding energy

```

```
{  
  
take in input the mass ratio r;  
evaluate the masses of the fragments;  
evaluate TKE;  
evaluate fragment velocities in CM frame;  
  
for (thetaCM_0 = 0.; thetaCM_0 <= 180.; thetaCM_0+=0.5){  
    thetaCM_1 = 180. - thetaCM_0;  
    evaluate both angle in lab frame using the CM motion;  
    print angles to file;  
}  
  
plot;
```

Appendix C

Main Experimental Setup

Parameters

C.1 Xe+Pb Setup

C.1.1 PRISMA Arm

PRISMA arm was placed at 45° with respect to the beam axis, with the entrance MCP tilted by 45° , thus being parallel to the beam.

Component	Distance(mm)
Target - MCP	250
MCP - Quadrupole	250
Quadrupole - Dipole	600
Dipole - MWPPAC	3285
PPAC - IC	720

Table C.1: Table of PRISMA arm component distances.

Component	Size(mm ²)	Sections
Entrance MCP	76×100	1
PPAC	1000×130	10×1
IC window	1000×130	10×1
IC area	1000×1060	10×4

Table C.2: Table of PRISMA arm component sizes.

C.1.2 TOF Arm

TOF arm was placed at 52° with respect to the beam axis and perpendicular to the radius at this angle.

Component	Distance(mm)
CORSET MCP - Target	67
Bragg PPAC - Target	884.5

Table C.3: Table of the TOF arm component distances.

Component	Size(mm ²)	Sections
Entrance MCP	2.2×2.2	1
circular PPAC	100 × 100	1

Table C.4: Table of TOF arm component sizes.

C.2 NRO127 Setup

C.2.1 CORSET

	deg	cm	cm	cm ²	cm ²
arm	θ	Start-target	Stop-Start	Start size	Stop size
0	-65	8	18	3×2.2	8.6×6.9
1	-40	8.5	22	2.2×2.2	8.6×6.9
2	40	8.5	22	2.2×2.2	8.6×6.9
3	65	8	18	3×2.2	8.6×6.9

Table C.5: Table of the CORSET parameters.

C.2.2 Silicon Detectors

ΔE detectors are collimated by means of 1 cm diameter diaphragm. E detectors size is 5×5 cm².

	deg	cm	cm	μm	μm	deg
Tel.	θ	E-targ.	ΔE -targ.	E thickn.	ΔE thickn.	Ang. range
0	109.5	27	n/a	300	n/a	10.5
1	127.5	27	n/a	300	n/a	10.5
2	145.5	27.5	n/a	300	n/a	10.3
3	-154.5	21.7	15.8	300	20	3.6
4	-136.5	22	16.1	300	20	3.6
5	-118.5	22	16.1	300	20	3.6

Table C.6: Table of the telescope parameters.

	deg	cm	μm
monitor	θ	mon-beam	thickness
0	8.6	9.7	50
1	8.6	9.8	50
2	8.7	9.9	50

Table C.7: Table of the monitor parameters.

Bibliography

- [1] E. Haseltine, Discover Magazine, February 01, 2002.
- [2] V. Zagrebaev, W. Greiner, Phys. Rev. Lett. 101 (2008) 122701.
- [3] V. Zagrebaev, W. Greiner, Phys. Rev. C 78 (2008) 034610.
- [4] V. Zagrebaev, W. Greiner, J. Phys. G: Nucl. Part. Phys. 31 (2005) 825–844.
- [5] V. Zagrebaev et al., Phys. Part. Nucl. 38 (2007) 469.
- [6] V.Zagrebaev and W.Greiner, PRC 83 044618 (2011).
- [7] L. Corradi et al 2002 Phys. Rev. C 66 024606.
- [8] L. Corradi et al 2007 Int. Symp. on Exotic Nuclei (Khanty-Mansiysk, 2006)
AIP Conf. Proc. 912 p 13.
- [9] P. Schall et al., Phys. Lett. B191, 339 (1987).
- [10] F. Gonnemann, Nucl. Phys. A 734, 213 (2004).
- [11] Yu.V. Pyatkov et al., Eur. Phys. J. A 45, 29 (2010).
- [12] W.J. Swiatecki, 2nd UN Intern. Conf. on the Peaceful uses of atomic energy
(Geneva, 1958), Vol. 15,p. 248.
- [13] H. Diehl and W. Greiner, Nucl. Phys. A229, 29 (1974).
- [14] G. Royer and J. Moignen, J. Phys. G: Nucl. Part. Phys. 18, 1781-1792 (1992).
- [15] M.G. Itkis, E. Vardaci, I.M. Itkis, G.N.Knyazheva, E.M.Kozulin, Nucl.
Phys. A944, 204 (2015).

- [16] V. Zagrebaev and W. Greiner, *Giant Nuclear Systems of Molecular Type*, Lecture Notes in Physics, 818, C. Beck (ed.), Springer-Verlag Berlin Heidelberg 2010.
- [17] A.V. Karpov and A. Adel, Ternary clusterization of heavy nuclear systems, 4th South Africa - JINR Symposium: Few to Many Body Systems: Models, Methods and Applications, Dubna, Moscow region, September 21-25 (2015).
- [18] K. Manimaran and M. Balasubramaniam, *EPJ A* 45, 293 (2010).
- [19] K. Manimaran and M. Balasubramaniam, *Phys. Rev. C* 83, 034609 (2011).
- [20] V. Zagrebaev, A.V. Karpov and W. Greiner, *Phys. Rev. C* 81, 044608 (2010).
- [21] I.V. Panov et al., *Nucl. Phys. A* 747, 633 (2005).
- [22] M.G. Itkis et al., *Nucl. Phys. A* 734 (2004) 136.
- [23] E.M. Kozulin, E. Vardaci et al., *Phys. Rev. C* 86, 044611 (2012).
- [24] R. Bass 1980 *Nuclear Reactions with Heavy Ions* (Berlin: Springer) p 326.
- [25] A.M. Stefanini et al., *Nuclear Physics A* 701 (2002) 217c–221c.
- [26] G. Montagnoli et al., *Nuclear Instruments and Methods in Physics Research A* 547 (2005) 455–463.
- [27] S. Beghini et al., *Nuclear Instruments and Methods in Physics Research A* 551 (2005) 364–374.
- [28] D. Quero et al., *IOP Conf. Series: Journal of Physics: Conf. Series* 1014, 012015 (2018).
- [29] E.M. Kozulin et al., *Phys. Rev. C* 89, 014614 (2014).

-
- [30] A. Pulcini et al., IOP Conf. Series: Journal of Physics: Conf. Series 1014, 012013 (2018).
- [31] V. E. Viola Jr et al. Phys. Rev. 130, (1963) 2044.
- [32] V. E. Viola et al., Phys. Rev. C 31 (1985) 1550-1552.
- [33] Courtesy of MD Ashadduzzaman.
- [34] MD Ashadduzzaman, PhD Thesis, University of Naples Federico II.
- [35] P. A. Posocco, *Characterization of ALPI performances for future upgrades*, PhD Thesis.